이학박사 학위논문

Study of Galactic H I Shells/Supershells using the I-GALFA Survey Data

아레시보망원경 탐사자료를 이용한 우리은하 중성수소가스 구각구조 연구

2017년 8월

서울대학교 대학원

물리·천문학부 천문학전공

박 금 숙

Study of Galactic H I Shells/Supershells using the I-GALFA Survey Data

by

Geumsook Park
(pgs@astro.snu.ac.kr)

A dissertation submitted in partial fulfillment of the requirements for the degree of

Doctor of Philosophy

in

Astronomy

in

Astronomy Program
Department of Physics and Astronomy
Seoul National University

Committee:

Professor	Woong-Tae Kim
Professor	Bon-Chul Koo
Professor	Myung Gyoon Lee
Doctor	Yong-Sun Park
Doctor	Ji-hyun Kang

Dedicated

To

My Father In Heaven,

My Mother,

And

My Beloved Husband

ABSTRACT

Neutral atomic hydrogen (H I) gas in interstellar space is largely organized into filaments, loops, and shells. H I shells are the interstellar material swept up by supersonic shock waves produced by mechanical energy sources such as stellar winds and supernovae (SNe). Among H I shells, gigantic structures called as "supershell" require energy larger than 3×10^{52} erg to form and are thought to be produced by either the explosion of multiple SNe in OB associations or, alternatively, by the impact of high-velocity clouds (HVCs) falling into the Galactic disk.

We carry out a systematic study of H I shells/supershells in the first Galactic quadrant ($\ell \approx 32$–77° and $|b| \approx 10^\circ$) using the "Inner-Galaxy Arecibo L-band Feed Array (I-GALFA)" H I 21-cm survey data. The high-resolution ($4'$) and high sensitivity (0.2 K) of the survey allow us to exploit the true nature of the sources detected in previous low-resolution studies and also to identify weak or distant shells/supershells that were not detectable before. Our work is composed of three parts: (1) examine fast-expanding H I shells associated with Galactic supernova remnants (SNRs). (2) confirm the objects in the low-resolution ($36'$) catalog of Heiles (1979) and search for new H I shells/supershells. (3) examine detailed spatial and velocity structures of the supershell GS040.2+00.6−70 and the compact HVC HVC040+01−282 (hereafter, GS040 and CHVC040, respectively).

In the first part, among the 39 known Galactic SNRs in the I-GALFA survey area, we find that four SNRs have an associated H I shell: W44, G54.4−0.3, W51C, and CTB 80. All four were previously identified in low-resolution surveys, and three of those (excluding G54.4−0.3) were previously studied with the Arecibo telescope. A remarkable new result, however, is the detection of H I emission at both very high positive and negative velocities in W44 from the receding and approaching parts of the H I expanding shell, respectively. This is the first detection of both sides

of an expanding shell associated with an SNR in the inner Galaxy in H I 21 cm emission. The high-resolution I-GALFA data also reveal a prominent expanding H I shell with high circular symmetry associated with G54.4−0.3. We explore the physical characteristics of four SNRs and discuss what differentiates them from other SNRs in the survey area. We conclude that these four SNRs are likely the remnants of core-collapse SNe interacting with a relatively dense ($\gtrsim 1\mathrm{cm}^{-3}$) ambient medium, and we discuss the visibility of SNRs in the H I line.

In the second part, we report the detection of 38 H I shells/supershells in the I-GALFA data: 13 are the previously-known Heiles' shells while 25 are new shell candidates. Their geometric mean diameter and velocity extent have about 1–13° and 7–65 km s^{-1}, respectively. The high-resolution I-GALFA images show that some of them, mostly in the inner Galaxy, are complicated with other chimney or more than one shell, and some might be located near active star-forming region(s). We estimate kinematic distances, radii, heights from the Galactic midplane (if available), and explosion energies of the found objects. Fifteen objects are likely to be supershells. We compare the Galactocentric distribution of H I shells/supershells with those of H II regions and giant molecular clouds. The comparison implies that many inner Galactic H I supershells are missing in our shell list. One possibility would be that many H I supershells there had broken through the disk and evolved to "chimneys" or "worms." We also present the result of investigations on the association of H I shells with molecular clouds.

In the third part, we report the discovery of a kiloparsec-size supershell GS040 in the Galactic outskirts with the CHVC040 at its geometrical center. Our Arecibo H I images reveal that GS040 appears as a complete circular ring with complicated structures inside while CHVC040 shows a bright elongated core surrounded by diffuse gas with a sharp boundary at the far side of the Galactic disk. The analysis of morphological and physical properties of the both objects suggests that CHVC040

collided with the disk ~ 4.3 Myr ago to form a supershell and could be a fragment of a nearby disrupted galaxy or a cloud that originated from an intergalactic accreting flow. Our results imply that some compact HVCs can survive their journey through the Galactic halo and supply energy and momentum into the Milky Way disk.

Keywords: Galaxy: disk – ISM: bubbles – ISM: supernova remnants – ISM: clouds – radio lines: ISM

Student Number: 2008-30826

Contents

List of Figures

List of Tables

Chapter 1

Introduction

1.1 H I Shells/Supershells

1.1.1 H I Shells/Supershells in the Interstellar Medium

Hydrogen is the most common element in the universe, most of which is in the neutral atomic state in the interstellar medium (ISM). Neutral atomic hydrogen (H I) emits at a specific radio wavelength of 21 cm (a frequency of 1.420 GHz), by a spin-flip transition between the hyperfine levels of the hydrogen ground state. The transition rate is very low (spontaneously only once every a few million years), but H I is abundant in the ISM so one can easily observe the 21 cm spectral line. Therefore, H I observational data can be a useful tool to understand physical conditions of the ISM.

In our home Galaxy, the Milky Way, H I gas is distributed mostly within the Galactic disk (about 90% in H I mass) (e.g., Dickey & Lockman 1990; Kalberla & Kerp 2009). The H I disk is an almost flat layer with a thickness (full width at half-maximum; FWHM) of 230 pc in the inner Galaxy (inside the Solar orbit with respect to the Galactic center; in opposite directions, outer Galaxy), while it drops

to < 100 pc inside Galactocentric radii ($R_{\rm Gal}$) of ~ 3.5 kpc and increases to ~ 3 kpc at the outer Galaxy. The H I disk is well established up to $R_{\rm Gal} \sim 35$ kpc, and beyond that, turbulent H I gas extends out to $R_{\rm Gal} \sim 60$ kpc (Kalberla & Dedes 2008). For reference, the optical disk extends up to $R_{\rm Gal} \sim 15$ kpc (Robin et al. 1992; Ruphy et al. 1996).

When taking a close look at the H I disk, H I gas is highly complicated, but make shapes like filaments or sheets which are organized into shells, chimneys (or worms), or spurs. These structures have been observed even in earlier H I surveys with moderate resolution (e.g., Heiles 1979, 1984; Koo et al. 1992). H I shells are a major object of this thesis. They are observed as coherent features like a ring or arc-like shape for at least several km s^{-1}, and some of them change in size over velocity. In other words, it is thought that a limb-brightened part of walls of an H I bubble is observable.

What are H I shells? It has been explained as follows. The interstellar material swept up by supersonic shock waves produced by mechanical energy sources is initially ionized, and over time, cools down and becomes neutral. So eventually, the cooled-down expanding shells with enough column densities are observable in H I emission line at 21 cm. These structures can be discriminated until their velocities are comparable to the random velocity of the peripheral medium, i.e., they are merging into the general ISM.

1.1.2 Origin of H I Shells/Supershells

A natural question that arises is what injects energetic shock into the ISM. The energy sources have been thought of as H II regions, stellar winds, supernova (SN) explosion, high-velocity clouds (HVCs), and so on. The dominant and most violent sources among them are supernovae (SNe), which release huge amounts of kinetic energy into the ISM in a short time every 20–70 yrs (See Section 2.2 of Koo &

Kang 2004). There are two main classes of SN explosions: Type Ia SNe and core-collapse SNe (CCSNe). Their progenitors are population II stars (e.g., Wang & Han 2012; Maoz & Mannucci 2012) and massive stars with masses more than 8 $M_{\odot}$ (e.g., Smartt 2009), respectively. Both erupt the stellar material with a total kinetic energy $\sim 10^{51}$ erg and an expansion speed $\leq 10^{4}$ km s^{-1}. However, there is a difference in forming shells. Type Ia SNe and a small fraction of CCSNe are likely to occur in isolation. These single SN explosions can produce isolated expanding shells of radius ≤ 100 pc. However, most SNe are CCSNe, and most CCSNe are correlated both in space and time because most of the massive stars form in clusters (e.g., Higdon & Lingenfelter 2005). Therefore, they can generate large H I shells with a radius more than a few hundred parsec (pc), i.e., 'supershells' (Heiles 1979). If the injected energy into the ISM is large enough that the sizes of supershells become comparable with the scale height of the galactic gaseous disk, supershells can even break through the disk to produce galactic "chimneys"[1] that could be pathways for hot gas and heavy elements to disperse to the galactic halo (Heiles 1984; Norman & Ikeuchi 1989).

Multiple SNe, stellar winds, or their combination are the acceptable energy sources for many shells and supershells, but it seems to be insufficient in some cases. For example, quite a few supershells with sizes > 1 kpc require much larger injection energy (kinetic energy $> 10^{53}$ erg) which can be difficult to imagine from stellar origin (e.g., Heiles 1979; McClure-Griffiths et al. 2002). Also, largest H I shells appear at large galactocentric radii in external galaxies as well as the Milky Way (e.g., Heiles 1979; Deul & den Hartog 1990; McClure-Griffiths et al. 2002; Boomsma et al. 2008). Several alternative scenarios have been suggested, for example, the impact of HVCs on the galactic gaseous disk (e.g., Tenorio-Tagle 1980; Tenorio-Tagle et al. 1987), gamma-ray bursts (e.g., Loeb & Perna 1998), and gravitational and

[1] These structures are fragmented shell walls and sometimes referred to as galactic "worms" (Koo et al. 1992).

thermal ISM instabilities in the galactic disk (e.g., Wada et al. 2000). The most popular one among these is the collision of HVCs with the disk, which is supported by the observational report by Mirabel & Morras (1990).

1.1.3 Importance of the H I Shells/Supershells Study in the Milky Way

Why H I shells/supershells should be explored? That is because, as one of the outgrowths of the most energetic physical processes in the ISM, these structures play crucial roles in the evolution of ISM and ultimately, the evolution of galaxies. As mentioned in previous section, they participate in the circulation of matter and energy not only between stars and the ISM but also between the galactic disk and the galactic halo. Also, when considering that many of them are the fossils of stellar winds and SNe, they can provide a continuous record of stellar feedback processes in the ISM even after parental stars eventually fade away.

The Milky Way is an excellent laboratory for studying the ISM evolution both in microscopic and macroscopic views although there are some difficulties since we are located inside the disk of our Galaxy, e.g., kinematic distance ambiguity. Observed Galactic H I shells/supershells have sizes varying from tens of pc to a few kiloparsec (kpc), at angular scales corresponding to tens of arcminutes to dozens of degrees within our Galaxy. So, detailed structures of H I shells/supershells can be hard to study in other galaxies. In addition to the resolution limit, there is a sensitivity limit to faint H I gas of low column densities. Therefore, the Milky Way allows us in-depth studies of individual objects as well as systematic studies of H I shells/supershells.

1.1.4 Previous Observational Studies of H I Shells/Supershells in the Milky Way

There have been many observational studies in finding H I shells not only toward known individual Galactic supernova remnants (SNRs) but also by using a blind survey from H I data of the Milky Way. The former is related to small shells having similar sizes to the SNRs, and the latter is including larger ones.

Koo & Heiles (1991) and Koo & Kang (2004) had searched systematically for H I shells from northern and southern Galactic SNRs known at that time, respectively. They used H I data at a moderate resolution of $36'$ and $16'$, respectively. These studies showed that about 10% of known Galactic SNRs are associated with high-velocity H I gas, and they are likely to be a portion of fast-expanding shells in a snowplow phase. Since the SNRs are usually less than 1°, high-resolution observation is essential to confirm the association. Such high-resolution studies have been done for some of the SNRs and confirmed the shell-like structure of the high-velocity H I features, e.g., CTB 80 (Koo et al. 1990), W44 (Koo & Heiles 1995), W51C (Koo & Moon 1997a), and IC 443 (Giovanelli & Haynes 1979; Braun & Strom 1986; Lee et al. 2008). Also, there had been papers reporting the detection of H I shells with expansion velocities smaller than $\sim$20 km s^{-1}, but it is usually difficult to derive the parameters of such low-velocity H I shells due to H I background confusion (e.g., Kothes et al. 2005; Cazzolato & Pineault 2005; see also references in Koo et al. 2004).

As a pioneering study, Heiles had done blind surveys to find H I shells/supershells using the all-sky H I images available at that time (Heiles 1976, 1979, 1984). After that, many observational studies have been done by visual inspection or using an automatic algorithm or using a combination of two methods. McClure-Griffiths et al. (2002) found 19 new H I shells in the Southern Galactic Plane Survey (SGPS; FWHM = $16'$). Ehlerová & Palouš (2005) developed an automatic method to find

an H I shell using Leiden-Dwingeloo H I survey data (LDS; FWHM = 30′; Hartmann & Burton 1997), and then Ehlerová & Palouš (2013) improved their method and covered the whole sky using Leiden/Argentine/Bonn (LAB; FWHM = 36′; Kalberla et al. 2005) survey data. They identified 333 shells in the whole Galaxy. Daigle et al. (2007) schemed out a new automatic method especially for expanding small H I shells with radii < 40 pc using the Canadian Galactic Plane Survey (CGPS; Taylor et al. 2003), and obtained detection of a few thousand shells in the Perseus arm. The recent catalog of Suad et al. (2014) is done by mixing a visual inspection and an automatic searching algorithm and lists 566 supershell candidates in the second and third Galactic quadrants from the LAB data. Also, using the Search for Extraterrestrial H I survey data (SETH I; FWHM = 6′) obtained the Arecibo telescope before the release of the Galactic Arecibo L-Band Feed Array H I (GALFA-H I; Peek et al. 2011), Sallmen et al. (2015) identified 74 new H I shells over a wide range of Galactic latitudes. In summary, these studies have found hundreds of H I shells/supershells in our Galaxy, ranging size from tens to thousands of pc. Some of them are expanding at speeds of a few km s^{-1} to about 30 km s^{-1}, and some are stationary. About half of H I shells/supershells are located within $|z| \lesssim 500$ pc (e.g., Ehlerová & Palouš 2005; Suad et al. 2014). Several objects have been studied in details (e.g., Aquila supershell (Maciejewski et al. 1996), Ophiuchus superbubble (Pidopryhora et al. 2007) in the first quadrant, and several objects in the second-third quadrants).

1.2 Instrument: Arecibo Telescope

The 305-m William E. Gordon radio telescope at Arecibo[2] is one of the most powerful single-dish radio telescope in the world. The Arecibo telescope was the largest one until July 2016 when the Five hundred meter Aperture Spherical Telescope was built

[2] `http://www.naic.edu/science/userguide_set.htm`

in China. The Arecibo Observatory is located in Arecibo, Puerto Rico (coordinates: 18.34° N latitude, 66.75° W longitude). The Arecibo telescope consists of a primary spherical reflector, nestled in a natural karst sinkhole, with a triangular "platform" which is at 137 m above the main reflector and holds movable structures of a circular track and bow-shaped track (azimuth arm) (see Figure 1.1). A feed system together with secondary and tertiary sub-reflectors is situated within a geodetic (Gregorian) dome hanging on the azimuth arm. The azimuth arm can rotate along the circular track, and the Gregorian dome can operate independently within $\sim 20°$ of vertical along the azimuth arm. So, the sky to be observable is constrained from $-1.33°$ to $+38.03°$ in Declination.

The Arecibo L-band Feed Array (ALFA)[3] is a seven-feed receiver system installed within the Gregorian dome in April 2004. Each beam size is $\sim 3.8' \times 3.3'$, and the ALFA band covers 1225–1525 MHz which contains H I 21 cm line. The ALFA's high mapping speed facilitates a large-scale survey with a detailed view of high sensitivity.

1.3 I-GALFA H I Survey

The "Inner-Galaxy Arecibo L-band Feed Array (I-GALFA)" survey[4] (Koo et al. 2010; Gibson et al. 2012) is mapping all the H I in the inner Galactic disk visible to the Arecibo 305 m telescope at $\ell = 32°$ to $77°$ in the Galactic plane within $b \approx \pm 10°$ (or more off the plane) using the 7-beam ALFA receiver. The survey, which obtained 1.2×10^6 independent spectra, began in 2008 April and are completed in 2009 September. The mapping is done by "basketweave" scanning where the feed is driven up and down in zenith angle while the telescope is kept at the meridian, and by dividing the area into five fields, A to D and Z (Figure 1.2). One advantage of this basketweave mapping is to have many overlapping points, which can be used to

[3] `http://www.naic.edu/alfa/`

[4] `http://www.naic.edu/~igalfa/`

Figure 1.1. Photos of the Arecibo telescope: the platform (a), the primary reflector (b-c), and ALFA (d). (a) The platform of a triangular frame is supported by cables from three towers, one of which is seen on the right side of this photo. Just below the platform is a circular track and curved track called as the azimuth arm. The Gregorian dome is just below the azimuth arm and on the right. (b) A surface of the main reflector viewed from above and shadow of the platform. (c) An enlarged view seen from below. The mesh surface appears nearly solid to radio waves. (d) ALFA is installed inside the Gregorian dome.

calibrate relative gains among different receiver and different days. The spectra are obtained at every second by a $\sim$8,000-channel spectrometer, and these time-ordered data are later corrected for systematic instrumental effects. The technique that has been developed for Galactic ALFA surveys[5] is the so-called "Least-Square Frequency Switching," which corrects the bandpass without obtaining the usual OFF spectra as in traditional H I observations. The details of the observation and data reduction processes can be found in Peek et al. (2011). The local standard of rest (LSR) velocity coverage is from ~ -700 to $+700$ km s^{-1}. The final angular resolution (FWHM) and sensitivity are $4'$ and 0.2 K, respectively. The high-resolution and great sensitivity of the survey offer an excellent opportunity to investigate detailed H I structures or faint H I features.

The history of H I line surveys to explore the diffuse ISM and the Galaxy goes back to 1970s (Weaver & Williams 1973; Heiles & Habing 1974). The early surveys used the Hat Creek 85 foot (26 m) telescope. Moreover, then, many surveys have been released over the past two decades (e.g., Kalberla & Kerp 2009). For example, several major surveys are listed in Table 1 of Peek et al. (2011). Among them, all-sky surveys that combine similar observations are as follows. The Leiden-Argentine-Bonn survey (LAB, $36'$; Kalberla et al. 2005) and the H I 4π survey (HI4PI, $16\farcm2$; HI4PI Collaboration et al. 2016) covers the whole sky using single-dish telescopes, while H I data of the International Galactic Plane Survey (IGPS, $\sim 1'$)[6] covers part of the Galactic plane using interferometers. The all-sky surveys provide the whole view of the Galaxy but in relatively low spatial resolution. On the other hand, the

[5] The Galactic ALFA (GALFA) consortium consists of three sub-consortia grouped by radiative processes, namely H I line emission and absorption (GALFA-H I), radio continuum emission (GALFA-CON), and radio recombination line emission (GALFA-RRL). The I-GALFA is one of the GALFA-H I projects. For details, see the web page of `http://www.naic.edu/alfa/galfa/#surveys`.

[6] The IGPS includes the CGPS, SGPS, and VLA Galactic Plane Survey (VGPS, $1'$; Stil et al. 2006). See `http://www.ras.ucalgary.ca/IGPS/` for more details.

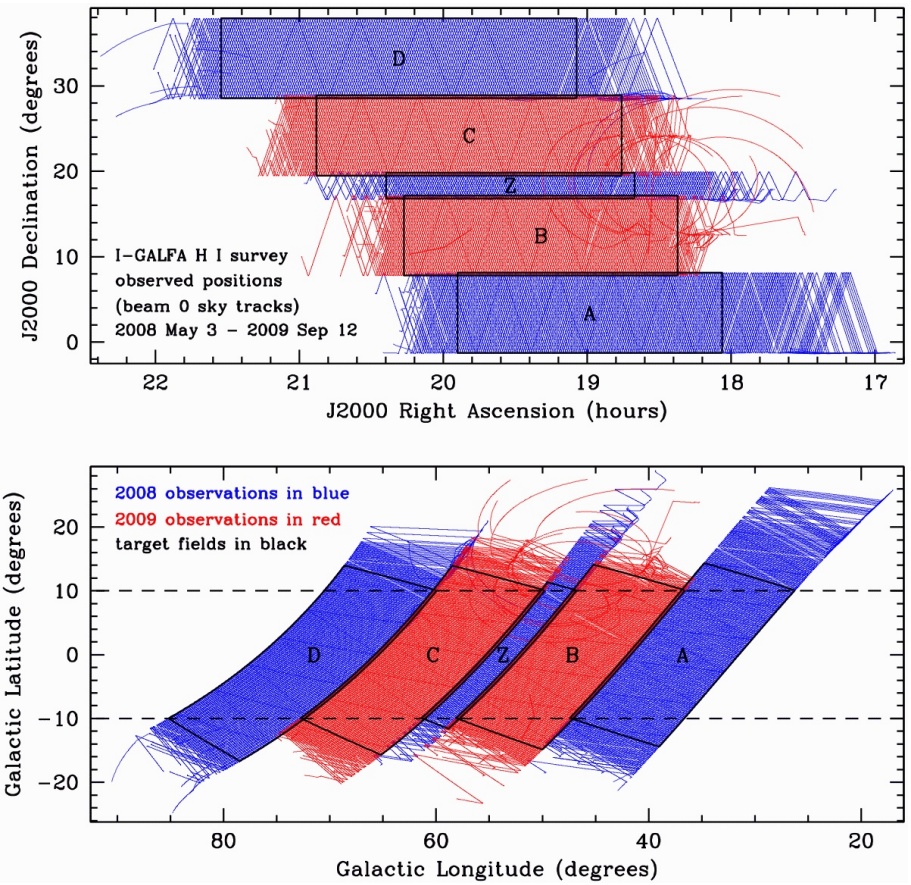

Figure 1.2. Observed positions of the I-GALFA H I survey marked with sky tracks of the central one of 7-beams. This image is taken from the I-GALFA web page.

interferometric surveys give the detailed view of the Galactic plane but limited in sky coverage and sensitivity. Therefore, the I-GALFA survey (or the full version GALFA survey) is intended to fill the gap between these two survey groups. In other words, the I-GALFA survey provides data on H I gas having three advantages which are considerable latitude coverage covering the Galactic plane, comparable beam size with interferometric observations, and excellent sensitivity thanks to the large single-dish.

1.4 Thesis Goals and Outline

To our knowledge, previous survey data are somewhat limited to study on H I shells/supershells either in details or a wide scope because of low-resolution or small b-coverage. However, the I-GALFA survey data overcome the two limits. That is, the high-resolution ($4'$) and high sensitivity (0.2 K) of the survey provide us an opportunity to exploit the true nature of the sources detected in previous low-resolution studies and also to detect faint shells that were not detectable before. Also, since the survey adequately covers the Galactic plane ($b \sim \pm 10^{\circ}$), large shells of several degrees in size there can be investigated. Therefore, this thesis goal is to identify H I shells/supershells in the I-GALFA survey data and to understand their physical nature and origin. As being complementary on previous studies, it could be worth checking the existence of these structures from a different perspective. Furthermore, this work is expected to contribute to a better understanding of physical structures and properties of the ISM.

In this thesis, we carry out a systematic study of H I shells/supershells in the first Galactic quadrant using the I-GALFA H I survey data. The remainder of this thesis is structured as follows. Chapter 2 presents results of searching H I shells associated with known SNRs using Green's catalog (Green 2009a,b) available at that time. Chapter 3 describes results of searching larger H I shells in the I-GALFA data. This work is composed of two parts: One is to confirm the objects in the low-resolution ($36'$) catalog of Heiles (1979) and the other is to search for new shell structures. Chapter 4 reports that one of the most interesting supershells, GS040.2+00.6−70 is generated by the impact of the high-velocity cloud, HVC040+01−282 on the Galactic disk. Chapter 5 summarizes this thesis.

Chapter 2

Fast-Expanding H I Shells Associated with Known Supernova Remnants[1]

2.1 Abstract

We search for fast-expanding H I shells associated with Galactic SNRs in the longitude range $\ell \approx 32°$ to $77°$ using 21-cm line data from the I-GALFA H I survey. Among the 39 known Galactic SNRs in this region, we find such H I shells in four SNRs: W44, G54.4−0.3, W51C, and CTB 80. All four were previously identified in low-resolution surveys, and three of those (excluding G54.4−0.3) were previously studied with the Arecibo telescope. A remarkable new result, however, is the detec-

[1] Most of the contents in this chapter were written as a separate paper: Geumsook Park, Bon-Chul Koo, Steven J. Gibson, Ji-hyun Kang, Daria C. Lane, Kevin A. Douglas, J. E. G. Peek, Eric J. Korpela, Carl E. Heiles, & Jonathan H. Newton, "H I Shells and Supershells in the I-GALFA H I 21-cm Line Survey: I. Fast-Expanding H I Shells Associated with Supernova Remnants," 2013, ApJ, 777, 14

tion of H I emission at both very high positive and negative velocities in W44 from the receding and approaching parts of the H I expanding shell, respectively. *This is the first detection of both sides of an expanding shell associated with an SNR in the inner Galaxy in* H I *21-cm emission.* The high-resolution I-GALFA survey data also reveal a prominent expanding H I shell with high circular symmetry associated with G54.4−0.3. We explore the physical characteristics of four SNRs and discuss what differentiates them from other SNRs in the survey area. We conclude that these four SNRs are likely the remnants of core-collapse supernovae interacting with a relatively dense ($\gtrsim 1$ cm^{-3}) ambient medium, and we discuss the visibility of SNRs in the H I 21-cm line.

2.2 Introduction

The ISM is pervaded by small and large expanding neutral atomic shells (e.g., Heiles 1979, 1984; McClure-Griffiths et al. 2002; Ehlerová & Palouš 2005; McClure-Griffiths 2012). These H I shells are the interstellar material swept up by supersonic shock waves produced by mechanical energy sources, including H II regions, stellar winds, SN explosions, and infalling high-velocity clouds. The dominant and most violent sources are SNe, which dump huge amounts of kinetic energy into the Galactic ISM every 20–70 yrs. But it is not clear how this kinetic energy is conveyed to the diffuse ISM, because this depends on the types and the physical environments of supernovae. Most SNe are CCSNe that have massive ($\geq 8\,M_{\odot}$) progenitors, and most CCSNe are produced in clusters (e.g., Higdon & Lingenfelter 2005). Most SN explosions, therefore, are correlated in both space and time, with such groupings frequently producing supershells and superbubbles with radii of more than a few hundred parsecs. Only Type Ia SNe and a small fraction of CCSNe are likely to occur in isolation. Single CCSNe probably explode inside a wind bubble created by their progenitor stars during the main-sequence phase. For stars of spectral type

later than B0, this bubble size is small ($\lesssim 1$ pc), and the SNRs can interact with dense molecular clouds in their early evolution (Chevalier 1999). Type Ia's, on the other hand, probably explode in either warm diffuse environments of density $n \sim 0.1$ cm^{-3} or in hot, rarefied gas with $n \sim 10^{-3}$ cm^{-3}. The amount and characteristics of the kinetic energy imparted to the ISM by SNe, therefore, should be diverse, and their role in shaping the kinematics of the atomic phase of the ISM is not clear. Consequently, H I observations of shells and supershells are useful not only to understand the nature and origin of individual structures but also, with reasonably large statistical samples, to explore the overall effects of SNe on the ISM.

There have been a number of systematic searches for H I shells associated with individual Galactic SNRs. Koo & Heiles (1991, hereafter KH91) carried out a survey of Galactic SNRs in H I 21-cm line using the Hat-Creek 25 m telescope (FWHM= $36'$). They observed 103 northern Galactic SNRs and detected high-velocity (HV) gas toward 15 SNRs including three SNRs known prior to the survey. Koo et al. (2004) searched for similar H I features toward 97 southern SNRs using the Parkes data from the SGPS (FWHM= $16'$; McClure-Griffiths 2001) and identified another 10 SNRs. Since the SNRs are usually less than 1° in diameter, high-resolution observations are essential to confirm the association of HV H I features with the radio continuum SNR. Such confirmations have been made in several cases, e.g., CTB 80 (Koo et al. 1990), W44 (Koo & Heiles 1995), W51C (Koo & Moon 1997a), and IC 443 (Giovanelli & Haynes 1979; Braun & Strom 1986; Lee et al. 2008). There have also been studies of almost stationary H I shells or H I bubbles associated with SNRs, but it is generally difficult to derive the parameters of such low-velocity H I shells due to H I background confusion (e.g., Kothes et al. 2005; Cazzolato & Pineault 2005; see also references in Koo et al. 2004).

Recently, the 7-beam ALFA receiver on the Arecibo 305m telescope has enabled Galactic H I surveys of unprecedented breadth and sensitivity with a fully-sampled

4′ beam (Peek et al. 2010, 2011). The I-GALFA survey (Koo et al. 2010; Gibson et al. 2012) covers the portion of the first Galactic quadrant visible to Arecibo, an area of more than 1650 square degrees at longitudes of 32° to 77° in the Galactic plane and extending to 10° or more off the plane. I-GALFA uses 0.184 km s^{-1} velocity channels over an LSR velocity range of ~ -700 to $+700$ km s^{-1}. Its brightness temperature root-mean-square (RMS) noise is 0.2 K in single empty channels. This combination of high sensitivity, high spatial and spectral resolution, and large area and velocity coverage are well suited for a systematic study of H I shells and supershells in the diffuse interstellar medium. In this first work, we search for fast-expanding H I shells associated with *known* SNRs and consider the implications of our results on their nature. A forthcoming work will discuss known H I shells and supershells as well as newly identified shells in the I-GALFA survey data. It is worth noting that the VGPS and CGPS cover most of the SNRs in the first quadrant in H I at higher spatial resolution ($\sim 1'$–$2'$). Their velocity coverage and sensitivity ($\pm$ 100–150 km s^{-1} and 1–3 K per 0.8 km s^{-1} channel) are not ideal to study faint, fast-expanding H I shells, but they can be useful to study shell fine structure at relatively low velocities.

In Section 2.3, we explain how we identify fast-expanding H I shells associated with SNRs and present the resulting list. In Section 2.4, we summarize the results on four SNRs that have associated fast-expanding H I shells. The two SNRs with new results, W44 and G54.4−0.3, are discussed in some detail. In Section 2.5, we explore the physical characteristics of the four SNRs and compare their properties to the other 35 SNRs in the survey area. Section 2.6 summarizes this work.

2.3 Identification of SNR H I shells

There are 275 Galactic SNRs in Green's catalog (Green 2009a,b).[2] Among them, 39 SNRs are included in the I-GALFA area (Table 2.1). The SNR name, size, and type parameters in Table 2.1 are from Green (2009a). (See the table note for more parameter details.) Note that the 21-cm spectra of sources with high continuum brightness are noisy, so faint high-velocity emission could not be seen in those objects. In Table 2.1, the ranks determined by KH91 are also listed. KH91 observed each SNR with the Hat Creek 85-foot telescope (FWHM=36′) at 9 points in a cross pattern centered on its catalog position and searched for SNRs with broad ($\simeq$ 10 km s^{-1}) excess emission over the background. They divided SNRs into four ranks: 0, 1, 2, and 3, where rank 3 has the highest probability for an associated fast-expanding H I shell. In rank 1, the central excess emission is brighter than the four outermost positions; in rank 2, the central excess emission is brighter than all outer positions; in rank 3, there is also excess emission at the highest positive or negative velocities; and in rank 0, none of these criteria are met. Among 39 sources in Table 2.1, 26 were studied by KH91, who classified 9 of these as rank 3 SNRs. KH91 mapped the excess HV emission in these 9 SNRs and concluded that the H I emission is not physically associated in 4 cases (marked as '(3)' in Table 2.1). Four SNRs are in rank 2. The other 13 (ranks 1 and 0) did not show any significant excess H I emission.

In order to identify fast-expanding shells associated with SNRs, we examined whether enhanced emission is present at the SNR position at high positive/negative velocities in several ways. We first inspected average, background-subtracted H I spectra toward individual SNRs as KH91 did. The average spectrum was obtained from a circular area with 1.1 times the SNR radius, while the background spectrum

[2] It was the latest version catalog available at that time. However, the list was updated after that, and the more recent version of Green's catalog contains 294 Galactic SNRs. See Green (2014) for updated information.

Table 2.1

Supernova Remnants in the I-GALFA Survey Area and Their Associated HV H I Gases

G-Name	Other Name	Size (arcmin)	Type	$T_{\rm b,21cm}$ (K)	KH91 Rank[a]	Note on the HV H I Gas from This Work
G31.9+0.0	3C391	7×5	S	140	1	···
G32.1−0.9	···	40?	C?	···	···	···
G32.4+0.1	···	6	S	1.7?	···	···
G32.8−0.1	Kes 78	17	S?	8.6?	2	···
G33.2−0.6	···	18	S	2.2	0	···
G33.6+0.1	Kes 79	10	S	45	2	···
G34.7−0.4	W44	35×27	C	52	3	associated HV H I gas at +124 – +240 and −120 – −67 km s^{-1}
G35.6−0.4	···	15×11	S	9.7	···	···
G36.6−0.7	···	25?	S?	···	0	···
G36.6+2.6	···	17×13?	S	0.6?	···	···
G39.2−0.3	3C396	8x6	C	74	2	···
G39.7−2.0	W50	120×60	?	2.2?	3	HV H I gas at +99 – +124 km s^{-1}, but extends beyond the SNR
G40.5−0.5	···	22	S	4.6	(3)	HV H I gas at −124 – −70 km s^{-1}, but portion of a larger structure
G41.1−0.3	3C397	4.5×2.5	S	401	(3)	HV H I gas at +110 – +120 km s^{-1}, but probably background emission
G42.8+0.6	···	24	S	1.1?	(3)	HV H I gas at +100 – +108 km s^{-1}, but probably background emission
G43.3−0.2	W49B	4×3	S	649	1	···
G43.9+1.6	···	60?	S?	0.5?	···	···
G45.7−0.4	···	22	S	1.8?	0	···
G46.8−0.3	(HC30)	17×13	S	13	1	···
G49.2−0.7	W51C	30	S?	39?	3	associated HV H I gas at +91 – +160 km s^{-1}
G53.6−2.2	3C400.2	33x28	S	1.6	0	···
G54.1+0.3[b]	···	12.4	C	1.9 − 3.8	1	···
G54.4−0.3	(HC40)	40	S	3.6	3	associated HV H I gas at +80 – +130 km s^{-1}
G55.0+0.3	···	20×15?	S	0.3?	···	···
G55.7+3.4	···	23	S	0.5	0	···
G57.2+0.8	(4C21.53)	12?	S?	2.5?	0	···
G59.5+0.1	···	15	S	2.7?	···	···
G59.8+1.2	···	20×16?	?	1.0	···	···

Continued on Next Page...

Table 2.1 – Continued

G-Name	Other Name	Size (arcmin)	Type	$T_{\rm b,21cm}$ (K)	KH91 Rank[a]	Note on the HV H I Gas from This Work
G63.7+1.1	···	8	F	6.1	···	···
G65.1+0.6	···	90×50	S	0.2	···	···
G65.3+5.7	···	310×240	S?	0.1?	(3)	HV H I gas at −122 – −159 km s^{-1}, but no morphological relation
G65.7+1.2	DA 495	22	F	2.1	2	···
G67.7+1.8	···	15×12	S	1.1	···	···
G68.6−1.2	···	23	?	0.3?	···	···
G69.0+2.7	CTB 80	80?	?	3.8?	3	associated HV H I gas at +43 – +110 km s^{-1}
G69.7+1.0	···	16×14	S	1.7	···	···
G73.9+0.9	···	27	S?	2.7	0	···
G74.0−8.5	Cygnus Loop	230×160	S	1.2	0	···
G74.9+1.2	CTB 87	8×6	F	38	0	···

Note. (1) The size is the angular diameter in radio continuum; a single value is quoted for nearly circular remnants, and the product of two values, the major and minor axes, is quoted for elongated remnants.

(2) The type codes 'S', 'F', or 'C' represent SNRs with a 'shell', 'filled-centre', or 'composite' radio structure. Uncertain parameters are listed with a question mark.

(3) The mean brightness temperature at 21 cm $T_{\rm b,21cm}$ is calculated from the 1 GHz flux ($F_{\rm 1GHz}$) and spectral index α ($F_\nu \propto \nu^\alpha$) in Green's catalog, i.e., $T_b = 1.42^\alpha F_{\rm 1GHz}\lambda^2/(2k\Delta\Omega_S)$ where λ is 21.1 cm and $\Delta\Omega_S$ is the solid angle of the source in steradians. For sources without spectral indexes, we adopt -0.5. We use the area of a circle (or ellipse) corresponding to the sizes in Table 2.1 as the solid angle.

[a]Rank '(3)' SNRs were classified as '3' but regarded to be not-associated with the SNRs by KH91.

[b]This SNR is classified as type 'C' since a larger radio shell at 1.4 GHz is detected by Lang et al. (2010). Its size and surface brightness, which is 100-200 mJy beam^{-1} with a beam of $6\farcm82 \times 6\farcm60$, are used to calculate T_b.

was obtained from an annular ring of $3'$ thickness surrounding the SNR. The radial interval between the SNR circle and the background ring was either $9'$ or 0.5 times the SNR radius, whichever was smaller. If another bright radio continuum source was located near the SNR, we left an appropriate space between the SNR circle and the background ring. We confirmed that all SNRs classified as rank 3 by KH91 show excess emission at high positive/negative velocities in their background-subtracted spectra, but we could not find additional SNRs with such features.

The above approach could have missed associated H I emission limited to small areas. We therefore inspected individual channel maps as well as (ℓ, v) and (b, v) maps to search for HV H I emission features spatially correlated with the SNRs in radio continuum maps. These are mostly from the VGPS or CGPS 21-cm continuum data with $\sim 1'$ resolution. For SNRs outside these two survey areas, we used either the lower-resolution ($\sim 4\farcm3$) Effelsberg 11-cm continuum data (Reich et al. 1990) or referred to previous works. Surprisingly, this detailed inspection yielded no additional detection. Instead, we confirmed the conclusion of KH91 that the HV emission in four rank 3 SNRs extended beyond the spatial extent of SNRs, so that it was probably not associated with the SNRs (marked as '(3)' in Table 2.1). In one of them (G40.5−0.5), we found that the HV H I emission is part of a much larger and prominent expanding shell. This result will be discussed in a forthcoming paper.

We are therefore left with the five rank 3 SNRs of KH91, but we suspect the HV H I emission in W50 (G39.7−2.0) is probably not associated with the SNR. W50 is a large, elongated shell-like SNR with SS 433 at the center, and KH91 reported the presence of very weak, extended H I emission at high positive velocities along the northern edge of the SNR where the continuum emission is enhanced (cf. Lockman et al. 2007). The high-resolution I-GALFA data confirm the presence of weak, filamentary H I emission along the SNR edge that appears connected to other H I structures well outside the SNR. We therefore regard the spatial correlation

between the H I emission and the SNR as a coincidence. Our results are summarized in the last column of Table 2.1, where we comment only on the HV emission features. We do see some low-velocity H I features that may be associated with SNRs, but many of these are confusing, and the scope of the present paper is limited to *fast-expanding* H I shells in SNRs.

2.4 Supernova Remnants with Fast-Expanding H I Shells

We have identified four SNRs that have associated HV H I gas: G34.7−0.4 (W44), G49.2−0.7 (W51C), G54.4−0.3 (HC40), and G69.0+2.7 (CTB 80). All four were ranked 3 by KH91, and follow-up high resolution observations have been made for SNRs W44, W51C, and CTB 80 (Koo & Heiles 1995; Koo & Moon 1997a; Koo et al. 1993). Figure 2.1 shows their average H I line profiles while Figure 2.2 shows (ℓ, v) maps across the centers of these four SNRs. (See Figure 2.3 for the areas used to derive these profiles.) The average profiles show some fluctuations in baseline, but they are removed in background-subtracted profiles. Figures 2.1 and 2.2 show that these four SNRs have excess H I emission at highest positive velocities. In W44, a faint, but clear, excess emission at highest negative velocities is also visible. Integrated (ℓ, b) maps in Figure 2.3 show the spatial distribution of HV H I emissions. The overlaid radio contours of SNRs clearly show that the HV H I gas is confined inside the SNR boundaries of W44 and G54.4−0.3. We discuss W44 and G54.4−0.3 in some detail below, where new results are obtained. We also briefly comment on the other two SNRs, W51C and CTB 80, where the I-GALFA results agree with previous findings.

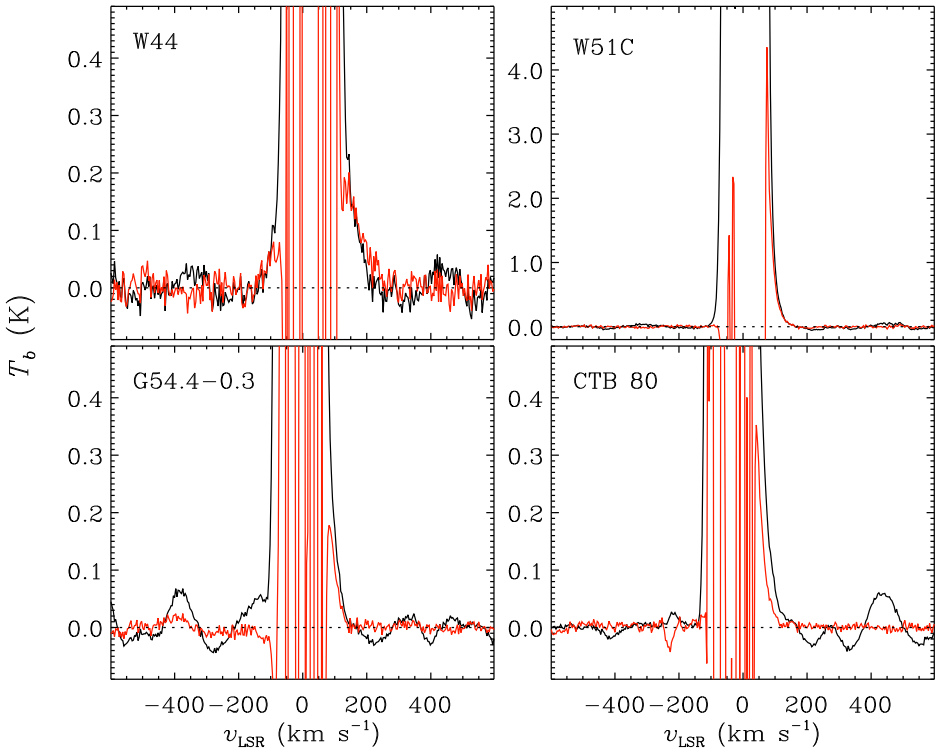

Figure 2.1. Average H I 21-cm line profiles of SNRs that have associated HV H I emission. Average profiles toward the SNRs are in black, while background-subtracted profiles are in red. (See Section 2.3 for details of the background subtraction.) Variations in H I 21-cm brightness between the source and background directions cause the wild fluctuations in the background-subtracted profiles at low velocities ($|v_{\rm LSR}| \lesssim 100$ km s^{-1}), but these have no effect on our analysis.

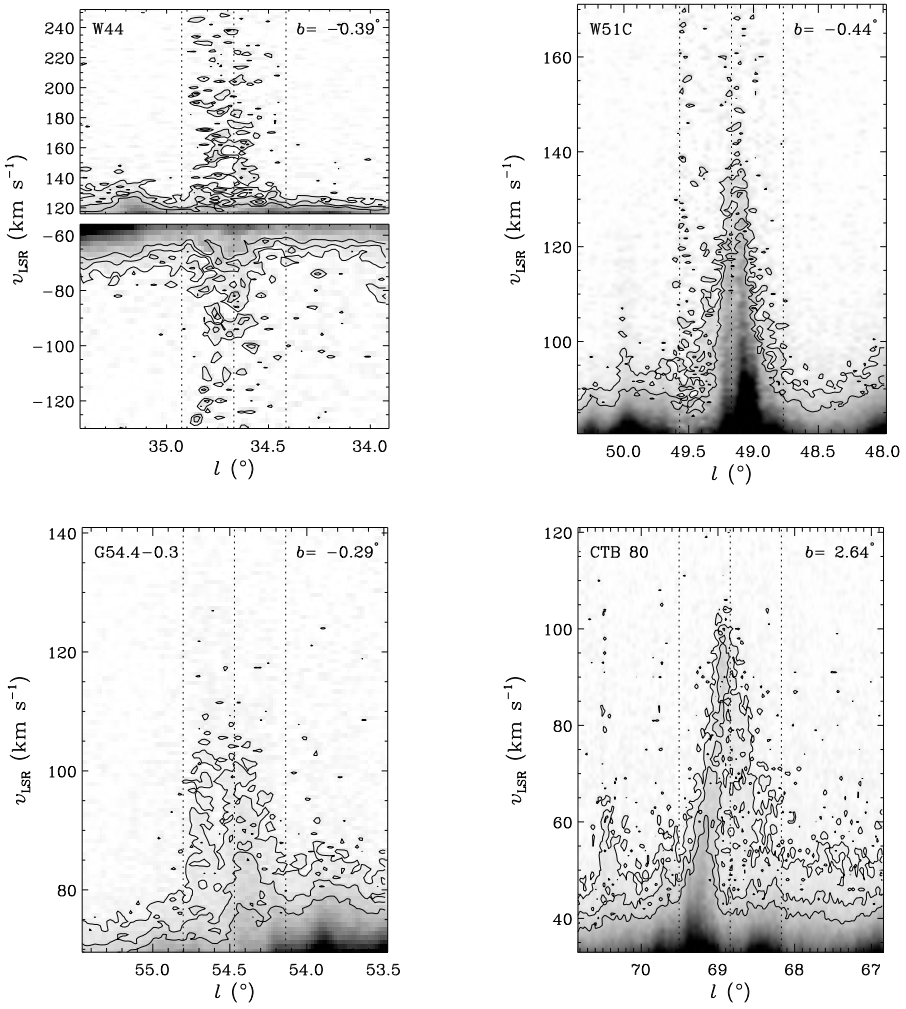

Figure 2.2. I-GALFA (ℓ, v) maps of H I emission of four SNRs. Each longitude-velocity map is at the latitude given in its upper-right corner. The central longitude of the SNR is marked by the middle dotted line in each panel. The other two dotted lines indicate the boundary of the SNR. The gray scale varies from 0 to 5 K (white to black). Contours are 0.5 and 1.0 K for W51C and 0.3, 0.6, and 1.0 K for the other SNRs.

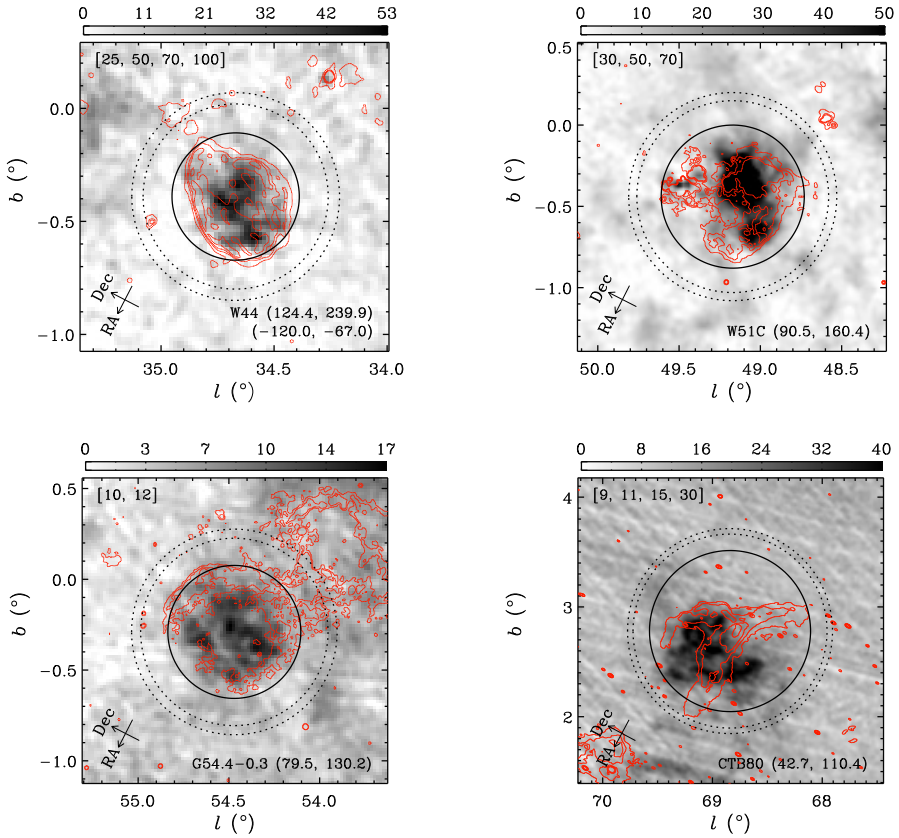

Figure 2.3. H I maps of the fast-expanding H I shells in four SNRs. The lower right corner of each panel gives the SNR name and velocity range for integration in km s^{-1}. For W44, both positive- and negative-velocity H I emissions have been used, although the former dominates. The scale bar units are K km s^{-1}. Red contours show the SNR morphology in 21 cm radio continuum, from the CGPS for CTB 80 and the VGPS for the others. Contour levels are written at the upper left corner of each panel in Kelvins. The black solid circle in each plot shows the mean size of the SNR in radio continuum. Two dotted circles mark the annulus used for estimating the background emission in deriving the average profiles in Figure 2.1. The size of W51C is 48′, and other sizes are from Green's catalog. To aid comparison to literature studies in Equatorial coordinates, arrows are shown in each frame indicating right ascension and declination (J2000) coordinate directions.

2.4.1 W44 (G34.7−0.4)

Previous studies

W44 is a middle-aged SNR ($\sim 2 \times 10^4$ yr) of mixed morphology, being shell-type in radio continuum but centre-filled in X-rays (Rho & Petre 1998). The radio continuum shell is somewhat elongated ($35' \times 27'$), and the southeastern[3] portion of the SNR shows enhanced radio emission (Figure 2.3; see also Castelletti et al. 2007). The pulsar PSR 1853+01 with a spin-down age of $\sim 2 \times 10^4$ yr lies $9'$ southwest of the center of W44, embedded in an X-ray emitting pulsar wind nebula (Petre et al. 2002; Wolszczan et al. 1991). H I gas at very high positive velocities ($\gtrsim +130$ km s^{-1}) accelerated by the SNR shock has been detected inside the remnant and studied using the Arecibo telescope (Koo & Heiles 1995). Ample evidence indicates the SNR is interacting with a molecular cloud in the southeast at $v_{\rm LSR} = +46.6$ km s^{-1} (Seta et al. 1998; Reach et al. 2005, and references therein). An extensive, organized system of thin and knotty H_2 filaments filling the SNR may indicate that the SN exploded inside a molecular cloud (Reach et al. 2005; Froebrich et al. 2011). Gamma-ray emission from the SNR has been detected by *Fermi*/LAT and *AGILE*/GRID at 50 MeV—10 GeV (Abdo et al. 2010; Giuliani et al. 2011). The emission is confined to an incomplete ring structure that matches well with the SNR but with a slight offset. The gamma-ray spectrum is well modeled with emission from cosmic-ray protons interacting with the nuclei in the ambient medium. Distance estimates to the SNR range from 2.6 to 3.2 kpc.

New Results

The I-GALFA images reveal several new H I features not seen in previous studies. First, we detect fast-moving H I gas associated with the SNR at both the highest

[3]Directions in this paper are all in reference to Galactic coordinates, not J2000 Equatorial coordinates.

positive and highest negative velocities. The negative-velocity emission is relatively faint, but clearly real (see below). The H I gas at positive and negative velocities must be from the receding and approaching hemispheres of the SNR, respectively. *This is the first detection of both sides of an expanding SNR shell in the inner Galaxy in the* H I *21-cm emission line.* We will discuss the visibility of fast-expanding H I shells in Section 2.5.2.

Figure 2.4 shows channel maps at both negative and positive velocities where we see H I emission confined inside the SNR boundary. At the highest negative velocities (-120 to -100 km s^{-1}), a knotty, elongated emission feature is seen along the southeastern boundary of the SNR (blue arrow in first two panels). It is worth noting that this is where the SNR is currently interacting with the molecular cloud (see references in the previous paragraph). At velocities less negative than this, the emission in the central area has a ring-like shape. At positive velocities, the H I emission is more prominent. At the highest positive velocities, the H I gas is confined to the central area of the remnant with the ring-like morphology noted by Koo & Heiles (1995). And at $v_{\rm LSR} = +130$ km s^{-1}, the H I gas forms a ring structure along the inner boundary of the SNR. This indicates that the H I gas is part of an expanding shell, and that the size of the H I shell is comparable to the radio continuum shell. This is in contrast to Koo & Heiles (1995), who concluded that the H I shell was smaller than the continuum shell from the extrapolation of the H I gas distribution at the highest velocities. Figure 2.4 indeed shows that the H I ring structure rather abruptly shifts from the central region to the SNR boundary as the velocity changes from +137 to +130 km s^{-1}. We speculate that the total extent of the expanding H I shell is probably comparable to the radio continuum shell, but the shell is not complete.

Figure 2.5 shows the average H I profile of W44. If the H I shell is symmetric, we can in principle derive an accurate systemic velocity by measuring the velocity at

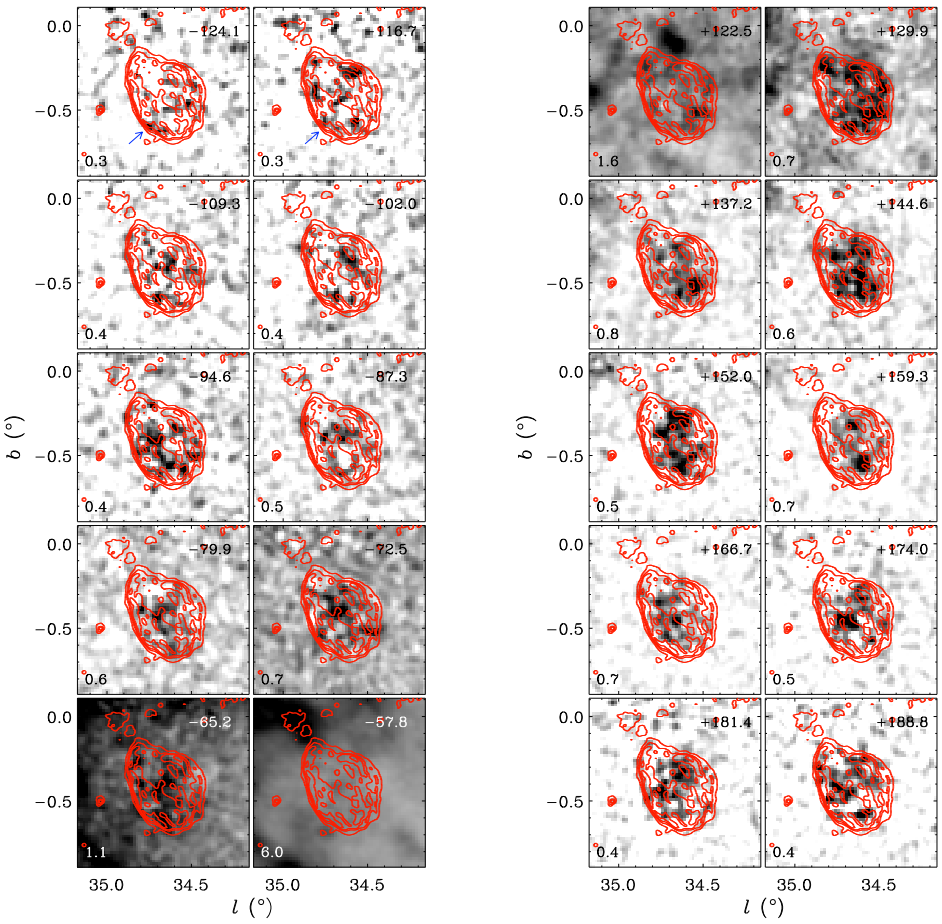

Figure 2.4. Channel maps of HV H I gas associated with the SNR W44 at negative (left) and positive (right) velocities in the I-GALFA H I data. The central LSR velocity of each panel is written at the upper right corner in km s^{-1}. The velocity width of one displayed channel is 3.68 km s^{-1}; this is binned by a factor of 20 from the raw data and has a measured RMS noise of 0.07 K. The H I brightness temperature in each gray scale ranges from 0 K (white) to the value (black) at the lower left corner of each panel in Kelvins. Radio continuum emission at 21 cm is shown by red contours as in Figure 2.3. The blue arrows in the first two panels indicate an emission feature described in Section 2.4.1.

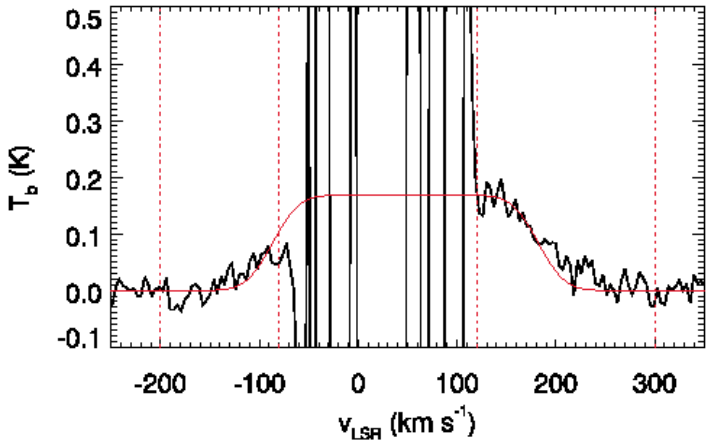

Figure 2.5. A fit to the average background-subtracted H I profile of W44. Low-velocity residual brightness fluctuations are as in Figure 2.1. The red solid line is a best fit to the profile. The red dotted lines mark the velocity range where the fit has been performed. See Section 2.4.1 for an explanation of the fit.

which the line profile becomes symmetric. For example, if we naively fit a Gaussian to the line profile, we obtain a central velocity of +59 km s^{-1}, which is considerably higher than the systemic velocity (+47 km s^{-1}) of the associated molecular cloud. We attribute the discrepancy to the asymmetric mass distribution of the H I shell. The implied asymmetry also makes it difficult to derive an accurate mass. But the uncertainty in the mass estimation is mainly due to the unobservable mass at low velocities, and, by fixing the central velocity, we can derive a reasonably accurate mass. The average line profile becomes flattened at velocities below +160 km s^{-1}, i.e., it does not rise steeply as one might expect when the high-velocity part ($\geq$ 160 km s^{-1}) is the tail of a Gaussian profile, which is consistent with Koo & Heiles (1995). If the H I shell is uniform and expanding at a constant speed $v_{\rm exp}$, then the average H I 21-cm line profile would appear as a square profile that extends from $-v_{\rm exp}$ to $+v_{\rm exp}$ centered at the systemic velocity v_0 (e.g., see Koo & Heiles 1991), i.e.,

$$T_{b,\rm square}(v) = \begin{cases} T_{b,\rm max} & \text{for } v_0 - v_{\rm exp} \leq v \leq v_0 + v_{\rm exp} \\ 0, & \text{otherwise} \end{cases} \tag{2.1}$$

where $T_{b,\rm max}$ is the maximum brightness temperature, which is proportional to the total mass in the shell (see below). But the shell probably does not coast at a constant speed, given non-uniformity/inhomogeneity of the ambient medium, turbulent motions produced by hydrodynamic instabilities, etc. We assume that the observed profile is composed of a flat profile convolved by a Gaussian profile, i.e.,

$$T_b(v) = \int_{-\infty}^{+\infty} \frac{T_{b,\rm square}(u)}{\sigma_v \sqrt{2\pi}} \exp\left[\frac{-(v-u)^2}{2{\sigma_v}^2}\right] du \tag{2.2}$$

where σ_v is the dispersion of random velocities related to the velocity at FWHM $\Delta v_{\rm FWHM}$ by $\sigma_v = \Delta v_{\rm FWHM}/2\sqrt{2\ln 2}$.

The fast-moving gas is clumpy and has broad lines. In the SNR W51C, for example, Koo & Moon (1997a) resolved individual clumps using the VLA and found

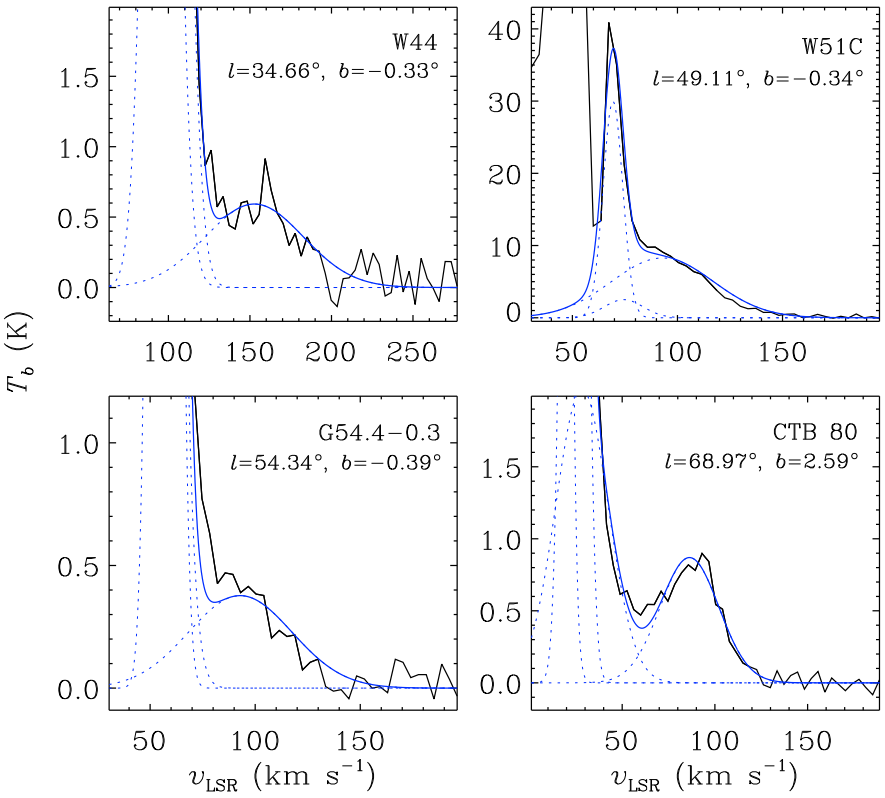

Figure 2.6. H I 21-cm spectra of some prominent HV clumps in individual SNRs (black lines). Their positions are given in the upper right corner of each panel. The HV parts of the spectra have been fitted by several Gaussian components, and the blue dotted and solid lines show the profiles of individual components and their sum, respectively. The components at the highest velocities are the ones related to the fast-expanding H I shells.

that their line profiles have FWHM of $\sim$ 40 km s^{-1}. In the I-GALFA survey, we could not completely resolve out clumps from the background emission in velocity space. But we see many clumps that appear as prominent protrusions. Figure 2.6 shows some examples of HV bumps in the tails of strong background emission. We fit the HV parts of these spectra with several Gaussian components. Our purpose is only to obtain the widths of the HV bumps, so the fit parameters of the low-velocity components are unimportant. We obtain suitable results using four components for CTB 80 and three for the others (Figure 2.6), and we find $\Delta v_{\rm FWHM} \approx 50$ km s^{-1} for the HV components in all four SNRs. We adopt $\Delta v_{\rm FWHM} = 50$ km s^{-1} as the characteristic value for the fit. The large velocity dispersion within the shell implies that the shell is dispersing, but its thickness will remain small compared to the radius of the shell until the very late stage of SNR evolution.

With the systemic velocity fixed at $v_0 \equiv +47$ km s^{-1}, we vary $T_{b,\rm max}$ and $v_{\rm exp}$. The fit was done using the IDL routine MPFIT (Markwardt 2009). The best fit profile is shown in Figure 2.5. Its parameters are $v_{\rm exp} = 135 \pm 2$ km s^{-1} and $T_{b,\rm max} = 0.168 \pm 0.005$ K. The H I mass is derived from the average column density obtained from the fit, i.e., $\bar{N}_{\rm HI} = 1.822 \times 10^{18}\, T_{b,\rm max} \times 2 v_{\rm exp}$ cm^{-2} considering both approaching and receding sides of the shell, by multiplying the area of W44. (Since the peak brightness temperature is only $\sim$ 0.2 K, we may assume that the H I emission is optically thin.) The derived H I mass is $393 \pm 13 M_\odot$, which implies a kinetic energy of $9.9 \pm 0.4 \times 10^{49}$ erg. These numbers agree with those of Koo & Heiles (1995) within 10–20%. The resulting dynamical age of the shell is $t \simeq 0.29 R_{\rm sh}/v_{\rm exp} \simeq 2.6 \times 10^4$ yr (Cioffi et al. 1988), where we used a geometrical mean radius (12.5 pc at 2.8 kpc; See Tables 2.2 and 2.3 for the adopted distances to the SNRs) as the radius of the SNR, $R_{\rm sh}$. This dynamical age is somewhat larger than the characteristic spin-down age of the pulsar. Assuming that this mass was initially inside the volume of the SNR, i.e., inside a sphere of geometrical radius of 12.5 pc, the mean density of hydrogen

nuclei in the ambient medium would be 1.9 ± 0.1 cm^{-3}. The initial explosion energy, $E_{\rm E}$, can be estimated from

$$E_{\rm E} = 6.8 \times 10^{43}\, {n_0}^{1.16}\, {R_{\rm sh}}^{3.16}\, {v_{\rm exp}}^{1.35} \quad \text{erg}, \tag{2.3}$$

where n_0 is the ambient density of hydrogen nuclei in cm^{-3}, $R_{\rm sh}$ is in pc, and $v_{\rm exp}$ is in km s^{-1} (Cioffi et al. 1988). We assume solar metallicity. Substituting the derived values, i.e., $n_0 = 1.9$ cm^{-3}, $R_{\rm sh} = 12.5$ pc, and $v_{\rm exp} = +135$ km s^{-1}, we have $E_{\rm E} = 3.2 \pm 0.1 \times 10^{50}$ erg. This is the energy required to heat and accelerate more or less uniformly distributed atomic gas. Since there is also fast-expanding ($\sim +30$ km s^{-1}), dense molecular gas accelerated by SN blast wave (Reach et al. 2005; Froebrich et al. 2011), some fraction of the total SN energy should have been used up for heating and accelerating the molecular gas. It would be interesting to derive the kinetic energy of shocked H_2 filaments and compare it to that of the H I shell.

2.4.2 G54.4−0.3 (HC 40)

Previous studies

G54.4−0.3 is a shell-type SNR of circular shape with a diameter of 40′. The shell is not complete, and its radio continuum brightness is not uniform (see the contour map in Figure 2.3; Junkes et al. 1992a). In the southeastern part of the remnant, the circular portion of the shell is missing, and instead faint continuum structures are visible connected to the tips of the bright ends. This probably indicates that the SNR blew out in this direction, presumably on encountering a rarefied medium there, and the shell was disrupted in the process. Junkes et al. (1992a) carried out CO observations and suggested an association with a molecular cloud at $v_{\rm LSR} = +36$ to $+44$ km s^{-1}. They proposed a distance of 3 kpc using the rotation curve of Burton (1988). Case & Bhattacharya (1998) adjusted this distance by adopting a revised

Table 2.2

Physical Parameters of Supernova Remnants with Fast-Expanding H I Shells

Name	d (kpc)	$R_{\rm sh}$ (pc)	v_0 (km s^{-1})	$v_{\rm exp}$ (km s^{-1})	Age (10^4 yr)	H I Mass ($M_\odot$)	K.E. (10^{49} erg)	n_0 (cm^{-3})	$E_{\rm E}$ (10^{50} erg)	P?[a]	M?[b]
W44	2.8	12.5	47	135(2)	2.63(0.04)	393(13)	9.9(0.4)	1.9(0.1)	3.2(0.1)	y	y
W51C[c]	6	6	62	96(6)	1.8(0.1)	>1200	>17	~ 100	~ 19	···	y
G54.4−0.3	3.3	19.2	40	59(6)	9.2(1.0)	580(150)	2.8(0.9)	0.79(0.20)	1.5(0.5)	···	y
CTB 80[d]	2	18.6	13	72(3)	7.7(0.3)	1050(210)	7.6(1.5)	1.5(0.3)	3.8(0.9)	y	···

Note. The distance (d), radius ($R_{\rm sh}$), and systemic velocity (v_0) are adopted values, so that they do not have errors. The errors in W44 and G54.4−0.3 are formal errors from the fit.

[a]Detection (y) of associated pulsars. References are Wolszczan et al. (1991) and Kulkarni et al. (1988) for W44 and CTB 80, respectively.

[b]Detection (y) of associated molecular clouds. References are Wootten (1977), Koo & Moon (1997b), and Junkes et al. (1992a) for W44, W51C, and G54.4−0.3, respectively.

[c]The H I shell parameters are from Koo & Moon (1997a). W51C is interacting with a molecular cloud, and only a lower limit to the H I mass has been obtained. We adopt 100 cm^{-3} as a characteristic density of the cloud.

[d]The H I shell parameters are from Koo et al. (1990). Koo et al. (1990) obtained an H I mass of 1200 $M_\odot$ by fitting a Gaussian profile to the observed H I mass distribution. But an independent estimate of the mass of the shell is available from infrared studies (900 $M_\odot$; see Koo et al. 1990). We adopt the mean of the two as the mass of the expanding shell.

rotation curve with $R_\odot = 8.5$ kpc and $\Theta_\odot = 220$ km s^{-1} and obtained 3.3 kpc. If we use the rotation curves of Brand & Blitz (1993) or Levine et al. (2008), the near-side kinematic distance corresponding to the systemic velocity of +40 km s^{-1} in this direction is 3.9 and 3.1 kpc, respectively. We adopt the 3.3 kpc distance of Case & Bhattacharya (1998) in this paper. There are several H II regions in this area at about the same distance, including the compact H II region just outside the northwestern boundary of the remnant (Junkes et al. 1992b). Junkes (1996) observed the remnant with *ROSAT* and derived an absorbing hydrogen column density of 1×10^{22} cm^{-2} and a plasma temperature of 2×10^7 K. Boumis et al. (2005) detected optical emission lines in the northwestern edge of the shell and derived an absorbing hydrogen-nuclei column density of 2.9–4.0 $\times 10^{22}$ cm^{-2}. KH91 detected fast-moving H I gas at velocities +91 — +108 km s^{-1}.

New Results

This SNR has some of the most prominent H I shell structure in our sample. Figure 2.7 shows H I channel images of G54.4−0.3 at $v_{\rm LSR} = +53$ to +108 km s^{-1}. At the highest positive velocities, e.g., $v_{\rm LSR} = +100$ km s^{-1}, the H I gas is confined to the central area of the remnant, whereas at lower velocities, we see a well-defined ring structure as well as some emission filling the central area. This velocity structure indicates that the HV gas is the receding portion of an expanding shell. The shell has non-uniform brightness. A prominent feature is the bar-like structure extending from the center to the southwestern at $v_{\rm LSR} = +78$ to +93 km s^{-1} (blue arrow in a panel at +89 km s^{-1}). Its northeastern tip appears as a bright spot at ($54\overset{\circ}{.}35, -0\overset{\circ}{.}30$) at $v_{\rm LSR} = +82$ — +89 km s^{-1}. At low velocities, e.g., at $v_{\rm LSR} = +64$ — +78 km s^{-1}, we see some correspondence between H I and radio continuum structures. First, the same southeastern portion of the H I shell is also weak and missing as in the continuum shell. Second, there is faint but enhanced H I emission coinci-

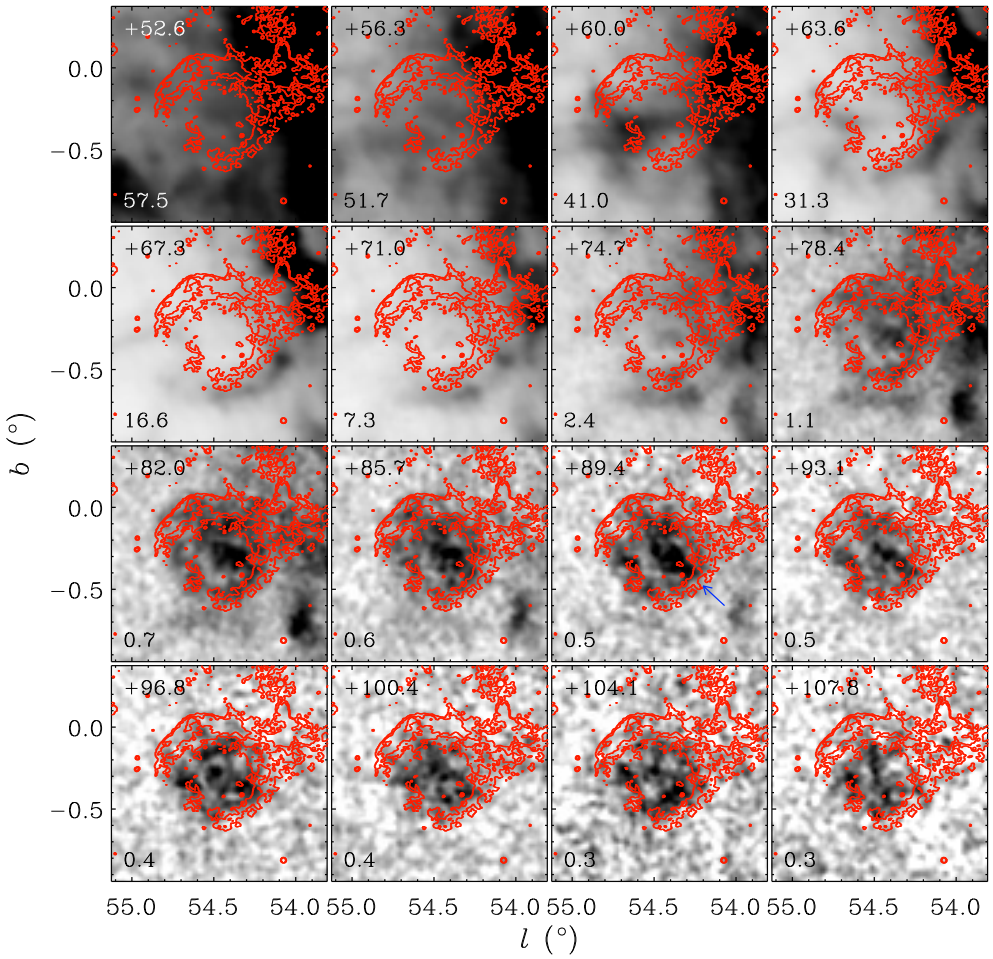

Figure 2.7. Channel maps of HV H I gas associated with the SNR G54.4−0.3 in the I-GALFA H I data. As in Figure 2.4, the central LSR velocity of each panel is shown in the upper left corner in km s^{-1}, and the velocity width of one channel is 3.68 km s^{-1}. The H I brightness temperature in each gray scale ranges from 0 K (white) to the value (black) at the lower left corner of each panel in Kelvins. Radio continuum morphology of the SNR is shown by red contours as in Figure 2.3. The blue arrow in the +89.4 km s^{-1} panel marks an emission feature described in Section 2.4.2.

dent with the continuum shell at ≥ 70 km s^{-1}. Third, along the southwestern SNR shell, there is a larger filamentary H I structure just outside it at $v_{\rm LSR} = +64$ to $+78$ km s^{-1}. This external H I feature has the same curvature as the SNR shell, so it might be associated with the SNR too. Perhaps this is the boundary of the stellar wind bubble produced by the progenitor star, although it is not obvious how we can see the SNR shell inside a wind bubble.

We derive the mass of the G54.4−0.3 H I shell in a similar fashion to W44, but using only positive velocities. We adopt $\Delta v_{\rm FWHM} = 50$ km s^{-1} and assume a systemic velocity of $+40$ km s^{-1}. The best-fit profile, shown in Figure 2.8, uses $v_{\rm exp} = 59 \pm 6$ km s^{-1} and an H I mass of $580 \pm 150 M_{\odot}$ at 3.3 kpc. The corresponding kinetic energy is $2.8 \pm 0.9 \times 10^{49}$ erg. The resulting dynamical age of the shell is $t \simeq 0.29 R_{\rm sh}/v_{\rm exp} \simeq 9.2 \times 10^4$ yr, where we used $R_{\rm sh} = 19.2$ pc ($20'$). Again assuming that this mass was initially inside the volume of the SNR, the mean density of hydrogen nuclei in the ambient medium would be 0.79 ± 0.20 cm^{-3}. With the above parameters, we obtain $E_{\rm E} = 1.5 \pm 0.5 \times 10^{50}$ erg. This is considerably smaller than the canonical value of 1×10^{51} erg but not unreasonable.

Others

G49−0.7 (W51C) is a middle-aged, shell-type SNR interacting with a molecular cloud. Koo & Moon (1997a,b) obtained high-resolution H I and CO observations and developed a model in which the fast-moving H I gas is produced by the SNR shock propagating into a molecular cloud. The SNR is one of the most luminous γ-ray sources in the Galaxy (Abdo et al. 2009). The I-GALFA results for the HV H I gas in Figures 2.1–2.3 agree with previous results.

G69.0+2.7 (CTB 80) is one of the first infrared SNRs detected by *IRAS* (Fesen et al. 1988). It appears as a large ($\sim 1^{\circ}$), spherical shell-type SNR in IR while, in radio continuum, only the northern portion of the shell is bright due to the interaction

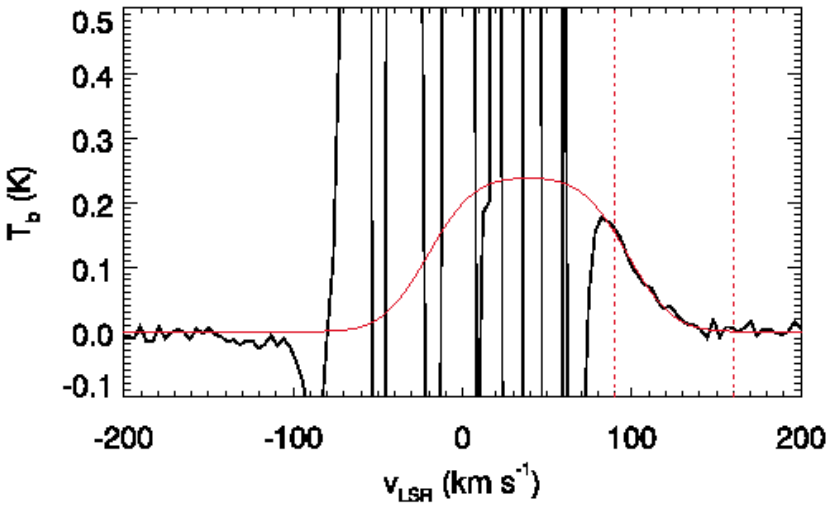

Figure 2.8. A fit to the average H I profile of G54.4−0.3. Low-velocity residual brightness fluctuations are as in Figure 2.1. The red solid line is a best fit to the profile. The red dotted lines mark the velocity range where the fit has been performed. See Section2.4.1 for an explanation of the fit.

with the pulsar. Koo et al. (1990, 1993) carried out H I studies using the Arecibo telescope and the VLA and confirmed the large size of the SNR shell and its old age ($\sim 1 \times 10^5$ yr). Again, the I-GALFA HV H I results in Figures 2.1–2.3 agree with previous results.

2.5 Discussion

2.5.1 Properties of H I SNRs

We have detected 4 SNRs with fast expanding H I shells in the I-GALFA survey area. Table 2.2 summarizes their parameters: distance d, radius $R_{\rm sh}$, systemic velocity v_0, expansion speed $v_{\rm exp}$, dynamical age, H I mass, kinetic energy, ambient density n_0, and initial explosion energy $E_{\rm E}$. The table also lists whether the remnant has an associated pulsar and whether it is interacting with a molecular cloud. The parameters of W44 and G54.4−0.3 are those derived in this work, whereas those of W51C and CTB 80 are from previous studies.

There are several points to make. First, all 4 SNRs are middle-aged (1.8–9.5 $\times$ 10^4 yr). Second, the ambient densities are $\gtrsim 1$ cm^{-3}, considerably larger than the densities of either the warm or hot diffuse ISM filling most of the interstellar volume. In particular, three SNRs are interacting with molecular clouds. Third, two SNRs are the remnants of core-collapse SNe with associated pulsar wind nebulae (PWNe). The other two remnants, G54.4−0.3 and W51C, do not have associated PWNe, but their interactions with molecular clouds suggests they also likely have massive progenitors. In summary, the SNRs with H I shells (hereafter H I SNRs) that are detected are middle-aged SNRs of probable CCSN origin interacting with a relatively dense medium.

The dynamical evolution of middle-aged SNRs in a uniform medium was studied in detail by Cioffi et al. (1988), who derived analytic expressions for radius $R_{\rm sh}$ and

expansion velocity $v_{\rm exp}$ that describe the results of their one-dimensional numerical simulations. Koo & Kang (2004) proposed somewhat simpler but still accurate forms of the equations of Cioffi et al. (1988).[4] We find it useful to introduce a parameter $\delta \equiv n_0 {E_{51}}^{-0.861}$ where n_0 is the density of hydrogen nuclei in the ambient medium divided by 1 cm^{-3}, and E_{51} is the SN energy released to the ISM in units of 10^{51} erg. Note that δ is dimensionless. The advantage of introducing δ is that the radius and velocity of middle-aged SNRs are now related by

$$R_{\rm sh} = 25.7 \delta^{-0.367} {v_{\rm exp,2}}^{-3/7} \quad {\rm pc}, \tag{2.4}$$

where $v_{\rm exp,2} \equiv (v_{\rm exp}/100 \text{ km s}^{-1})$. This equation is obtained by combining equations (5)–(8) of Koo & Kang (2004). (Note that this is just another expression of equation (3) except that their numerical coefficients differ by 2%.) In the ($R_{\rm sh}$, $v_{\rm exp}$) plane, H I SNRs evolve along a line satisfying the above equation. In terms of δ, the expansion velocity of H I SNRs is given by (Eq. 6 of Koo & Kang 2004)

$$v_{\rm exp} = 179\, \delta^{1/7}\, {E_{51}}^{0.194} \left(\frac{11}{10} \frac{t}{t_{\rm sf}} - \frac{1}{10} \right)^{-7/10} \quad {\rm km\ s^{-1}}, \tag{2.5}$$

where the "shell formation time" $t_{\rm sf}$ representing the onset of the formation of H I shell is defined by (Cioffi et al. 1988)

$$t_{\rm sf} \equiv 3.61 \times 10^4\, {n_0}^{-4/7} {E_{51}}^{3/14} \text{ yr}. \tag{2.6}$$

As pointed out by Koo & Kang (2004), the maximum disagreement between the equations (4)–(5) and the original equations (3.22)–(3.23) of Cioffi et al. is less than 0.1% during $t \sim (1 - 13)\, t_{\rm sf}$. The radius and velocity are now functions of δ, E_{51}, and $t/t_{\rm sf}$ instead of n_0, E_{51}, and t. And since the dependence of $v_{\rm exp}$ on E_{51} is weak, a single grid can be drawn in the ($R_{\rm sh}$, $v_{\rm exp}$) plane to describe the evolution of H I SNRs in different physical environments.

[4] There was a typo in equation (8) of Koo & Kang (2004): the index "-1/14" should be read as "1/14."

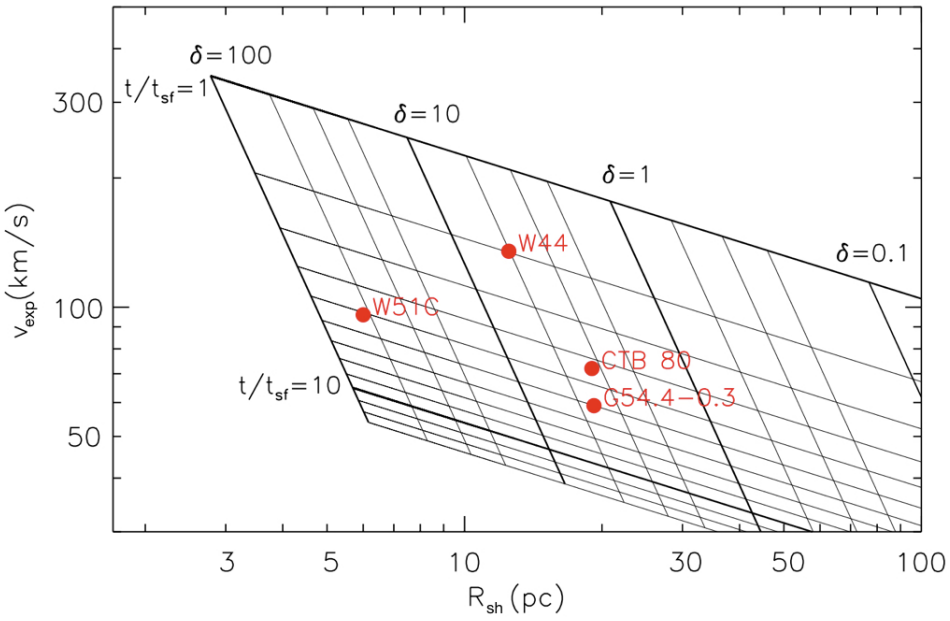

Figure 2.9. Radius-velocity relation of H I SNRs. The grid is for $E_{51} = 1$. The grid shifts along lines of constant δ for different E_{51} but not much: e.g., for $E_{51} = 0.1$, the lines of constant $t/t_{\rm sf}$ shift down by 36%. The thin grid lines in δ are drawn at 20, 30, and 50% of the thick-grid intervals, while those in $t/t_{\rm sf}$ are at every 10%. The four H I SNRs identified in the I-GALFA survey are marked.

Figure 2.9 shows how the radius and velocity of H I SNRs evolve in time ($t/t_{\rm sf}$) for a given δ. The SNR develops a fast-expanding H I shell at $t/t_{\rm sf} = 1$, which expands and slows down along a line of constant δ as it evolves. For example, suppose an SNR has $E_{51} = 1$ in a uniform medium with $n_0 = 1$, so that $\delta = 1$. Then the SNR has an H I shell of ($R_{\rm sh}$, $v_{\rm exp}$) = (20 pc, +179 km s^{-1}) at $t/t_{\rm sf} = 1$ and ($R_{\rm sh}$, $v_{\rm exp}$) = (40 pc, +34 km s^{-1}) at $t/t_{\rm sf} = 10$, where $t_{\rm sf} = 3.61 \times 10^4$ yr. The H I SNRs identified in the I-GALFA survey have radii of 6–19 pc and expansion velocities +59 — +135 km s^{-1}, or $\delta = 5$–50 and $t/t_{\rm sf} = 2$–9. The expansion velocities of the detected H I shells are all greater than +50 km s^{-1}, which is necessary to be clearly discernible from the Galactic background emission (see next section). It is also worth noting that no large H I SNRs expected in the diffuse ISM have been detected, i.e., there are no H I SNRs where $\delta < 1$ in Figure 2.9. This may be either because such SNRs are rare or because such SNRs are faint in radio continuum and "missed" in the current catalog of SNRs. We will discuss this further in next section.

Table 2.3

Distances to the SNRs in the I-GALFA Survey Area

G-Name	Coordinates		Type	Distance		Radius	$v_{\rm det,min}$[a]	Reference(s)
	ℓ (°)	b (°)		Quoted (kpc)	$\Sigma - D$ (kpc)	(pc)	(km s^{-1})	
G31.9+0.0	31.89	0.03	S	8.5	5.4	7.3	59	Green (2009a)
G32.1−0.9	32.12	−0.90	C?	4.6	···	26.8	72	Folgheraiter et al. (1997)
G32.4+0.1	32.41	0.11	S	17	33.9	14.8	76	Yamaguchi et al. (2004)
G32.8−0.1	32.81	−0.06	S?	∼7.1	6.3	17.6	50	Koralesky et al. (1998); Boumis et al. (2009)
G33.2−0.6	33.18	−0.55	S	···	10.1	26.4	84	···
G33.6+0.1	33.70	0.01	S	7.8[b]	5.1	11.3	53	Frail & Clifton (1989); Green (2004, 2009a)
G34.7−0.4	34.67	−0.39	C	2.8[b]	···	12.5	89	Caswell et al. (1975); Green (2004, 2009a)
G35.6−0.4	35.59	−0.50	S	3.7	7.6	6.9	76	Green (2009b)
G36.6−0.7	36.59	−0.69	S?	···	···	···	53	···
G36.6+2.6	36.58	2.60	S	···	20.5	44.3	52	···
G39.2−0.3	39.24	−0.32	C	8.5	···	8.6	64	Lee et al. (2009)
G39.7−2.0	39.69	−2.39	?	6.0	···	74.0	50	Green (2009a)
G40.5−0.5	40.52	−0.51	S	3.8[c]	6.1	12.2	64	Yang et al. (2006)
G41.1−0.3	41.11	−0.31	S	10.6[c]	6.1	5.2	94	Jiang et al. (2010)
G42.8+0.6	42.82	0.64	S	∼6	10.3	20.9	50	Marsden et al. (2001)
G43.3−0.2	43.27	−0.19	S	10	4.8	5.0	87	Green (2009a)
G43.9+1.6	43.91	1.61	S?	···	5.7	49.7	50	···
G45.7−0.4	45.69	−0.39	S	···	9.1	29.1	76	···
G46.8−0.3	46.77	−0.30	S	∼7.8	5.8	16.9	62	Green (2009a)
G49.2−0.7	49.14	−0.60	S?	6	1.9	26.2	51	Koo et al. (1995)
G53.6−2.2	53.63	−2.26	S	2.8	6.6	12.4	55	Giacani et al. (1998); Green (2009a)
G54.1+0.3	54.09	0.26	C	6	···	10.8	54	Kim et al. (2013)
G54.4−0.3	54.47	−0.29	S	3.3[d]	3.7	19.2	52	Junkes et al. (1992a); Case & Bhattacharya (1998)
G55.0+0.3	55.11	0.42	S	14	23.1	35.3	79	Matthews et al. (1998); Green (2009a)
G55.7+3.4	55.60	3.51	S	···	14.3	47.8	76	···
G57.2+0.8	57.30	0.83	S?	···	14.3	25.0	74	···
G59.5+0.1	59.58	0.12	S	···	11.1	24.2	101	···

Continued on Next Page...

Table 2.3 – Continued

G-Name	Coordinates		Type	Distance		Radius	$v_{\rm det,min}$[a]	Reference(s)
	ℓ	b		Quoted	$\Sigma - D$			
	(°)	(°)		(kpc)	(kpc)	(pc)	(km s^{-1})	
G59.8+1.2	59.81	1.20	?	···	14.1	36.7	72	···
G63.7+1.1	63.79	1.17	F	···	···	···	···	···
G65.1+0.6	65.27	0.30	S	9	6.8	87.8	93	Green (2009a)
G65.3+5.7	65.18	5.66	S?	0.8	2.1	31.7	51	Boumis et al. (2004); Green (2009a)
G65.7+1.2	65.72	1.21	F	1.5	···	4.8	51	Kothes et al. (2004); Green (2009a)
G67.7+1.8	67.74	1.82	S	∼12	18.0	23.4	79	Mavromatakis et al. (2001)
G68.6−1.2	68.60	−1.20	?	···	19.2	64.2	50[e]	···
G69.0+2.7	68.84	2.78	?	2	1.8	23.3	50	Koo et al. (1990)
G69.7+1.0	69.69	1.00	S	2[f]	13.2	4.4	50	Yoshita et al. (2000)
G73.9+0.9	73.91	0.88	S?	∼1.3	6.4	5.1	51	Lozinskaya et al. (1993)
G74.0−8.5	73.98	−8.56	S	0.44	1.2	12.3	53	Green (2009a)
G74.9+1.2	74.94	1.14	F	6.1	···	6.1	75	Kothes et al. (2003); Green (2009a)

Note. Distance with a symbol of '∼' denotes that we adopt the average of possible distances given by reference(s).

[a]Minimum expansion velocity for detection.

[b]Recalculated by Green (2004) assuming a flat rotation curve with $R_\odot = 8.5$ kpc and $\Theta_\odot = 220$ km s^{-1}.

[c]Recalculated by this work using the Galactic rotation curve of Brand & Blitz (1993) with $R_\odot = 8.5$ kpc and $\Theta_\odot = 220$ km s^{-1}.

[d]Recalculated by Case & Bhattacharya (1998) assuming a flat rotation curve with $R_\odot = 8.5$ kpc and $\Theta_\odot = 220$ km s^{-1}.

[e]This remnant is outside the assumed disk radius of 15 kpc, so we simply adopt 50 km s^{-1} as the minimum velocity.

[f]Yoshita et al. (2000) suggested that G69.7+1.0 will be at a similar distance as CTB 80, since the column density of the ISM between us and G69.7+1.0 is analogous with that of CTB 80. In this paper, we adopt 2 kpc for both CTB 80 and G69.7+1.0.

2.5.2 Visibility and Statistics of H I SNRs

The visibility or detectability of SNRs in the H I 21-cm line was investigated by Koo & Kang (2004). An important constraint on the visibility of H I SNRs is that they should be in the "right" positions in the Galaxy where the line-of-sight velocities of expanding H I shells can easily exceed the maximum or minimum LSR velocities of the Galactic background H I emission, e.g., along the loci of tangential points in the inner Galaxy. For example, W51C is in a high-visibility location, because its systemic velocity (+62 km s^{-1}) is close to the maximum velocity ($\sim$ +90 km s^{-1}; see Figure 2.2) of the background emission in this direction ($\ell = 49\overset{\circ}{.}2$). In contrast, W44 is in a low-visibility location: its systemic velocity (+47 km s^{-1}) is much less than the maximum velocity (+130 km s^{-1}) in this direction ($\ell = 34\overset{\circ}{.}7$). Apparently, W44 is relatively young and has the largest expansion velocity, so that both its approaching and receding parts can be seen.

The locations of the SNRs in the I-GALFA area are marked in Figure 2.10 (left), with filled circles for the 4 H I SNRs. Table 2.3 lists our adopted distances, where the fifth column gives the distances that are considered to be reliable. Twenty-eight SNRs have reliable distances, half of which are from the compilation by Green (2009a). The other half are from our own literature search, with references listed in the last column. The sixth column gives distances estimated using the surface brightness – diameter ($\Sigma - D$) relation (e.g., Case & Bhattacharya 1998; Arbutina et al. 2004; Guseinov et al. 2003). For this work, we adopt the Case & Bhattacharya (1998) version. The $\Sigma - D$ relation has considerable dispersion, and its applicability has been criticized (e.g., Green 2004). But without any other estimates, it still provides a useful reference. We use reliable distances wherever possible and $\Sigma - D$ distances for other SNRs.

The background grey-scale map in Figure 2.10 (left) shows the minimum shell expansion velocity for detection, $v_{\rm det,min}$. The Galactic disk is assumed to be axi-

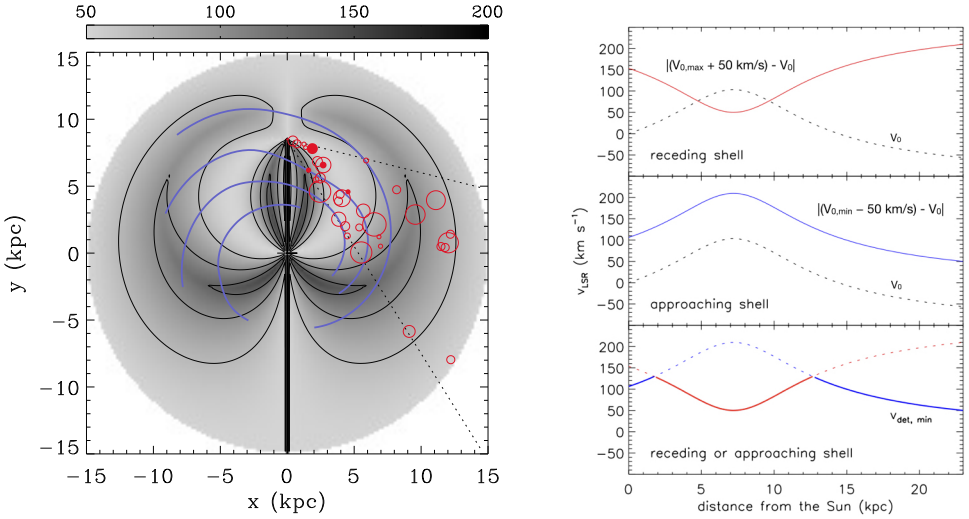

Figure 2.10. (left) Distribution of $v_{\rm det,min}$, the minimum expansion velocity of a fast-expanding SNR H I shell for detection. Areas with higher minimum expansion velocities are darker. The scale bar at the top displays velocity scales in a unit of km s^{-1}. Contour levels are drawn at 70, 100, and 130 km s^{-1}. The Sun is located at $x = 0.0, y = 8.5$ kpc. The dotted lines mark the boundaries of the I-GALFA survey at $b = 0°$, i.e., $\ell = 32°$ to $77°$. The blue curved lines represent the four spiral arms of Taylor & Cordes (1993). The locations of the SNRs in the I-GALFA area are marked by red circles with diameters proportional to SNR size. The SNRs with fast-expanding H I shells are marked by the filled circles. (right) One-dimensional velocity profiles at $\ell = 32°$. Minimum expansion velocities required for the detection of receding (top frame) and approaching (middle frame) portions of the shell are shown together with the systemic LSR velocity (v_0) as a function of distance from the Sun. $v_{\rm det,min}$ is the smaller of the two velocities (bottom frame). (See text for details.)

symmetric with radius 15 kpc and a flat rotation curve with $R_\odot = 8.5$ kpc and $\Theta_\odot = 220$ km s^{-1}. An expanding H I shell is considered to be visible if the LSR velocity of its receding endcap, which is the sum of the systemic LSR velocity and the expansion velocity, is greater than the maximum LSR velocities allowed by circular rotation in that direction by more than 50 km s^{-1} or vice versa. This appears to be conservative considering that the turbulent velocity dispersion of the warm neutral medium is 27 km s^{-1} (Heiles & Troland 2003) and that the non-circular velocities due to spiral shocks are typically 20 km s^{-1} (e.g., Roberts 1969). But note that the H I emission from fast-expanding SNR shells appears as very weak broad wings superposed on the Gaussian tails of background emission; in Figure 2.6, for example, the maximum LSR velocities in the directions of the four SNRs according to the flat rotation curve are, in the order of increasing Galactic longitude, +94, +54, +42, and +15 km s^{-1}, respectively. H I shells along the tangent points in the inner Galaxy have small $v_{\rm det,min}$ (~ 50 km s^{-1}) because their positive-velocity wings can be easily detected. The H I shells near the outer boundary of the disk in the survey area also have small $v_{\rm det,min}$, but, in this case, it is because their negative velocity wings can be easily detected. In order to help the understanding, Figure 2.10 (right) shows the variation of $v_{\rm det,min}$ for SNRs in the direction at $\ell = 32^\circ$. In the top and middle frames, the dotted line shows how the systemic LSR velocity (v_0) varies with distance from the Sun due to Galactic rotation. Note that the maximum and minimum systemic LSR velocities in this direction are 103 and -56 km s^{-1}, respectively. This gives an approximate velocity range of the background H I emission. Therefore, for the receding portion of an expanding SNR shell to be detectable, its expansion velocity should be larger than $(103+50)$ km s$^{-1}-v_0$, where v_0 is the systemic velocity of the shell (red line in the top frame). On the other hand, for the approaching portion to be detectable, which will appear as a negative-velocity wing, the expansion velocity should be larger than $|(-103-50)$ km s$^{-1}-v_0|$ (blue line in the middle frame).

For just one part of the shell detectable, the required expansion velocity will be the smaller of the two (thick line in the bottom frame). Figure 2.10 shows that three SNRs (W51C, G54.4−0.3, CTB 80) are located where the $v_{\rm det,min}$ is relatively small, i.e., 50 km s^{-1}, whereas W44 is located in a region where $v_{\rm det,min} \sim 90$ km s^{-1}. Table 2.3 lists $v_{\rm det,min}$ at the position of each SNR.

In Figure 2.10, there are many SNRs that are *not* detected in H I 21-cm line in spite of their favorable locations in areas where $v_{\rm det,min}$ is small. They could be either too young or too old to have an associated fast-expanding H I shell. Their nature can be inferred in Figure 2.11, which is same as Figure 2.9, but we now also mark the SNRs without detected H I shells using their minimum velocities for detection. In Figure 2.11, an SNR without detected H I can be either an old SNR with a velocity less than $v_{\rm det,min}$ or a young SNR above the grid, i.e., with velocity greater than that at $t/t_{\rm sf} = 1$. Note that if an SNR is above the grid, it means that the remnant is in adiabatic phase and does not have an H I shell. It is "too young," i.e., younger than $t_{\rm sf}$ in equation (6). Note that $t_{\rm sf}$ is large when the ambient density is low. For small SNRs, e.g., those with $R_{\rm sh} \leq 10 - 20$ pc, the latter possibility is more likely unless they are in a dense environment, such as a molecular cloud. For larger SNRs, both possibilities are likely. Further observational studies will be helpful to address the nature of such SNRs individually.

As a final comment, our study in this chapter has targeted *known* SNRs, but there could be many missing SNRs. The estimated SN rate in our Galaxy ranges from 1.4 to 5.8 $\times 10^{-2}$ yr^{-1} (Li et al. 2011). If we adopt the recent estimate from the Lick Observatory Supernova Search, $2.84 \pm 0.60 \times 10^{-2}$ yr^{-1} (Li et al. 2011), the total number of radio SNRs in the Galaxy would be ~ 2800, assuming 1×10^5 yrs of visible radio continuum emission. Then, simply using the geometrical fraction of the survey area, which is 18% for a Galactic disk radius of 15 kpc, the expected number of radio SNRs in the survey area is ~ 500. Therefore, the number of known SNRs (39) is only

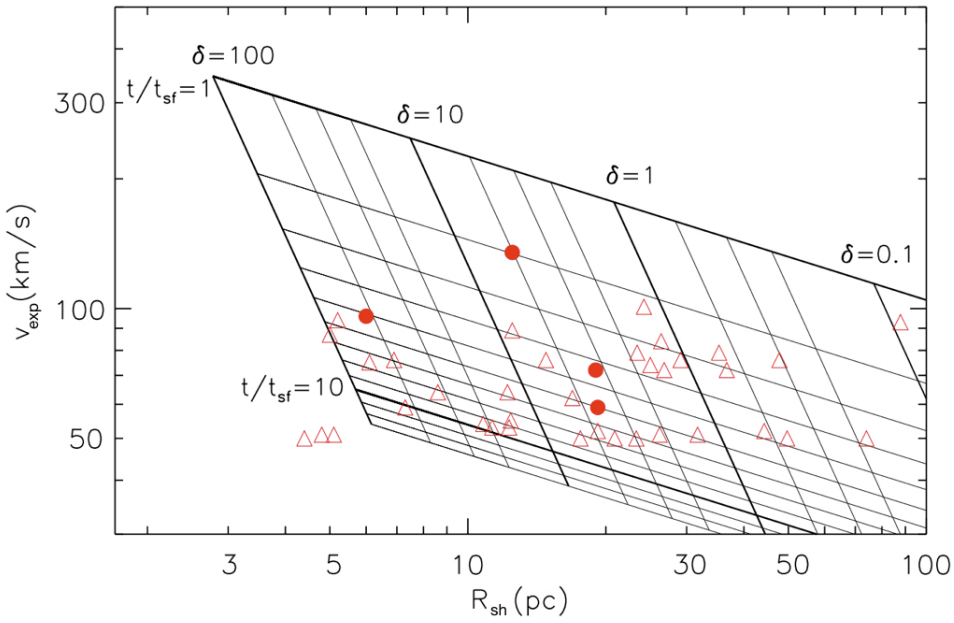

Figure 2.11. Same as Figure 2.9 but with all SNRs not seen in I-GALFA H I also marked (empty triangles). The velocities of the latter SNRs are the minimum velocities of detection for their hypothetical H I shells. The four SNRs with detected fast-expanding H I shells (filled circles) are shown with their measured expansion velocities.

8% of the expected population. This small fraction could be due to several factors: faintness of old SNRs in radio continuum, confusion due to Galactic background emission, collective explosions of CCSNe that produce supershells instead of SNRs, etc. (see Koo & Kang 2004; Higdon & Lingenfelter 2005; Brogan et al. 2006). So in principle, there could be many old SNRs or supershells not visible in radio continuum but visible in the H I 21-cm line, and it may be worthwhile to search for such H I features.

2.6 Summary

The I-GALFA survey provides fully-sampled H I data covering the Galactic plane between longitudes 32 to 77 degrees and latitudes −10 to +10 degrees. The high resolution ($4'$) and high sensitivity (0.2 K) of the data provide an opportunity to investigate small-scale, faint H I emission in the diffuse ISM. In this paper, we have explored the I-GALFA data toward the all known 39 SNRs in order to search for associated fast-expanding H I shells. Our main results are as follows:

1. Among the 39 SNRs in the survey area, four SNRs show associated high-velocity (HV) H I emission. These four SNRs were classified by KH91 as rank 3 SNRs with excess emission at the highest positive velocities in their low-resolution ($30'$) H I study. KH91 listed another SNR (W50) as a candidate with associated HV H I emission out of 26 SNRs known in the survey area at that time. But the high-resolution I-GALFA data show that the emission extends well beyond the SNR boundary, so we consider it not associated with the SNR. Surprisingly, we have not detected associated HV H I emission in any of the ten SNRs discovered since the work of KH91.

2. The four SNRs where we have detected physically associated HV H I gas are G34.7−0.4 (W44), G49.2−0.7 (W51C), G54.4−0.3 (HC40), and G69.0+2.7 (CTB 80). Their velocity structures indicate that the HV H I gas is in portions of

expanding shells. In the SNR W44, we see H I emission from both receding and approaching portions of the shell, which is the first ever such detection. In the other SNRs, we could see only the receding portions of the shells. The SNR G54.4−0.3 shows highly circularly symmetric H I emission that matches very well with its radio continuum morphology. There is a ring structure lying just outside the SNR boundary, which could be a pre-existing structure formed by the progenitor. We discuss the properties of the expanding H I shells in these two SNRs and derive their physical parameters. The other two SNRs have been studied previously in detail. The I-GALFA results are consistent with those previous studies.

3. The four SNRs with associated fast-expanding H I shells are all middle-aged SNRs with $t = 1.8$–9.5×10^4 yr (Table 2.2). The expansion velocities of the shells range from 59 to 135 km s^{-1}. Notably, their estimated ambient densities are all $\gtrsim 1$ cm^{-3}, significantly higher than that of the warm or hot ISM filling most of interstellar space. Two of them have associated PWN indicating that they are the remnants of CCSNe. The other two do not have PWN but are interacting with molecular clouds, so they are also likely the remnants of CCSNe. Therefore, the SNRs with H I shells (H I SNRs) that are detected are middle-aged SNRs of probable CCSN origin interacting with a relatively dense medium. Large H I SNRs in the diffuse ISM could be detected in principle, but they have not found.

4. The visibility of H I SNRs depends on their location in the Galaxy. Three of the four detected H I SNRs (excluding W44) are located where the visibility is favorable. On the other hand, many SNRs are *not* detected in the H I 21-cm line despite having favorable locations. They could be either too young or too old to have an associated fast-expanding H I shell. We present a diagram (Figure 2.11) that can be used to infer the nature of these SNRs.

Chapter 3

H I Shells/Supershells in the I-GALFA Survey Area

3.1 Abstract

We carry out a systematic study of H I shells and supershells in the first Galactic quadrant ($\ell \approx 32°$ to $77°$, $b \approx -10°$ to $+10°$) using the I-GALFA H I 21-cm survey data. The high-resolution ($4'$) and high sensitivity (0.2 K) of the survey provide us an opportunity to exploit the true nature of the sources detected in previous low-resolution studies and also to identify weak or distant shells that were not detectable before. Our work is composed of two parts: (1) confirm the objects in the low-resolution ($36'$) catalog of Heiles (1979) and (2) search for new shell structures in the I-GALFA data. We have identified thirty-eight H I shells/supershells in the survey area: thirteen are the previously known Heiles' shells while twenty-five are new shell candidate. Their geometric mean diameter and velocity extent have about $1°$–$13°$ and 7–65 km s^{-1}, respectively. The high-resolution I-GALFA images show that some of them, mostly in the inner Galaxy, are complicated with other chimney or more than one shell, and some might be located near active star-forming region(s).

For all objects found, we estimate the kinematic distances, radii, heights from the Galactic midplane (if available), and explosion energies. Fifteen objects are likely to be "supershells" which require enormous explosion energy ($\geq 3 \times 10^{52}$ erg). We compare the Galactocentric distribution of H I shells/supershells with those of H II regions and giant molecular clouds. The result of our comparison implies that many inner Galactic H I supershells are missing in our shell list, and we suggest that many supershells there had broken through the disk and evolved into "chimneys" or "worms." We also present the result of investigations on the association of H I shells with molecular clouds.

3.2 Introduction

The ISM maintains many great and small expanding neutral atomic shells which are the interstellar material, swept-up by supersonic shock (e.g., Heiles 1979, 1984; McClure-Griffiths et al. 2002; Ehlerová & Palouš 2005; McClure-Griffiths 2012; Ehlerová & Palouš 2013). It has generally been thought that such energetic shock can be generated from sources such as SNe, stellar winds, or collision of HVCs. A parcel of interstellar gas swept-up by fast shock is initially ionized by the shock, but later, cools down and becomes neutral. The cooled-down expanding shells with enough column densities are observable in H I emission line at 21 cm. Koo & Kang (2004), for example, estimated that there would be $\sim$3,000 H I shells produced by Type Ia SN explosions in the Galaxy. Type Ia SNe have population II progenitors and produce isolated expanding shells of radius $\leq$100 pc. In contrast, core-collapse SNe with massive progenitors are correlated both in space and time because they form in clusters so that they can produce gigantic H I shells with a radius more than a few hundred parsecs, i.e., 'supershells' (Heiles 1979).[1] If the energy is large

[1] We will use a *shell* as a broad term embracing both of a *small* shell and a supershell as far as its specific size is not mentioned.

enough, they can even break through the galactic gaseous disk to produce galactic "chimneys" that could be pathways for hot gas and heavy elements to disperse to the halo (Heiles 1984; Norman & Ikeuchi 1989). SN explosions, stellar winds, or their combination is the acceptable energy sources for many shells, but it seems to be inadequate in some cases. For example, quite a few supershells require much larger injection energy than the one by such stellar origin, and the population of shells is usually unacceptable by the level of star formation in their host galaxies (Rhode et al. 1999). As the most popular alternative scenario, HVC collisions on the Galactic disk has been suggested observationally (Mirabel & Morras 1990; Park et al. 2016) as well as theoretically (Tenorio-Tagle 1980; Tenorio-Tagle et al. 1987).

H I shells are observed as coherent features like a ring or arc-like shape for at least several km s^{-1} in H I 21-cm emission lines, and some of them vary in size over velocity. The observations of such expanding H I shells, however, is difficult because of the confusion with the Galactic foreground and background H I emission. For the individual SNR shells mentioned above, for example, only 9% of the 3,000 shells are expected to be observable (Koo & Kang 2004). There are two occasions when the detections can be made relatively easily. First, if the shell has a large angular size, e.g., more than a few degrees, the distinction with the other H I structures becomes allowable. This notion applies to supershells. Second, if the expansion velocity of the shell is very large, greater than the maximum velocity permitted by the Galactic rotation to that direction, then it could be easily discernible from the background emission. This notion applies to the shells with large ($\gtrsim$ 50 km s^{-1}) expansion velocity, e.g., the H I shells associated with radio SNRs (Park et al. 2013).

The pioneering study of H I shells/supershells had been done by Heiles (Heiles 1976, 1979, 1984). He carried out systematic studies to identify H I shells and supershells using the all-sky H I images available at that time. He identified 63 shells within $\pm 10^{\circ}$ of the Galactic plane. After this pioneering study, many observational

studies have been done. McClure-Griffiths et al. (2002) found 19 new H I shells in the SGPS (FWHM = 16′). Ehlerová & Palouš (2005) developed an automatic method to find an H I shell using Leiden-Dwingeloo H I survey data (LDS; FWHM = 30′; Hartmann & Burton 1997), and then Ehlerová & Palouš (2013) improved their method and covered the whole sky using LAB (FWHM = 36′; Kalberla et al. 2005) survey data. They identified 333 shells in the whole Galaxy. Daigle et al. (2007) schemed out a new automatic method especially for expanding small H I shells with radii < 40 pc using the CGPS (Taylor et al. 2003), and obtained a few thousand detections in the Perseus arm. The recent catalog of Suad et al. (2014) is done by mixing a visual inspection and an automatic searching algorithm and lists 566 supershell candidates in the second and third Galactic quadrants from the LAB data. Also, using the Search for Extraterrestrial H I survey data (SETH I; FWHM = 6′) obtained the Arecibo telescope before the release of the Galactic Arecibo L-Band Feed Array H I (GALFA-H I; Peek et al. 2011), Sallmen et al. (2015) identified 74 new H I shells over a wide range of Galactic latitudes.

So far survey studies of H I shells have been quite active, but there are only several detailed studies of individual shells. For example, Aquila supershell and Ophiuchus superbubble were investigated by using the Green Bank Telescope (FWHM = 9′) (Maciejewski et al. 1996; Pidopryhora et al. 2007), and Galactic chimney GSH 277+00+36 by using the combined data (with a final resolution of 3′) of the Australia Telescope Compact Array and the Parkes Radio Telescope (McClure-Griffiths et al. 2003). Recently, the I-GALFA survey had been observed H I gas in the first Galactic quadrant using the ALFA receiver on the Arecibo telescope. The I-GALFA survey provides the high-resolution (4′) and high sensitive (0.2 K) data, and therefore allows us to exploit the true nature of the sources detected in previous low-resolution studies and also to detect faint shells that were not detectable before. Also, the high-resolution view of individual H I shells will be helpful to understand

the nature of H I shells. In this chapter, we report the results of the systematic study of H I shells using H I data of the I-GALFA survey. Using the high-quality survey data, we re-examine the objects presented in low-resolution ($36'$) data by Heiles (1979) as well as provide a list of new shell candidates in the survey data.

Furthermore, since the I-GALFA data enable us to look into individual shell structures, we perform a pilot study of investigation on molecular clouds associated with shells using the obtained shell list. The site of H I shells could be where pre-existing molecular clouds are destroyed by the strong shock. However, the swept-up matter by the shock is accumulated and compressed in expanding shells, and cool, dense conditions can trigger molecular cloud formation (e.g., McCray & Kafatos 1987; Hartmann et al. 2001; Ntormousi et al. 2011; Dawson 2013). Recent statistical study of H I shells-molecular clouds have presented an observational evidence supporting the importance of the latter issue: Ehlerová & Palouš (2016) has investigated CO clumps in the outer Galactic shells, located in the second and third quadrants among the list of Ehlerová & Palouš (2013), and found about 20% increase of total CO amount by the shells. So, we would expect to provide addressable samples among our shell list in this case.

In Sections 3.3 and 3.4, we inspect the shell structures in the catalog of Heiles (1979) and new shell candidates, and several interesting individual shells are presented in detail. In Section 3.6, we derive physical parameters of the I-GALFA H I shells. In Section 3.7, we describe comparison results with other H I shell catalogs published before. In Section 3.8, we discuss the Galactocentric radius distribution of H I shells and molecular clouds in shell walls. We summarize this work in Section 3.9.

3.3 Heiles' Shells/Supershells

3.3.1 A Summary on Heiles' Shells/Supershells in the I-GALFA Survey

Heiles (1979) found 63 shells/supershells near the Galactic plane using the H I survey data of Weaver & Williams (1973) which had an angular resolution of $36'$. Among them, 20 objects are covered by the I-GALFA survey including those partly covered near its boundary. Columns 1–5 of Table 3.1 list the parameters of Heiles' shells, i.e. a name, a size, and a velocity range where a shell is visible given by Table 1 and 2 of Heiles (1979). Originally, the name of a shell consists of three values, that is a combination of central positions in Galactic coordinates and a reference LSR velocity. We have added "e" at the end of the names for shells classified as an expanding case by Heiles (1979). As Heiles' definition, the reference velocity is selected as where a shell is largest for an expanding case or a middle value of velocities where a shell is visible for a stationary case.

To confirm the shells in Table 3.1 in the I-GALFA survey data, we put the ellipses corresponding to their central positions and sizes on channel maps, and check whether a (partial) shell-like structure is visible. We start from the velocity ranges in Table 3.1 and continue to next velocities. For most objects, we could identify the corresponding shell structures. But some objects are either ambiguous or even absent. We attribute the miss-identification to the low-resolution data that Heiles (1979) used. We assign "rank" to each shell based on reliability which is different from one of Heiles (1979): rank "1" indicates a comparatively well-identified shell including both stationary and expanding cases, rank "2" is for an ambiguous shell which shows a hole and has a relatively bright boundary but looks like transient filaments, and rank "3" source is the one invisible in the I-GALFA survey data. Ranks of Heiles' shells are given in the last column of Table 3.1. For the shells graded rank

1, the newly determined parameters are listed in columns 6–11 of Table 3.1 including a name given by reidentified parameters of Galactic central position and reference velocity, a size in Galactic coordinates, and velocity range where a shell is visible in the I-GALFA survey data.[2] In an expanding case, we put "e" on the end of rank for shells that, in our opinion, seem to be expanding. Among twenty objects, thirteen and six are classified as rank 1 and 2, respectively. Two shells, GS042.0+00.4+29 (GS041+01+27) and GS076.0−00.9+29 (GS075−01+39), were confirmed to expand as mentioned in Heiles (1979). However, it does not seem to be clear if the other three shells, GS057.7+02.6−14 (GS057+03−11), GS061.6−00.4+54 (GS061+00+51), and GS064.3−00.9−80 (GS064−01−97), are expanding. A re-identified geometric diameter and velocity extent range 3.°4–12.°2 and 7–35 km s^{-1} having an average of 7.°1 and 20 km s^{-1}, respectively. Some shells show a relatively large extent (> 30 km s^{-1}) in velocity. They have one thing in common that their locations in velocity are near or beyond the maximum LSR velocities allowed by the Galactic rotation model in lines of sight (See Figure 3.1).

Individual shells are briefly described in Appendix A, and, in the next section, rather a detailed discussion has been made for four supershells; GS034.7−05.5+61 (GS034−06+65), GS035.1+05.9+57 (GS036+06+55), GS042.0+00.4+29 (GS041+01+27), and GS074.8−00.9+29 (GS075−01+39). The high-resolution data show that two supershells, GS034.7−05.5+61 (GS034−06+65) and GS042.0+00.4+29 (GS041+01+27), are complicated with other chimney or more than one shell. H I channel maps to present rank 1 shells in (ℓ, b) space are provided in Appendix A, and their (ℓ, b) and (ℓ, v) distributions are shown in Figure 3.1.

[2] In text, a shell graded rank 1 is written as the new name followed by the old one called by Heiles (1979) in parentheses.

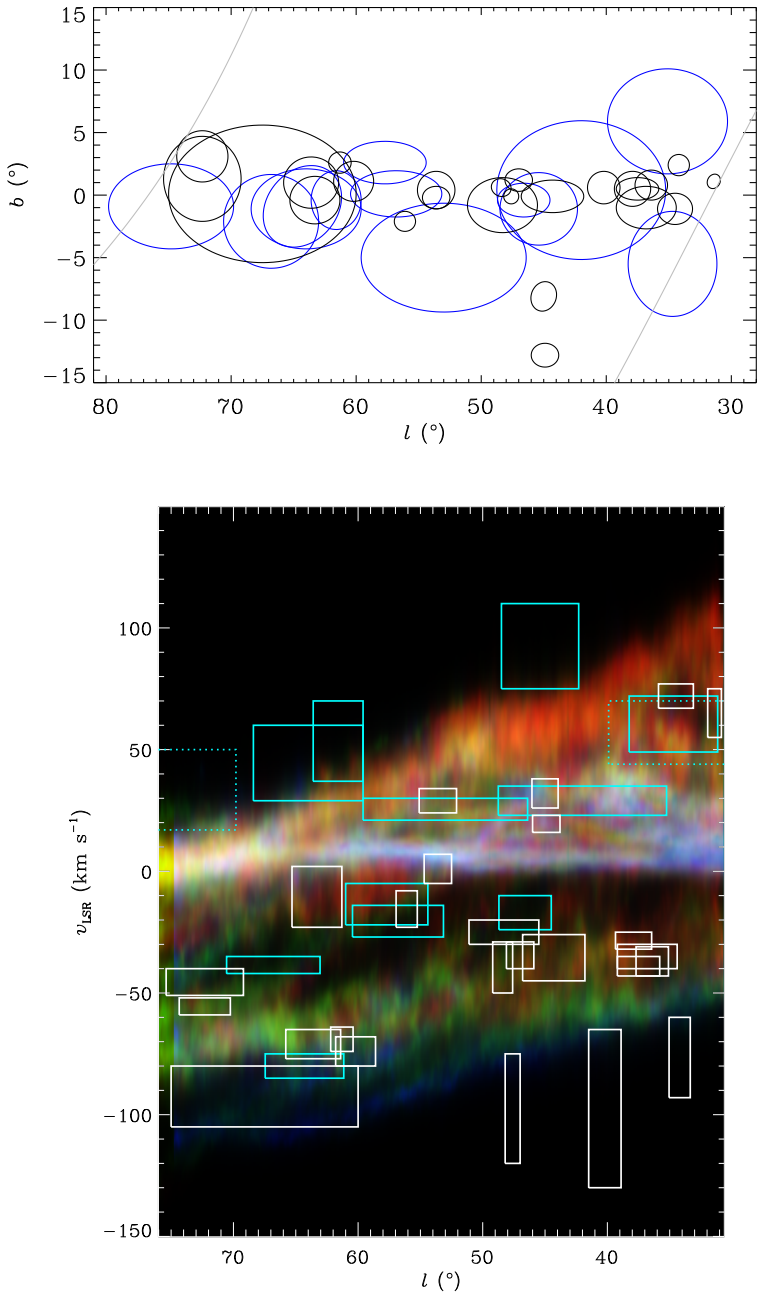

Figure 3.1. (ℓ, b) and (ℓ, v) distributions of H I shells in Tables 3.1 and 3.2. (Continued on the following page.)

Figure 3.1. (Previous page.) Top: Identified H I shells are marked with ellipses, blue for confirmed Heiles' shells and black for our new shell candidates. Gray oblique lines indicate I-GALFA survey boundaries, Dec. = $-1\overset{\circ}{.}27$ and $37\overset{\circ}{.}93$. Bottom: Three-color composite image is a combination of (ℓ, v) diagrams averaged over three latitude ranges, (-1°, $+1^\circ$), ($+1^\circ$, $+3^\circ$), and ($+3^\circ$, $+5^\circ$). Cyan and white boxes mark locations of confirmed Heiles' shells and our new shell candidates, respectively. Those with dotted lines present shells partially covered by the I-GALFA survey.

3.3.2 Individual Shells/Supershells

GS034.7−05.5+61 (GS034−06+65)

This supershell was first identified by Heiles (1979) and has been studied in detail by Maciejewski et al. (1996). Heiles (1979) cataloged it as a stationary shell with a size of $5^\circ \times 8^\circ$ visible between +49 and +81 km s^{-1}. On the other hand, Maciejewski et al. (1996), using a fully-sampled map with an angular resolution of $21'$ obtained by using the former 140-ft Green Bank telescope, noted that there is a "cone" structure near the midplane that appears to connect to the shell (see next). The cone structure has an apex at ($34\overset{\circ}{.}6$, $-1\overset{\circ}{.}4$), and its opening angle varies from 30 to 80 degrees with velocity. Maciejewski et al. (1996) considered the cone and the shell structures as parts of a single structure persisting over +38–+72 km s^{-1}, and adopted +55 km s^{-1} as its systemic velocity where the brightness of the cone structure attains its maximum. Its kinematic distance was 3.3 kpc, which gave the full extent of 320 pc × 550 pc ($5\overset{\circ}{.}6 \times 9\overset{\circ}{.}5$). They proposed that this, so called, Aquila supershell could have been produced by 10–100 SNe during last 10^7 yrs. However, we think that the two structures are unconnected, and the shell structure seems to be stationary as described below. If adopting +61 km s^{-1} as its systemic velocity, it is located at a bit further distance (d = 4.0 kpc), and geometric mean radius of

Table 3.1

Heiles' H I Shells/Supershells in the I-GALFA Survey Area

Heiles (1979)					This Paper					
Name	$\Delta\ell$ (°)	Δb (°)	v_{min} (km s^{-1})	v_{max} (km s^{-1})	Name	$\Delta\ell$ (°)	Δb (°)	v_{min} (km s^{-1})	v_{max} (km s^{-1})	Rank[a]
GS033+06−49	4	3	−59	−39		...				2
GS034−06+65	5	8	+49	+81	GS034.7−05.5+61	7.1	8.4	+49	+72	1
GS034+02+73	3	3	+65	+81		...				2
GS036+01−21	1	6	−31	−11		...				3
GS036+06+55	9	8	+45	+65	GS035.1+05.9+57	9.6	8.4	+44	+70	1
GS041+01+27e	14	12	+25	+37	GS042.0+00.4+29	13.5	11.1	+23	+35	1e
GS046−01−15	3	4	−23	−7	GS046.6−00.4−17	4.2	2.7	−24	−10	1
GS046−01+83	7	6	+77	+89	GS045.4−01.1+93	6.2	5.8	+75	+110	1
GS048−04+49	3	4	+45	+53		...				2
GS052−05+25	11	7	+21	+29	GS053.0−05.0+26	13.2	8.7	+21	+30	1
GS052+07+39	5	7	+17	+61		...				2
GS057+03−11	6	3	−15	−7	GS057.7+02.6−14	6.6	3.4	−22	−5	1
GS057+01−33e	8	3	−35	−15	GS056.8+00.1−21	7.3	3.7	−27	−14	1
GS061+00+51e	3	4	+37	+53	GS061.6−00.4+54	4.0	4.7	+37	+70	1
GS063+04+13	4	4	+9	+17		...				2
GS063−01−3	2	2	−7	+1		...				2
GS064−01−97e	11	6	−99	−75	GS064.3−00.9−80	6.3[b]	6.6[b]	−85	−75	1
GS066−01+35	6	6	+29	+41	GS064.0−01.1+45	8.8	6.4	+29	+60	1
GS067−02−37	7	8	−39	−35	GS066.8−02.1−39	7.5	7.6	−42	−35	1
GS075−01+39e	11	6	+17	+41	GS074.8−00.9+29	10.0	6.8	+17	+50	1e

Note. A name stands for a central position in Galactic coordinates and representative velocity (See § III*b*(iii) of Heiles (1979) for details about the velocity). For those of Heiles (1979) considered as expanding by the authors, we added "e" at the end of their names.

[a]Reinspection with the I-GALFA data: well-identified (1), ambiguous (2), and invisible (3) shells/supershells. "e" next to the number indicates that a shell/supershell is expanding.

[b]These values are the ranges of this shell occupied in Galactic longitudes and latitudes, but this shell can be well-described as a tilted ellipse (See the panel of GS064.3−00.9−80 in Figure A.1). It has a major axis ($a_{\rm maj}$) of 7.°1 and a minor axis ($a_{\rm min}$) of 5.°6 with an angle (θ) of about 50° from ℓ-axis in the counter-clockwise direction.

3.°9 corresponds to 270 pc.[3]

Figure 3.2 shows H I velocity-channel maps of the area surrounding GS034.7−05.5+61 (GS034−06+65), which present H I brightness temperature multiplied by $sin|b|$ to show weak emission at high latitudes. (We note that, as a result, H I emission near $b = 0°$ artificially becomes zero). The southwestern area which is not covered by the I-GALFA is filled with the LAB survey data. Both the shell and the cone structures described above are apparent in Figure 3.2. We make notes on new features seen in the I-GALFA maps: (1) GS034.7−05.5+61 (GS034−06+65) of Heiles (1979) is seen clearly at +49–+72 km s^{-1}. The overall shape is close to a water drop rather than to an ellipse. The geometrical center and the size, obtained by fitting an ellipse to the outer boundary, are (34.°7, −5.°5) and 7.°1 × 8.°4, respectively. The thickness of the shell is ∼1°, and the brightness sharply decreases across the inner boundary. At LSR velocities lower than +50 km s^{-1}, the outer boundary of the shell becomes unrecognizable although the inner hole can be seen. (2) The cone structure is seen from +64 to +49 km s^{-1}. The opening angle increases systematically from 30 to 100 degrees as the velocities decrease from +64 to +49 km s^{-1}. It might indicate that the cone structure is expanding outside at ∼15 km s^{-1}. The shell (and the hole), however, does not change either its shape or size with velocity. At $v_{\rm LSR} = +53$ km s^{-1}, for example, the eastern wall of the cone structure is more than a degree outside of the outer border of the shell. This casts some doubt about the association between the cone and the shell. (3) The cone structure extends above the midplane. (Maciejewski et al. (1996) did not map the area above $b = -1°$.) At +49–+53 km s^{-1}, the local area just above the cone has enhanced brightness up to $b \sim 2°$. Figure 3.3 is 1-D intensity profiles cut along longitudes at three different latitudes, which are marked in the third

[3] We note that we accepted Galactic rotation curve of Brand & Blitz (1993) with $\Theta_\odot = 220$ km s^{-1} and $R_\odot = 8.5$ kpc, which is different from Heiles (1979).

panel of Figure 3.2. The wall component at high longitudes ($\ell \gtrsim 35^\circ$) is drawn from the I-GALFA data and shows that the inner boundary of the cone structure is quite sharp. The H I distribution at lower negative latitudes shows many clumps, filaments, and "spokes." The spokes, which are thin, straight filaments, appear to originate from the apex of the cone in the midplane, which is fascinating. We note that all these complicated H I structures above the midplane are associated with GS035.1+05.9+57 (GS036+06+55) which is another supershell in the catalog of Heiles (1979). In the next section, we propose that GS035.1+05.9+57 (GS036+06+55) is indeed a chimney and that the cone is part of the chimney. The association of GS034.7−05.5+61 (GS034−06+65) with the chimney is uncertain. It is centered at somewhat higher velocity and spatially offset from the cone, which suggests that it could be an unrelated object.

GS035.1+05.9+57 (GS036+06+55)

This H I supershell was cataloged by Heiles (1979) as a stationary shell with an extent of $9^\circ \times 8(?)^\circ$ visible between +45 and +65 km s^{-1}. But as we discuss below this is probably a chimney, that is the blowout of a supershell. Figure 3.4 is H I velocity-channel maps which present $T_b sin|b|$ same as the case of Figure 3.2 mentioned in the second paragraph of Section 3.3.2. In the I-GALFA data, the shell appears within an imaginary ellipse with a center of ($35\overset{\circ}{.}1$, $5\overset{\circ}{.}9$) and a size of $9\overset{\circ}{.}6 \times 8\overset{\circ}{.}4$. It is visible from +44 to +70 km s^{-1}. However, at +57 km s^{-1}, it is immediately obvious that GS035.1+05.9+57 (GS036+06+55) is not a complete shell although one may imagine a shell structure at low angular resolution. Its top portion is open, and there are faint H I fragments up to +20 degrees. If we adopt 3.8 kpc, this corresponds to about 1.3 kpc above the plane. The area is quite complicated with many vertical filaments which look like emanating from the midplane to the north of the galactic plane. Such gaseous pillars or spokes appear to converge on the midplane at $\ell \sim 35\overset{\circ}{.}5$.

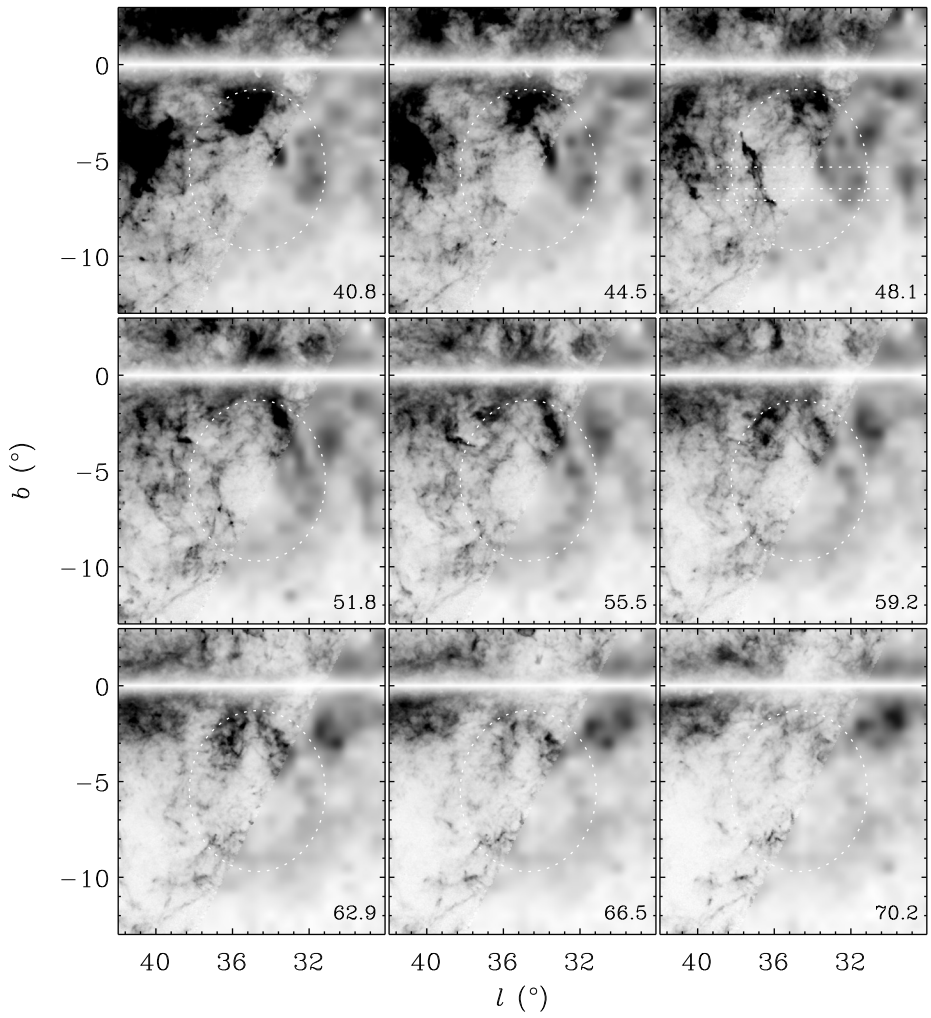

Figure 3.2. H I velocity-channel maps of GS034.7−05.5+61 (GS034−06+65). The central velocity of each channel is written in the lower right corner in km s^{-1}, and a channel width is 0.92 km s^{-1}. Brightness temperature is multiplied by $sin|b|$ to make weak features in high latitudes noticeable, and presented in an inverted gray scale which ranges from 0 K (white) to 1.9 K (black). The white dotted ellipse is drawn to help locating the supershell. In the channel map of $v_{\rm LSR} = 48.1$ km s^{-1}, three white dotted lines are drawn for intensity profiles of Figure 3.2. A partial field on the right side of each panel has not been covered by the I-GALFA survey and filled with the LAB survey data.

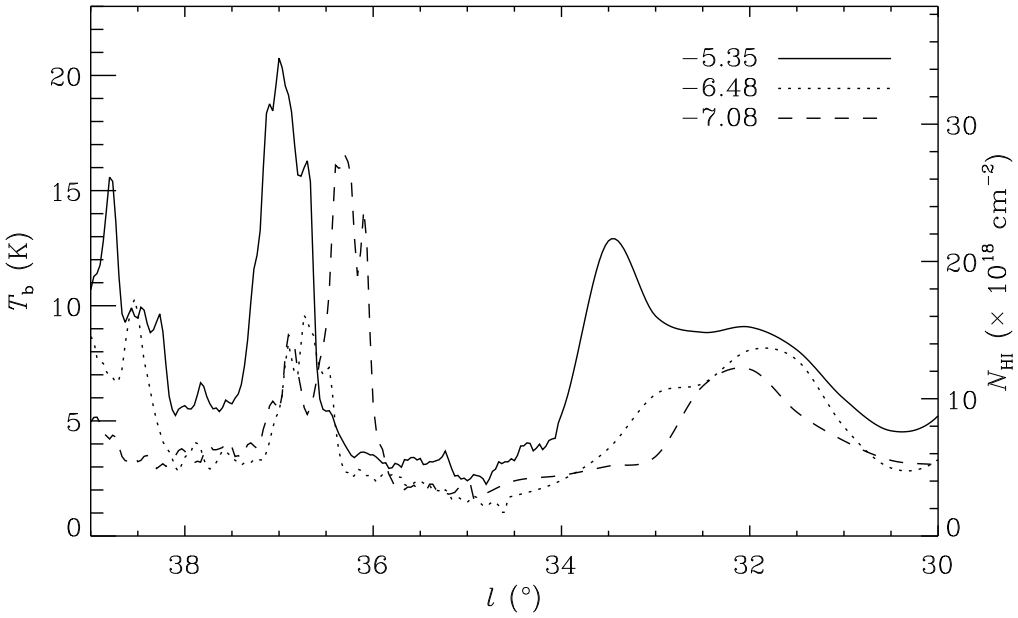

Figure 3.3. H I intensity profiles from a one-dimensional cut across the supershell, GS034.7−05.5+61 (GS034−06+65). Each profile is obtained along longitudes at $b = -5.^{\circ}35$, $-6.^{\circ}48$, and $-7.^{\circ}08$ at $v = 48.1$ km s^{-1} (see the third panel of Figure 3.2). With respect to $\ell \sim 34^{\circ}$, the left part corresponds to the I-GALFA data and the right to the LAB one.

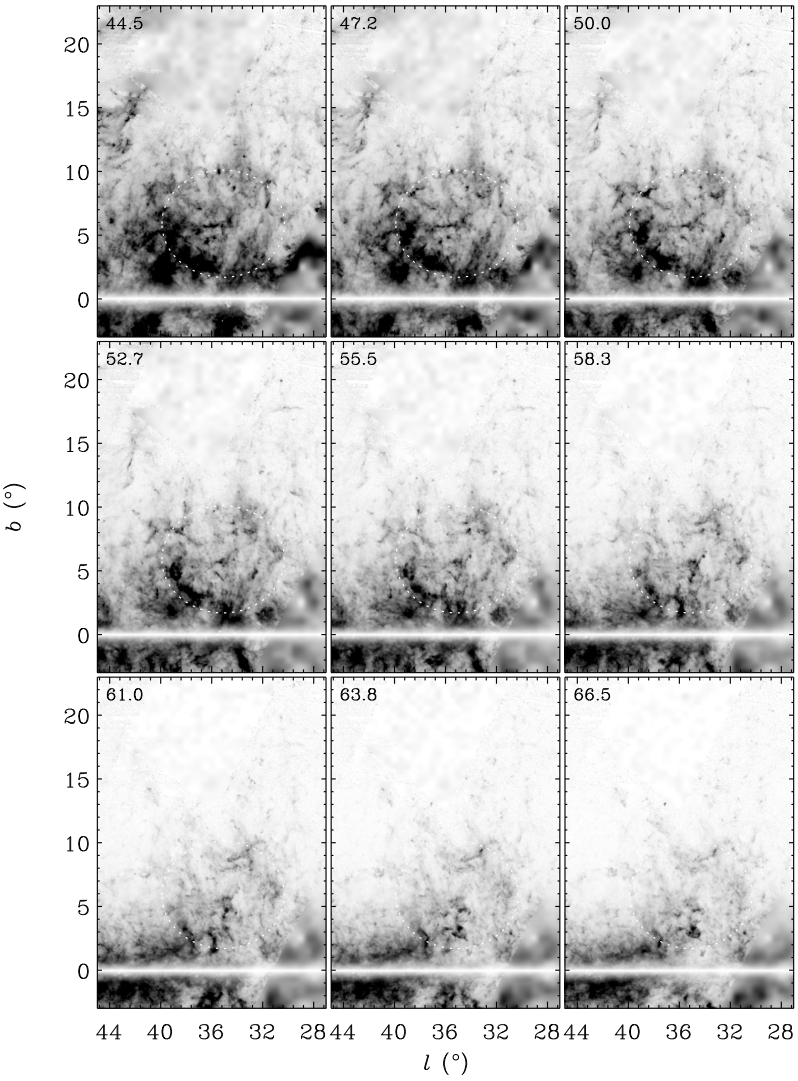

Figure 3.4. H I velocity-channel maps of GS035.1+05.9+57 (GS036+06+55). The central velocity of each channel is written in the upper right corner in km s^{-1}, and a channel width is 0.92 km s^{-1}. An inverted gray scale presents $T_{\rm b} sin|b|$ and ranges from 0 K (white) to 1.7 K (black). A white dotted ellipse on each panel is drawn to help locating the supershell. Some partial fields, which is some upper regions and an area in the lower right corner, are filled with the LAB data (Kalberla et al. 2005).

There are several H II regions at velocities from +44 to +60 km s^{-1} which are determined at near distances, and they are surrounded the converging position. In the LAB survey, there is H I gas at +30 degrees at the same velocity range. Interestingly, at the converging position, we discovered an H I gas structure which can be called as 'Forbidden-Velocity Wing' (FVW; Kang & Koo 2007). It has a 0.°7-diameter at (ℓ, b) = (35.°3, −0.°2), and is seen from +120 to +179 km s^{-1}. There is no stellar counterpart and even radio emission feature, so it is not clear what drives such fast-moving gas. It would be worth to investigate whether the H I structures, chimneys, pillars, and FVWs, and stellar sources like H II regions are linked to each other, but we defer a further study for later work.

GS042.0+00.4+29 (GS041+01+27)

This is a remarkable supershell but has not been studied much since discovered by Heiles (1979). He identified that the shell has an angular size of 14° × 12° and its expansion is visible between +25 and +37 km s^{-1}. The velocities indicate that it is within the inner Galaxy (the part of the Galaxy inside the Sun's orbit). It is hard, however, to know where it is actually located between *near* and *far* away from the Sun along the line of sight. Assuming that it is at near-distance, he estimated its distance from the Sun of 2 kpc and geometric mean radius of 250 pc from the flat Galactic rotation curve with $\Theta_\odot$ = 250 km s^{-1}and $R_\odot$ = 10 kpc. Corresponding initial explosion energy is $\sim 8 \times 10^{52}$ erg which demands lots of multiple SN explosions.

Figure 3.5 shows H I velocity-channel maps GS042.0+00.4+29 (GS041+01+27), which are drawn every three channels. Panels in the right column are same as those in the middle column, but $T_\mathrm{b} sin|b|$ same as the case of Figure 3.2 mentioned in the second paragraph of Section 3.3.2. Overall, in the high-resolution data, it shows a

complete elliptical shape in +23–+35 km s^{-1}, with a center almost on the midplane. But, details are quite complicated with many large and small H I features which can be related or unrelated to the supershell. At +27 km s^{-1}, for example, the outer boundary is well-defined relatively, but the inside is partially filled with extensive emission features, and some of them extend outside of the supershell. The cross section of the supershell is distinct in the vicinity of $b = 5°$ (periphery of a white line in the third panel), and its width is $\sim 0.^{\circ}4$. By comparison, the western edge in negative latitudes is blended into turbulent stream-like features starting from the plane. As velocity goes high, the outer boundary becomes faint and different structures appear. Among them, at least two structures are shell-like and located in the periphery of the supershell (black dotted ellipses in the bottom panels). These are visible from +31 to +45 km s^{-1}. While one has a size of $\sim 11° \times 10°$ at the center of (ℓ, b) = ($38.^{\circ}5$, $0.^{\circ}5$), another has a size of $\sim 15° \times 14°$ at the center of (ℓ, b) = ($38.^{\circ}9$, $2.^{\circ}4$). (Hereafter, GS038.5+0.5+38 and GS038.9+02.4+38. These are not listed in Table 3.2.) Also, a stick-like structure, which resembles an exclamation mark without a dot (indicated by an arrow in the bottom panels), is visible from +29 to +38 km s^{-1}, and located inside the supershell GS042.0+00.4+29 (GS041+01+27), but extends to outside of the supershell.

Figure 3.6(a) shows intensity profiles along a specific line above the wall of the supershell at $v_{\rm LSR}$ = +23.3, +25.1, +27.0, and +28.8 km s^{-1}. The line is in the radial direction on the center of the supershell, and the line and center are marked with a white line and cross in the third panel of Figure 3.5, respectively. The area surrounding the line is less contaminated than the other part of this shell wall. A ridge near the middle of each profile is intensity distribution of the supershell at each velocity, and its inner boundary is clearly shifted from left to right (i.e. outward) as velocity increases. This result suggests that this supershell is expanding.

Let consider an expanding spherical shell simply. Since its small portion will

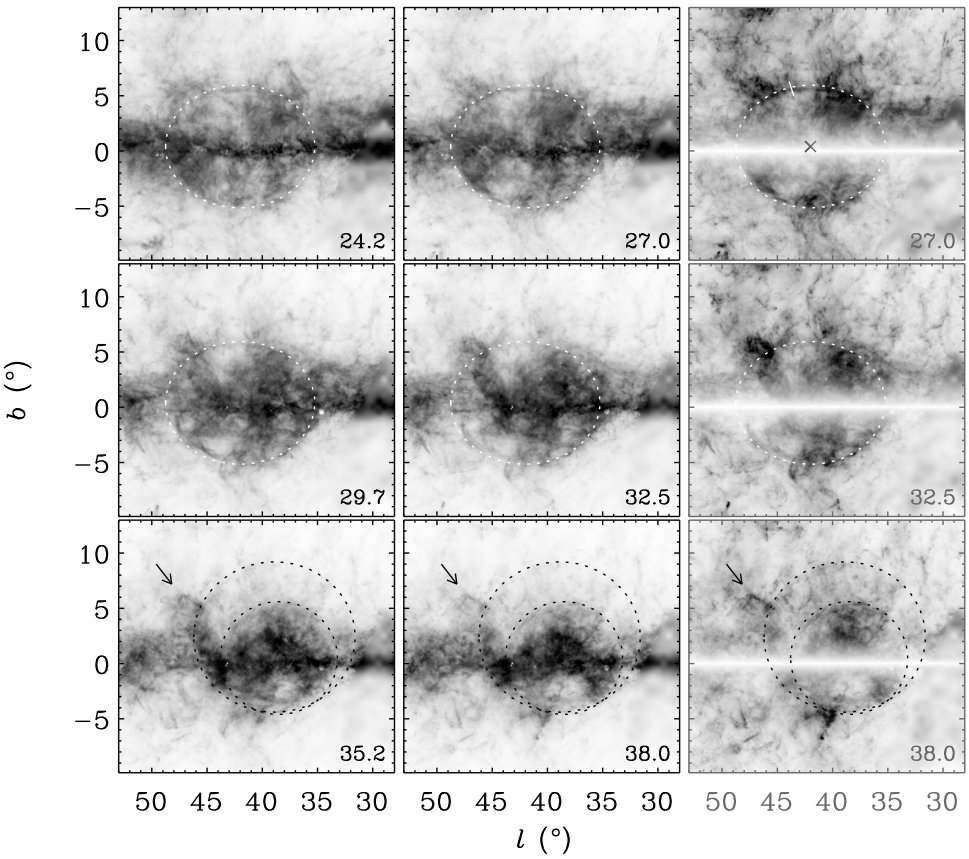

Figure 3.5. H I velocity-channel maps of GS042.0+00.4+29 (GS041+01+27). In the first two columns, brightness temperature is presented in an inverted gray scale which ranges from 0 K (white) to 100 K (black). Channels in the last column are same as those in the second column, but $T_{\rm b}sin|b|$. Its inverted gray scale ranges from 0 K (white) to 5 K (black). The central velocity of each channel is written in the lower right corner in km s^{-1}, and its channel width is 0.92 km s^{-1}. In the top and middle panels, a white ellipse is drawn to help locating the supershell. In the third panel, its center is marked with a cross in the third panel, and a white line on the upper shell wall is for Figure 3.6(a). In the bottom panels, the other two black ellipses and an arrow are drawn for H I structures mentioned in Section 3.3.2. A partial field in the lower right corner is filled with the LAB data (Kalberla et al. 2005).

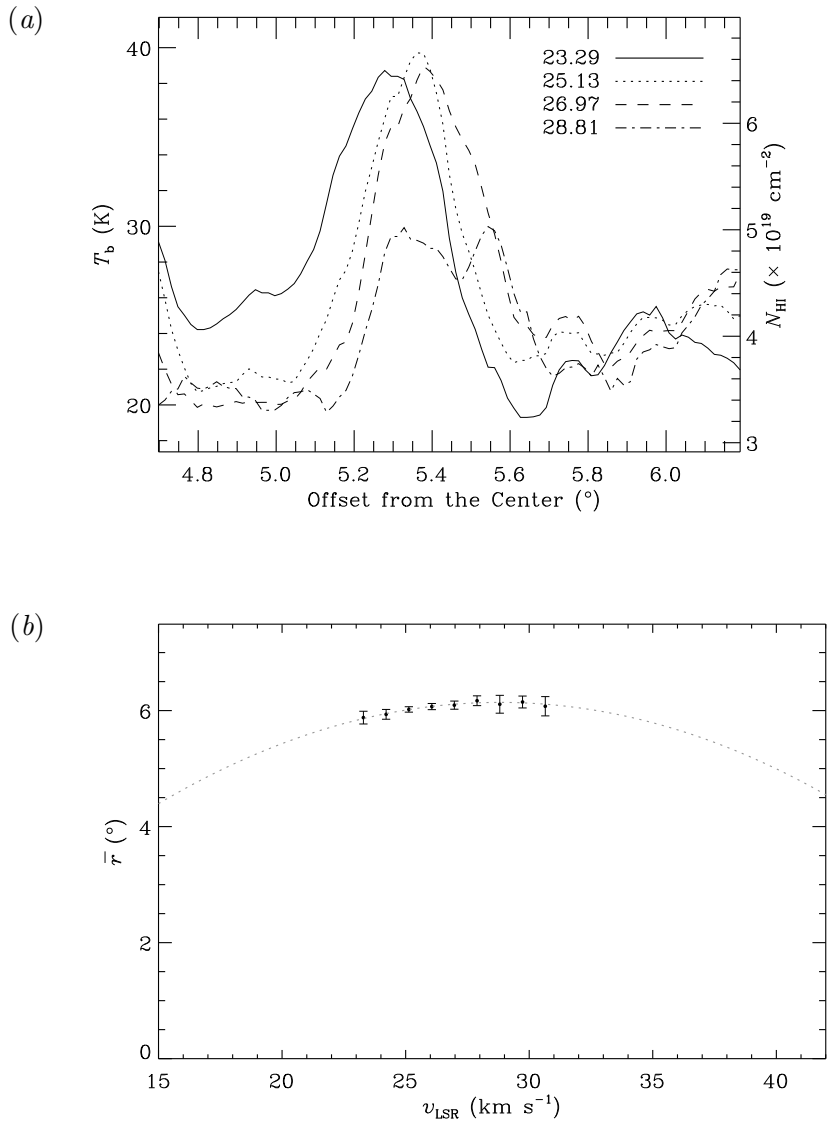

Figure 3.6. Expansion of GS042.0+00.4+29 (GS041+01+27). (*a*) Intensity profiles are obtained across the wall of the supershell from four velocity channels in a radial direction from the center ($\ell = 40\overset{\circ}{.}0$, $b = 0\overset{\circ}{.}4$). The location of the center and where the profiles are obtained are marked with a cross symbol and a white line in the third panel of Figure 3.5, respectively. (*b*) Variation of the geometric mean radius in LSR velocity. Dots are from observational data with the 1σ uncertainty, and a dotted curve from the best-fitting of an expanding spherical shell model.

approximate a paraboloid, a projected radius on the sky, which we observe, can be written as

$$\theta_{\rm proj} = \theta_{\rm sh}(1 - 0.5(v_{\rm obs} - v_0)^2/v_{\rm exp}^2), \tag{3.1}$$

where $\theta_{\rm sh}$ is a radius of the shell, v_0 systemic velocity, and $v_{\rm exp}$ an expansion velocity. By the best-fitting with observational values of $\theta_{\rm proj}$ (i.e mean radius) and $v_{\rm obs}$, other three parameters are obtained: $\theta_{\rm sh} = 6\overset{\circ}{.}1 \pm 0\overset{\circ}{.}1$, $v_0 = 28.8 \pm 1.7$ km s^{-1}, and $v_{\rm exp} = 18.3 \pm 6.8$ km s^{-1}. Since data points used, which are near a tangent position as shown in Figure 3.6(a), are too small to describe the whole system, values may be more uncertain. Figure 3.6(b) presents data used and the best-fit model with dots and a dotted curve, respectively. If one accepts v_0 estimated above, this shell is located at 2.0 kpc from the Sun and has a radius ($R_{\rm sh}$) of $\sim$ 213 pc. A dynamic age, $t_{\rm d} \simeq 0.29 R_{\rm sh}/v_{\rm exp}$, is $\sim$ 3.4 Myr. It is not easy to extract emission only from this shell since it extends over large space and so huge foreground and background emissions are overlapped. From a part of a wall around where is used for Figure 3.6(a), we infer several physical parameters such as mass and energy. A sample box has a size of $2\overset{\circ}{.}1 \times 0\overset{\circ}{.}6$ and the velocity range from +23 to +35 km s^{-1}. Background emission, which is estimated from same size boxes above and below the sample, is subtracted. The sample contains H I mass of $\sim 1.8 \times 10^3 M_\odot$. Assuming that the shell has isotropic and Gaussian mass distribution and the sample is representative for this shell, the total mass ($M_{\rm sh}$) and kinetic energy of the shell are extrapolated as $\sim 1.4 \times 10^5$ $M_\odot$ and $\sim$ 4.5×10^{50} erg including the He abundance, respectively. Initial explosion energy ($E_{\rm E}$) can be estimated from an equation of Cioffi et al. (1988),

$$E_{\rm E} = 6.8 \times 10^{43} {n_0}^{1.16} R_{\rm sh}^{3.16} {v_{\rm exp}}^{1.35} \xi_{\rm m}^{0.161} \text{ erg}, \tag{3.2}$$

where n_0 is the ambient density of hydrogen nuclei in cm^{-3}, $R_{\rm sh}$ in pc, $v_{\rm exp}$ in km s^{-1}, and $\xi_{\rm m}$ the metallicity. If total mass above is uniformly distributed within the volume of the shell at first, n_0 is $\sim$ 0.13 cm^{-3}. If we accept $\xi_{\rm m} = 1$, then $E_{\rm E} \sim 7.4 \times 10^{51}$ erg.

We note that values such as $M_{\rm sh}$, n_0, and $E_{\rm E}$ could be underestimated. First, the sample box, which is above $\sim$ 200 pc from the midplane, may be inappropriate to represent the whole system because real density distribution will not be uniform (e.g. vertical density gradient). Derived n_0 seems quite small comparing an expected value of an average midplane density at the Galactocentric radius of the supershell ($\sim$ 1.4 cm^{-3}; Kalberla & Kerp 2009). If assuming $n_0 = 1\,{\rm cm}^{-3}$, we obtain $E_{\rm E} \sim 5 \times 10^{52}$ erg, which suggests that $\sim$ 50 SNe are required (See Section 3.6).

We suggest that three supershells, GS042.0+00.4+29 (GS041+01+27), GS038.5+0.5+38, and GS038.9+02.4+38, might be originated in the same place. We sketched H I gas features probably related to shells in Figure 3.7. It shows that they surround a space with its center of $\ell \sim 38^\circ$. Also, massive stars listed by Reed (2003, 2005) are gathered in the space. Atomic gas structures and massive stars seem to be morphologically consistent. We suggest that an active star-forming region is located at $\ell \sim 38^\circ$, and generates three shells above.

GS074.8−00.9+29 (GS075−01+39)

This is seen near the border of the I-GALFA survey data and partially covered by the data. This was identified by Heiles (1979) as an expanding shell with an extent of $11^\circ \times 6^\circ$ visible between +17 and +41 km s^{-1}. We give slightly different definition after examining it in the I-GALFA data: a size of $10\overset{\circ}{.}0 \times 6\overset{\circ}{.}8$ and velocity range of (+17, +50) km s^{-1}. These shell walls show complicated filamentary structures. The eastern part seems to burst, and vertical features appear there, as seen in the LAB data. This shell is apparently positioned near the Cygnus X which is one of the richest known sites showing vigorous star-forming activities first discovered by Piddington & Minnett (1952). It is worth noticing that thermal emission structures at 6 cm decomposed by Xu et al. (2013, See their Figure 4) seem to correlate fairly well with H I structures of this shell. In the region of this shell, thermal emission

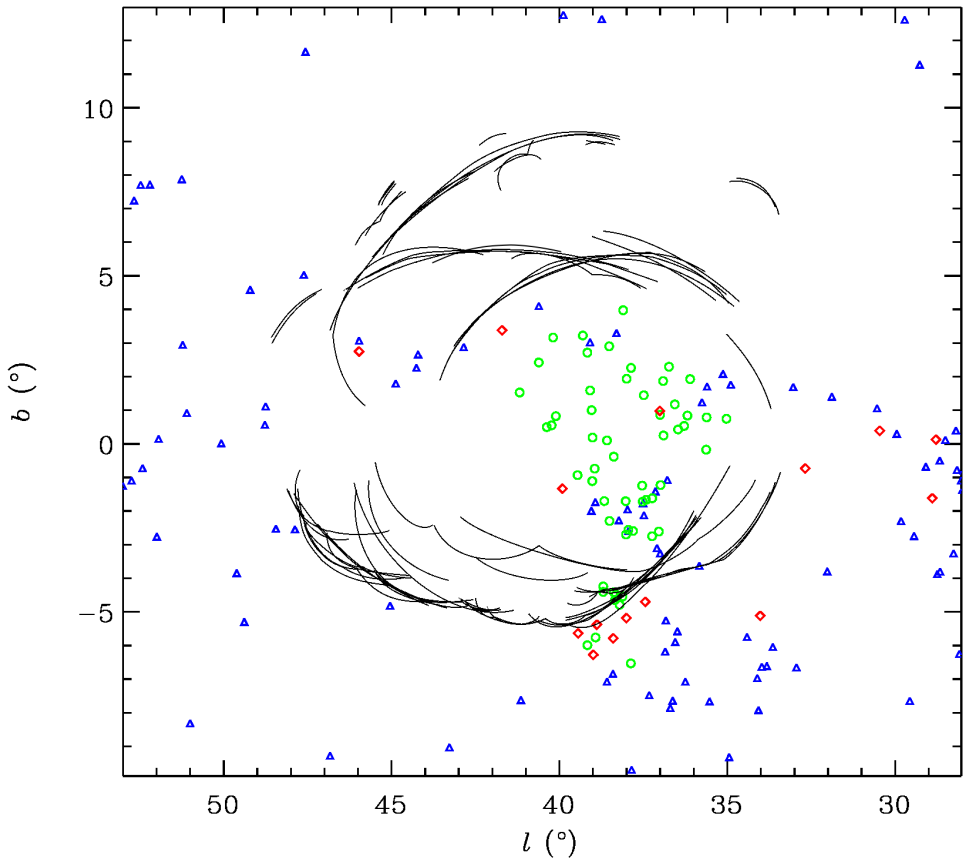

Figure 3.7. Sketch of GS042.0+00.4+29 (GS041+01+27). Traces are drawn every two channels ($\Delta v = 0.92$ km s^{-1}) from 23.3 to 39.8 km s^{-1}. Massive stars published by Reed (2003, 2005) are marked: red diamonds for O-type stars, blue triangles for B0-3 type stars, and green circles for uncertain stars whether it is O or B-type.

shows clear filamentary structures, and, surprisingly, they are located in where H I emission of the shell is not seen or faint. There is an H I shell-like structure, which is not listed, over the northeastern part of GS074.8−00.9+29 (GS075−01+39). It has a size of $3\overset{\circ}{.}6 \times 4\overset{\circ}{.}2$ at $(\ell,\ b) = (72\overset{\circ}{.}0,\ +1\overset{\circ}{.}1)$ with a 30°-angle with the north direction. The thermal filamentary features fill inside the H I structure and extend outward. Also, a shell-like feature in thermal emission is seen inside GS074.8−00.9+29 (GS075−01+39). The eastern inner boundary of the shell walls seems to fit well with the western border of the bright thermal features at $\ell \sim 79°$–$84°$. Xu et al. (2013) concluded that the major contributor is thermal diffuse emission rather than the discrete H II regions by comparison with H II regions of Paladini et al. (2003) in the Cygnus X. This morphological correlation may imply that multiple stellar activities make complicated H I structures of GS074.8−00.9+29 (GS075−01+39), and hot gas inside the shell is visible in radio continuum. Also, such energy may be generated by the previous stellar generation in the Cygnus X.

3.4 New Shell Candidates

3.4.1 A Summary on New Shell Candidates in the I-GALFA Survey

Using the I-GALFA H I data, we found relatively well-defined twenty-five shells, which maintain a complete or incomplete elliptical shape (expanding, in some case) for at least several velocities. Table 3.2 lists the shells. A name of a shell is in column 1, which is originated by the same way mentioned in Section 3.3. A size in Galactic coordinates are in columns 2–3, and a velocity range where a shell is visible in columns 4–5. In the case of an expanding shell, 'e' is written in the last column. The geometric mean diameters of the new shells, assuming an elliptical shape, range between $1\overset{\circ}{.}1$ and $12\overset{\circ}{.}8$ with an average of $4\overset{\circ}{.}6$. The lower boundary is caused by a selection bias that we focus on objects with sizes $\gtrsim 1°$ which is possible to be

a "supershell" although exactly it depends on their distances. The velocity extent ranges 7–65 km s^{-1} with an average of 17 km s^{-1}. Some shells show a relatively large extent (> 30 km s^{-1}) in velocity. They have a common point that they appear at relatively very negative LSR velocities comparing with apparently neighboring H I emission features (See Figure 3.1).

Individual shells are briefly described in Appendix A, and, in the next section, rather a detailed discussion has been made for three supershells; GS040.2+00.6−70, GS053.6+00.4+29, and GS067.5+00.1−93. H I channel maps to present all shells are provided in Appendix A, and their (ℓ, b) and (ℓ, v) distributions are shown in Figure 3.1.

3.4.2 Individual Shells/Supershells

GS040.2+00.6−70

This is one of the most interesting shells in the I-GALFA survey area and discussed in earlier research of Park et al. (2016). Its size is about 2.°6 corresponding to $\sim$900 pc at d = 20 kpc. So, it is very likely to be a supershell, and indeed we derived that initial energy as much amount of 70 SNe is required to form it. Its cartwheel-like shape is very intriguing, and it seems to be different from the general thought of what we can imagine appearances of an expanding shell projected on velocity-channel maps. Overall, its size appears to become smaller as absolute LSR velocity increases, but the interior structures are complicated with spoke-like filaments and clumps. It is worth noticing that a compact HVC (CHVC) is located in the very center of this supershell. We think that interaction with the CHVC will mainly cause such appearance. That is because it is quite far from the Galactic midplane in height and no association with known stellar components. Therefore, the CHVC in the center is most likely to be a contributor, and the interior gas features may be one or both of accelerated disk gas by interaction with the CHVC and cooled part of the CHVC,

Table 3.2

Newly Identified H I Shells/Supershells in the I-GALFA Survey Area

Name	$\Delta\ell$ (deg)	Δb (deg)	v_{min} (km s^{-1})	v_{max} (km s^{-1})	Exp?
GS031.4+01.1+65	1.1[a]	1.2[a]	+55	+75	e
GS034.2+02.4−77	1.7	1.7	−93	−60	···
GS034.5−01.1+72	2.8	2.5	+67	+77	···
GS036.4+00.8−37	2.6	2.4	−43	−31	···
GS036.8−01.0−35	4.8	3.4	−40	−30	···
GS037.5+00.5−39	3.4	1.8	−43	−35	···
GS037.9+00.5−25	2.9	2.8	−32	−25	···
GS040.2+00.6−70	2.6	2.6	−130	−65	e
GS044.3−00.1−39	5.0	2.6	−45	−26	···
GS044.9−12.8+20	2.2	1.9	+16	+23	···
GS045.0−08.1+32	2.1[a]	2.4[a]	+26	+38	···
GS047.0+01.2−35	2.2	1.8	−40	−29	···
GS047.6−00.1−98	1.2	1.2	−120	−75	···
GS048.3−00.8−25	5.6	4.4	−30	−20	···
GS048.4+00.6−40	1.6[a]	1.4[a]	−50	−29	···
GS053.6−00.2+5	2.2	1.8	−5	+7	e
GS053.6+00.4+29	3.0	3.0	+24	+34	···
GS056.1−02.1−21	1.7	1.6	−23	−8	e
GS060.2+01.1−74	3.2	3.2	−80	−68	···
GS061.3+02.6−69	1.8	1.7	−74	−64	···
GS063.3−00.4−3	4.0	3.8	−23	+2	e
GS063.6+01.0−71	4.4	4.1	−77	−65	···
GS067.5+00.1−93	15.0	11.0	−105	−80	···
GS072.3+01.3−46	6.2	6.8	−51	−40	···
GS072.3+03.1−56	4.1	4.1	−59	−52	···

Note. This table lists information as the same way of Table 3.1 except for the last column. In the case of an expanding shell, 'e' is written in the last column.

[a]These values are the ranges of each shell occupied in Galactic longitudes and latitudes, but it can be well described as a tilted ellipse which has ($a_{\rm maj}$, $a_{\rm min}$, θ) = (1.°2, 1.°0, 60°) for GS031.4+01.1+65, (2.°4, 2.°0, −20°) for GS045.0−08.1+32, and (1.°6, 1.°4, −20°) for GS048.4+00.6−35. For these shells, the tilted ellipses are used in Figure A.2 to help locating the shells.

not expanding. In other words, if we look at it carefully, the western rim where is less complicated than one in the east and shows a shift, i.e. likely to expand. This supershell would be a good example formed by CHVC collision with the Galactic disk gas.

GS053.6+00.4+29

This seems to be an almost complete, stationary shell. It has a size of 3° with a center of $(\ell, b) = (53.^{\circ}6, 0.^{\circ}4)$ and is visible from +24 to +34 km s^{-1}. The inner boundary of the shell seems to be well-defined, but the outer boundary on the east and west are ambiguous because of contamination by back/foreground emission. The northeastern and southern parts of the shell show a thin wall ($\sim 9'$). The inside of this shell seems to be not empty: Somewhat bright H I emission shows an elongated filament-like structure just below the center of the shell, which extends over $\gtrsim 1^{\circ}$ with a 10°-angle to the Galactic plane, and a circular structure of weaker emission is overlapped. Figure 3.8 is a three-color composite image at $v_{\rm LSR} = +32,\ +29,\ +25$ km s^{-1} and a dotted ellipse indicates a shell-defined size. The figure shows the features mentioned above. From the color composite image, one may think that the circular feature is almost not seen at the lowest velocity. But it is not likely to be caused by a lack of H I gas, instead of an absorption effect of cold foreground gas with respect to the warm background. Detection of ^{13}CO molecular gas emission by the GRS survey (Jackson et al. 2006) and sharp dips in H I line profiles supports the presence of dense molecular clouds there. As an example, H I position-velocity (PV) diagrams in Figure 3.9 show a low-intensity area with a distinct edge at $v_{\rm LSR} \sim +21$ to +27 km s^{-1}. The rest of the inside looks relatively faint. If we assume that this shell is located at the near distance corresponding to +29 km s^{-1}, it is at 2.3 kpc and has a diameter of 120 pc.

Several stellar objects such as SNRs and H II regions were observed in this shell

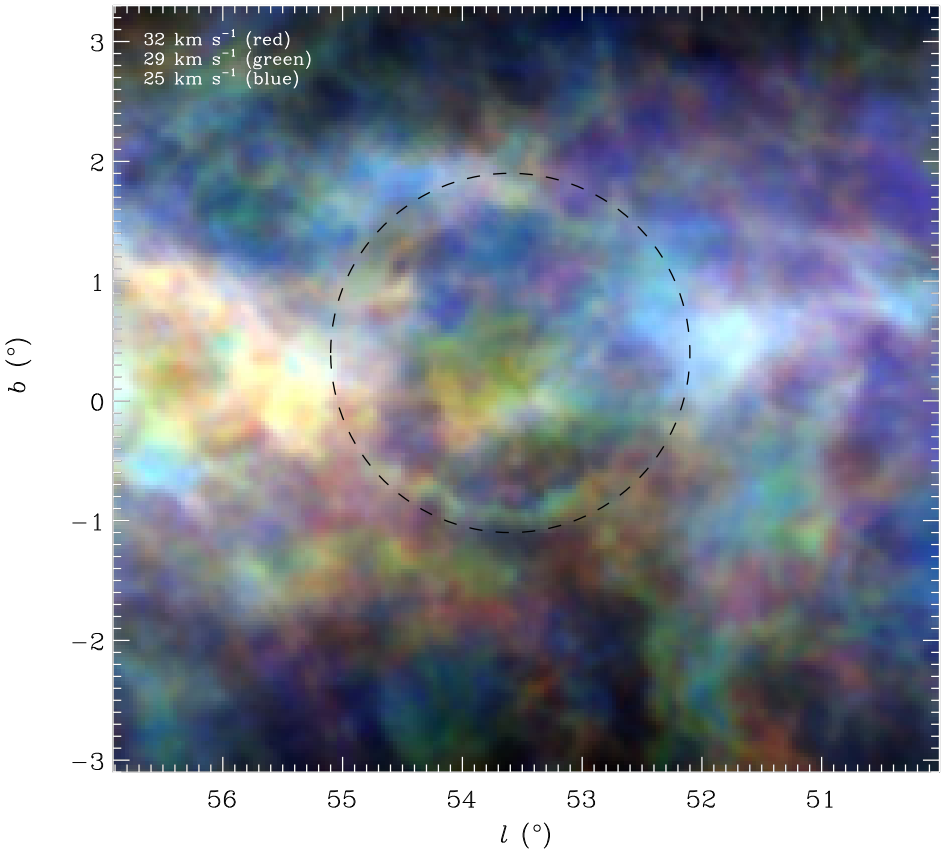

Figure 3.8. H I three-color composite image of GS053.6+00.4+29 at $v_{\rm LSR}$ = $+32, +29, +25$ km s^{-1}. A velocity width of one channel is 0.92 km s^{-1}. A dashed ellipse marks to help locating this shell.

area. Three SNRs, G54.1 + 0.3, G54.4 − 0.3, and G55.0 + 0.3, have been known. For the SNR G54.4 − 0.3, Junkes et al. (1992a) suggested an association with molecular clouds at $v_{\rm LSR}$ = +36 to +44 km s^{-1}. The kinematic distance corresponding the systemic velocity of +40 km s^{-1} depends on the rotation curve and parameters of the solar orbit, and we follow the distance of 3.3 kpc adopted in our previous study of Park et al. (2013). So, SNR G54.4 − 0.3 is located beyond this shell. On the other hand, the other SNRs have been located farther away, ∼ 8 and 14 kpc, respectively (Camilo et al. 2002; Koo et al. 2008; Matthews et al. 1998). Figure 3.9 shows an H I channel map at $v_{\rm LSR}$ = +29 km s^{-1} and two PV diagrams along particular longitude and latitude and marked known *WISE* H II regions (Anderson et al. 2014)[4]. Five *WISE* H II regions appear within the shell in its velocity range: G054.541 − 00.011, G053.644 + 00.14, G53.932 + 01.324, G054.449 + 01.011, and G054.490 + 00.930. Two of them (G053.644 + 00.014 and G054.490 + 00.930) are supposed to be at *far* kinematic distances (Dunham et al. 2011; Anderson et al. 2012). H II region G53.541 − 0.011, on the H I filamentary structure below the center of the H I shell, has a systemic velocity of +23.9 km s^{-1} (Anderson et al. 2011). And, it is probably associated with molecular gas at at $v_{\rm LSR}$ ∼ +24 km s^{-1} (Yu & Wang 2012; Xu & Ju 2014). Hunter & Massey (1990) suggested that it is at a photometric distance of 1.7 kpc. It is not likely that H II region G53.541 − 0.011 is responsible for the H I shell since it is enclosed by a small dust shell (4.23′). However, they can be grouped into a star-forming complex. The other H II regions appear on the northwestern wall and may be triggered by the H I shell. Further analysis will be needed to determine their distances and confirm association with the shell.

[4] The Wide-field Infrared Survey Explorer (*WISE*) catalog of Galatic H II regions lists H II regions and candidates, compiled from *WISE* 12 and 22 μm data. The catalog is accessible on the web page, `http://astro.phys.wvu.edu/wise/`.

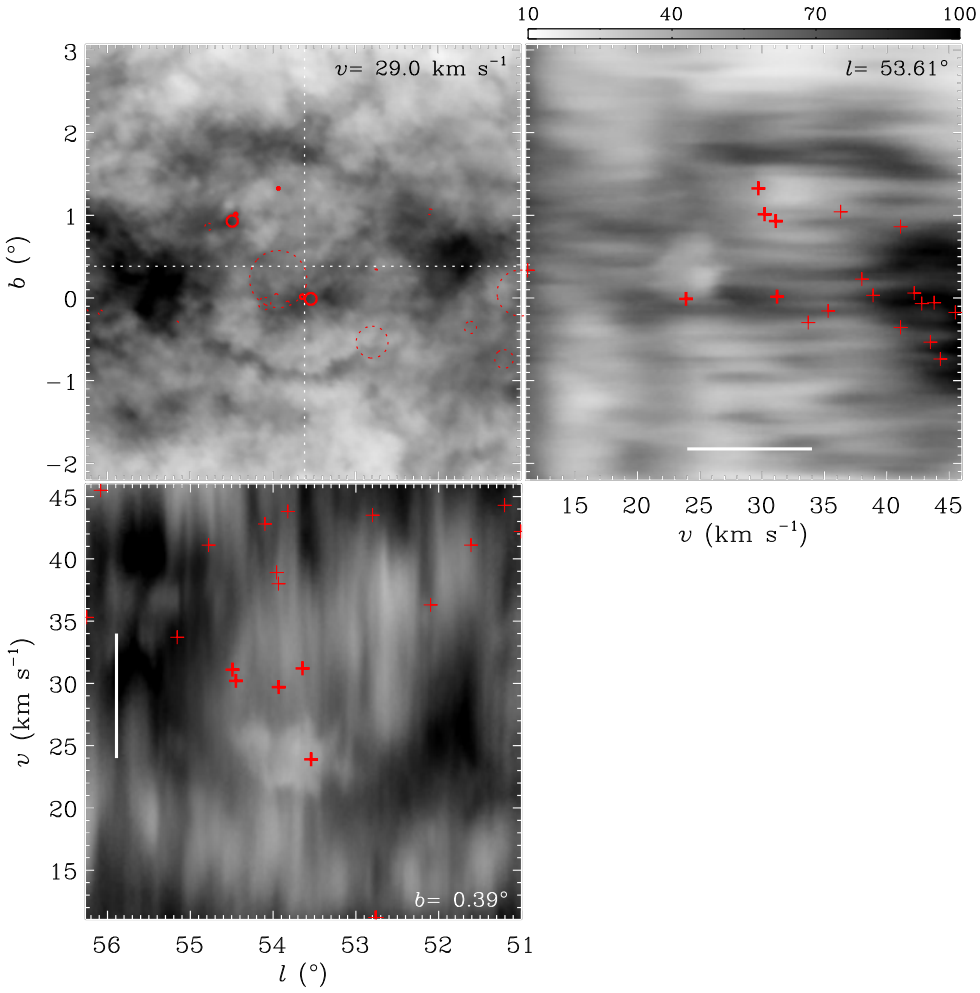

Figure 3.9. H I velocity-channel map ((ℓ, b); upper left) at +29 km s^{-1} and PV diagrams (upper right: (v, b), lower left: (ℓ, v)) at the center of GS053.6+00.4+29. The color bar at the top of the (v, b) image shows the range of H I brightness temperature in Kelvins. Dotted lines in the (ℓ, b) image mark locations where PV diagrams are extracted. *WISE* H II regions are shown using *WISE* angular sizes in the (ℓ, b) image. Those in the velocity range from +24 to +34 km s^{-1}, where the H I shell is visible (shown as white thick solid lines along a v-axis in PV diagrams), are marked with solid circles in (ℓ, b) or thick crosses in PV diagrams, otherwise with dotted circles in (ℓ, b) or thin crosses in PV diagrams.

GS067.5+00.1−93

This is one of the *largest* shells in Table 3.1 and 3.2 in angular size, and the fact that it appears at very negative velocities tells us that its real size will be even very large, i.e., it is likely to be a supershell. The central position is $(\ell,\, b) = (67.^{\circ}5,\, 0.^{\circ}1)$ with an angular size of $15^{\circ} \times 11^{\circ}$. The velocity extension is roughly from -105 to -80 km s^{-1}, but it is quite uncertain. This supershell is clearly seen at $v_{\rm LSR} \sim -88$ km s^{-1}and shapes a longitude-elongated ellipse showing blow-out features toward the northwest and southwest. A belt-like structure at $b \sim 2^{\circ}$ traverses, and its some part in $73^{\circ} \gtrsim l \gtrsim 67^{\circ}$ is relatively week than the other part. At $v_{\rm LSR} \gtrsim -85$ km s^{-1}, another supershell GS064.3−00.9−80 (GS064−01−97) appears just inside the western wall of this supershell. Some parts of the two supershell walls are seemingly overlapped, but, looking closer, bright clumpy features within the walls slightly shift away from each other (*region A* in Figure 3.10). Figure 3.10 is three-color (red/green/blue) composite image at $v_{\rm LSR} = -80, -88, -103$ km s^{-1}. Red and green emission images outline GS064.3−00.9−80 (GS064−01−97) and GS67.5+00.1−95, respectively. A tail-like structure of GS064.3−00.9−80 (GS064−01−97) (*region B* in Figure 3.10) in its southwest is also seen, and, beyond the west end, green emission features are prominent (*region C* in Figure 3.10). There is another shell-like structure, not listed in our catalog, outside the south-west of the imaginary boundary of GS067.5+00.1−93 (*region D* in Figure 3.10). Extended, low-intensity contours seems to connect with the structure and the supershell. Blue emission at higher negative velocity shows almost no emission from part of the supershell walls below the warped disk gas except *region C*. The emission feature in *region C* was reported as FVW $71.0 - 4.0$ by (Kang & Koo 2007), but the association with this supershell is not clear. We note that kinematic distances, converted from LSR velocities, along longitudes in Figure 3.10 at same velocity are very different. For examples, $v_{\rm LSR} = -93$ km s^{-1} at $\ell = 63^{\circ}$ and 73° corresponds to kinematic distances of ~ 19 and 16 kpc, respectively. This shell

is assumed to have the systemic velocity of -93 km s^{-1}, and it gives $d = 17.5$ kpc at $\ell = 67\overset{\circ}{.}5$. Figure 3.11 shows velocity-channel maps from -109 to -69 km s^{-1}. In the directions, two spiral arms in the outer Galaxy has been known (e.g., Kerr 1969; Weaver 1970, 1974; Koo et al. 2017). They are Outer arm and Scutum-Centaurus (Sct-Cen) arm, of which gas seems to be dominant at ~ -70 and ~ -100 km s^{-1}, respectively. GS067.5+00.1−93 appears at velocities between two spiral arms.

3.5 Comments on Heiles' Objects and New Shell Candidates

We found about twice new shell candidates in Table 3.2 as many as confirmed Heiles' shells in Table 3.1. Mean angular geometric diameters ($\sim 3\overset{\circ}{.}2$) of those in Table 3.2 are about two times smaller than those ($\sim 7\overset{\circ}{.}1$) in Table 3.1. For shells in Table 3.2, six are in the inner Galaxy, and nineteen are in the outer Galaxy. Meanwhile, for those in Table 3.1, eight and five are in the inner and outer Galaxy, respectively. Therefore, we found much more shells having smaller apparent sizes, and much more outer Galactic shells. We can think of different resolutions of observational data to explain the results. Since the data that Heiles used have a lower angular resolution of $36'$, it could be difficult to recognize *small-sized* shells which might be less than $\sim$ 4–5 times the beam size. The minimum size of Heiles' shells in Table 3.1 is $\sim 3\overset{\circ}{.}4$. Meanwhile, the data we used have a high resolution of $4'$, and we could discover such *small-sized* shells. We cloud also find outer Galactic shells having such small apparent sizes, which will be hard to identify before. In fact, such outer Galactic shells have larger linear sizes than same apparent-sized inner Galactic shells.

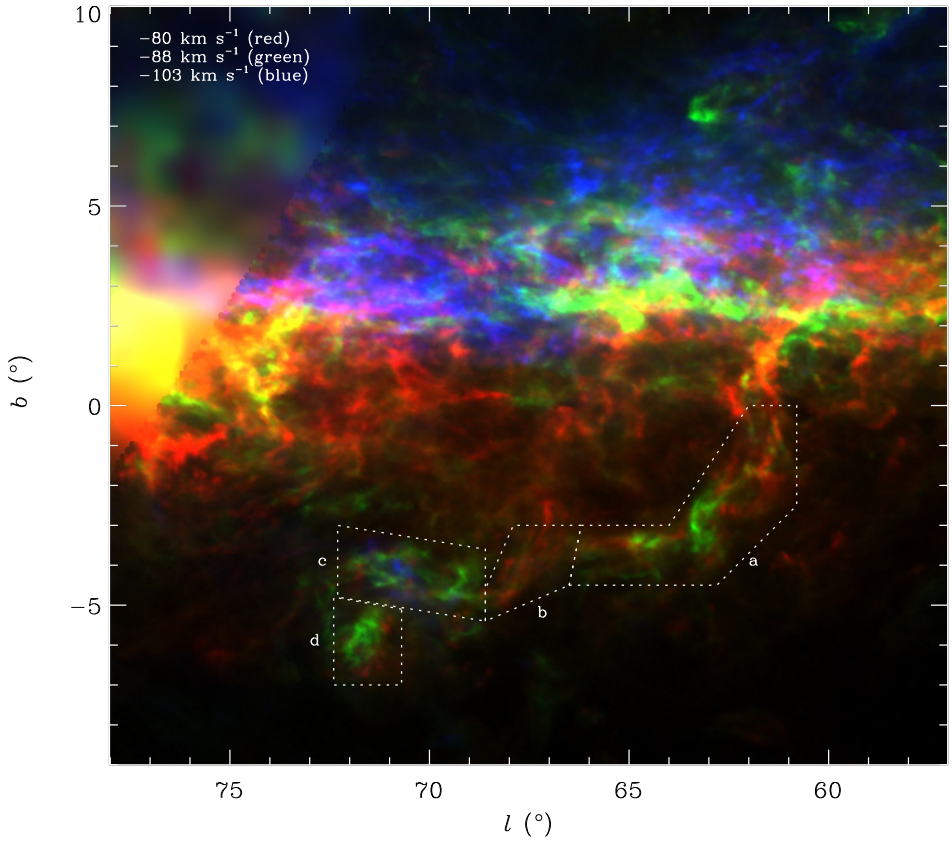

Figure 3.10. H I three-color composite image of GS067.5+00.1−93 at $v_{\rm LSR} = -80, -88, -103$ km s^{-1}. A velocity width of one channel is 0.92 km s^{-1}. Dotted polygons are marked to help locate where is described in the text.

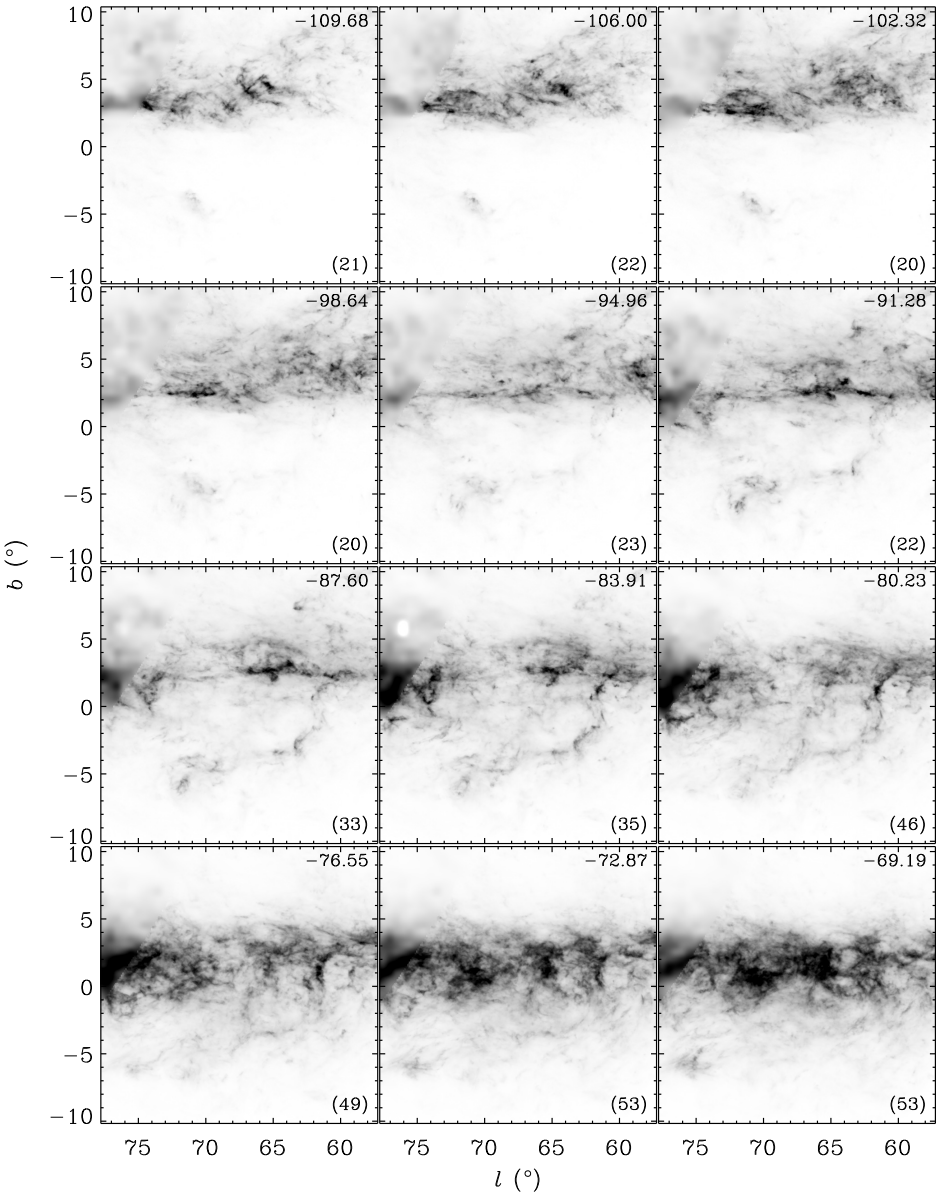

Figure 3.11. H I velocity-channel maps of GS067.5+00.1−93. The central LSR velocity of each channel is written in the bottom right corner in km s^{-1}. The channel width and interval are both 1.84 km s^{-1}. The H I brightness temperature in gray scale ranges from 0 K (white) to the value (black) in parentheses at the bottom left corner of each panel in Kelvins.

3.6 Distance and Physical Parameters

Distance is essential to derive other physical quantities such as a real size, mass, and energy. One of the most common ways is a kinematic distance estimation from an observed LSR velocity with an assumption of a Galactic rotation curve. According to the Galactic rotation, positive LSR velocities are allocated to an object located inside the inner Galaxy in the first quadrant, and negative to the outside. On the one hand, a positive LSR velocity gives two possible distances from us to the object: kinematic *near* and *far* distances compared to a tangential position, where has the maximum LSR velocity allowed by the Galactic rotation model in the same line of sight. We adopted reference velocities in Tables 3.1 and 3.2 as systemic LSR velocities of shells. And we used the Galactic rotation curve of Brand & Blitz (1993) with IAU standard values $\Theta_{\odot} = 220$ km s^{-1}and $R_{\odot} = 8.5$ kpc. Table 3.3 show the results of our calculations. For the inner Galactic shells except one, we assumed that they are at near distances. There are four shells (marked with "*a*" in the last column of Table 3.3) seen at forbidden velocities by the Galactic rotation model, and they are assumed to be at a tangential position. For the outer Galactic shells, there is no distance ambiguity in principle. However, three shells (marked with "*b*" in the last column of Table 3.3) have pretty larger negative velocities than values of the most distant spiral arm, Sct-Cen arm ($\sim$ 20 kpc). The emission features of the H I shells in position-velocity diagrams look like FVWs, and actually, two of them were identified as FVWs by Kang & Koo (2007) using low-resolution data. Also, as one of them, GS040.2+00.6−70 is considered to be located at the Sct-Cen arm since disrupted H I gas feature does not appear at lower negative velocities than the velocity range of the arm (Park et al. 2016). The others are in a similar situation with GS040.2+00.6−70, and we assumed that they are in the same spiral arm. The Sct-Cen arm has almost same heliocentric distances along longitudes of the I-GALFA survey area.

Our distance calculations assume that H I gas perfectly follows the Galactic ro-

tation model, but it is not the case in reality. A departure from the model which is caused mainly by streaming motion will contribute to the uncertainty, and its typical one-dimensional value is 12 km s^{-1} (e.g., Brand & Blitz 1993), which corresponds to one to a few kpc-scale for our objects.

Table 3.3 lists Galactocentric ($R_{\rm Gal}$) and heliocentric (d) distances, shells' linear radius ($R_{\rm sh}$), heights from the midplane (z), and initial explosion energy ($E_{\rm E}$) of our shell list. We note that given kinematic distances in this chapter may be quite uncertain, but are still useful if there is no further information to decide a distance. The derived radii of shells range from 25 pc to 2 kpc with a mean of $\sim$ 380 pc. For relatively complete shells, we obtained angular offsets between shell's central latitudes and intensity-weighted mean latitudes from the LAB data and converted them to linear heights (z) using given distances. The reason to use the LAB data is that some shells are not fully covered by the I-GALFA survey data. It is almost insignificant since we use mean $b-$profiles which are averaged over broad ranges in longitude ($\Delta l = 5^\circ$) and velocity ($\Delta v = 20$ km s^{-1}). Half-thickness of the H I gas disk is known to be roughly 100–150 pc for the inner Galaxy and 200–500 pc for the outer Galaxy (Kalberla & Dedes 2008; Levine et al. 2006). Several shells having derived z are placed at quite high heights. We also inferred an explosion energy using equations (2–3) of Heiles (1979) supposing that multiple SN explosions produces a shell: for stationary shells, $E_{\rm E} \sim 9.7 \times 10^{44}\, n_0^{1.12}\, {R_{\rm sh}}^{3.12}$; for expanding shells, $E_{\rm E} \sim 5.3 \times 10^{43}\, n_0^{1.12}\, {R_{\rm sh}}^{3.12}\, {v_{\rm exp}}^{1.4}$. The explosion energy needs a current radius of a shell ($R_{\rm sh}$) in parsec and an ambient hydrogen density (n_0) before the explosion in cm^{-3}, also in expanding case an expansion speed of a shell ($v_{\rm exp}$) in km s^{-1}. Dependence on a variance of n_0 or $v_{\rm exp}$ is relatively insignificant than that of $R_{\rm sh}$. We assumed that $n_0 = 1\,{\rm cm}^{-3}$ and $0.1\,{\rm cm}^{-3}$ for inner and outer Galactic shells, respectively, and $v_{\rm exp} = 10$ km s^{-1} for expanding shells. Eight of Heiles' shells in Table 3.1 and seven of new shell candidates in Table 3.2 requires a tremendous

energy of $E_{\rm E} \geq 3 \times 10^{52}$ erg. Values that we give are very rough estimates and should be treated with caution.

3.7 Comparison with Other Shells or Bubbles Catalogs

After completing the shell lists in Tables 3.1 and 3.2 and substantial analysis, two shell catalogs (partially) covering the I-GALFA survey area were published by Ehlerová & Palouš (2013) and Sallmen et al. (2015). Ehlerová & Palouš (2013) provided the catalog done by an automatic search uniformly over the whole sky using relatively low-resolution data. Their algorithm finds H I shell candidates regardless of expansion but having closed structures. And, Sallmen et al. (2015) did a visual inspection for searching H I shells in a significant portion of the Arecibo sky using the SETH I survey data. The SETH I survey covers the full range of R.A., but the narrower range of Declination ($7\overset{\circ}{.}2 < \delta < 29\overset{\circ}{.}7$) than one of the I-GALFA survey ($-1\overset{\circ}{.}27 \lesssim \delta \lesssim 37\overset{\circ}{.}93$). In other words, about half area of the I-GALFA survey is overlapped with the SETH I survey area. The final data of the SETH I survey have a similar sensitivity (0.25 K) but a slightly larger angular resolution ($6'$). By comparison between figures in this chapter and those in Sallmen et al. (2015), it is clear that the I-GALFA survey data provide a better image quality.

We carried out the comparison with the above two catalogs. First, there are thirty-one among Ehlerova's shells in the I-GALFA survey area: eight are ranged in negative LSR velocities, eighteen in positive, and five in both. In our view, seven of them are matched or related to our list: one with ours and the others with reconfirmed Heiles' shells. Many of the rest seem to be still ambiguous when seeing in the I-GALFA data. The number of comparable shells is quite small, and most objects matched are similar with Heiles' shells. That might be because the method of Ehlerová & Palouš (2013) is limited in relatively well-defined holes and they used data with much lower resolution than what we used but almost same with what

Table 3.3

Physical Parameters of H I Shells/Supershells in Tables 3.1 and 3.2

Name	$R_{\rm Gal}$ (kpc)	d (kpc)	$R_{\rm sh}$ (pc)	z (pc)	$E_{\rm exp}$ (erg)	Note*
GS031.4+01.1+65	5.4	4.2	40	+100	1×10^{50}	···
GS034.2+02.4−77	13.8	20.0	300	···	5×10^{51}	*b*
GS034.5−01.1+72	5.4	4.6	110	−90	2×10^{51}	···
GS034.7−05.5+61	5.7	4.0	270	···	4×10^{52}	···
GS035.1+05.9+57	5.8	3.8	300	···	5×10^{52}	···
GS036.4+00.8−37	12.2	18.0	390	0	1×10^{52}	···
GS036.8−01.1−35	11.9	17.5	620	−460	5×10^{52}	···
GS037.5+00.5−39	12.4	18.0	390	−60	1×10^{52}	···
GS037.9+00.5−25	10.7	16.0	400	···	1×10^{52}	···
GS040.2+00.6−70	14.6	20.0	450	−420	7×10^{52}	*b*†
GS042.0+00.4+29	7.1	2.0	210	+10	5×10^{52}‡	···
GS044.3−00.1−39	11.7	16.2	510	···	3×10^{52}	···
GS044.9−12.8+20	7.6	1.4	25	···	2×10^{49}	···
GS045.0−08.1+32	7.1	2.3	44	−340	1×10^{50}	···
GS045.4−01.1+93	6.1	6.0	310	···	6×10^{52}	*a*
GS046.6−00.4−17	9.7	13.3	390	···	1×10^{52}	···
GS047.0+01.2−35	11.1	15.0	260	+200	3×10^{51}	···
GS047.6−00.1−98	15.6	20.0	210	···	2×10^{51}	*b*
GS048.3−00.8−25	10.3	13.7	590	−330	4×10^{52}	···
GS048.4+00.6−40	11.6	15.3	200	0	1×10^{51}	···
GS053.0−05.0+26	7.5	2.0	190	···	1×10^{52}	···
GS053.6−00.2+5	8.5	10.1	180	···	1×10^{52}	*c*§
GS053.6+00.4+29	7.4	2.3	60	0	3×10^{50}	···
GS056.1−02.1−21	9.8	11.6	170	−510	1×10^{51}	···
GS056.8+00.1−21	9.8	11.4	520	−60	3×10^{52}	···
GS057.7+02.6−14	9.3	10.5	430	+400	2×10^{52}	···
GS060.2+01.1−74	14.4	16.6	460	−60	2×10^{52}	···
GS061.3+02.6−69	13.7	15.6	240	···	3×10^{51}	···
GS061.6−00.4+54	7.5	4.0	150	···	6×10^{51}	*a*
GS063.3−00.4−3	8.8	8.2	280	···	6×10^{51}	···
GS063.6+01.0−71	13.8	15.3	570	0	4×10^{52}	···
GS064.0−01.1+45	7.6	3.7	240	···	3×10^{52}	*a*
GS064.3−00.9−80	14.8	16.4	900	−660	2×10^{53}	···

Continued on Next Page...

Table 3.3 – Continued

Name	$R_{\rm Gal}$ (kpc)	d (kpc)	$R_{\rm sh}$ (pc)	z (pc)	$E_{\rm exp}$ (erg)	Note*
GS066.8−02.1−39	10.8	10.8	710	···	8×10^{52}	···
GS067.5+00.1−93	16.3	17.5	2000	−700	2×10^{54}	···
GS072.3+01.3−46	11.2	10.3	580	···	4×10^{52}	···
GS072.3+03.1−56	12.0	11.4	410	···	1×10^{52}	···
GS074.8−00.9+29	8.2	2.2	160	···	1×10^{52}	*a*

Note. $R_{\rm Gal}$: Galactocentric distance, d: Heliocentric distance, $R_{\rm sh}$: geometric mean radius, z: altitude from the midplane, $E_{\rm exp}$: explosion energy to form a shell.

*Shells marked with alphabets in the last column are assumed to be at the tangent position for *a*, the most distant spiral arm ($\sim$ 20 kpc) for *b*, and far distance under the circumstances for *c*.

†Park et al. (2016).

‡We aussumed $n_0 = 1\,{\rm cm}^{-3}$, and adopted $v_{\rm exp} = 18.3$ km s^{-1} inferred in Section 3.3.2.

§This shell is visible around $v_{\rm LSR} = 0$ km s^{-1}, and a difference between corresponding kinematic near and far distances is quite large ($\sim$ 10 kpc). Accordingly, angular scales of H I gas features at each position seem to be different and distinguishable: H I gas at the near distance looks like cirrus clouds distributed over the whole I-GALFA mapping region, but one at the far distance seems to be lumping clouds crowded around $b = 0^\circ$. This shell appears to be the latter case.

Heiles used. Second, there are twenty of Sallmen's shells in the I-GALFA survey area: six are comparable to five shells in our list (three of ours and two of re-confirmed Heiles' shells), but fourteen are not. In reverse, considering only new shell candidates in Table 3.2, twelve of ours are within the SETH I survey area, and, as mentioned above, three of them are comparable to Sallen's shells. (We maintain the three shells in the new candidate list, but the readers should refer Sallmen et al. (2015) also.) That is because visual inspection is subjective and detailed structures of interstellar gas are very complicated. The comparison results of individual shells are written in Appendix B.

We also tried to match with the catalog of *GLIMPSE* bubbles (Churchwell et al. 2006), but many of the IR bubbles have much smaller sizes (mostly, less than $10'$). So, it is unlikely to be in one-to-one correspondence. There might be IR bubbles generated from young stellar sources which are triggered by feedback of H I shells on the ISM. However, we would not deal with the topic in this chapter.

Visual examinations can be strongly affected by investigator bias, while automatic search will depend on how much criteria of the search algorithm reflect complex reality. The former has the advantage of linking discontinuous structures into a single entity even in complex environments, and the latter is good at uniform application over large data. The two methods could be necessary to maximize finding H I shells. Thus they are complementary each other. As seen above, our shell list provides additional shell candidates undiscovered by other shell catalogs. Also, the high-resolution analysis using high-quality data will be helpful to understand individual objects comparing the surrounding gas.

3.8 Discussion

3.8.1 Galactocentric Radius Distribution of H I Shells/Supershells and the Origin of Supershells

SN explosions are acceptable as energy sources to form H I shells/supershells. For examples, GS034.7−05.5+61 (GS034−06+65), GS035.1+05.9+57 (GS036+06+55), GS042.0+00.4+29 (GS041+01+27), GS053.6+00.4+29, and GS074.8−00.9+29 (GS075−01+39) are very likely to be generated by stellar activities such as stellar winds and/or multiple SN explosions since these seem to be located in active star-forming regions (see Sections 3.3 and 3.4). In this section, we try to compare Galactocentric radius distribution of H I shells and other objects implying star-forming regions.

Most H I shells in Tables 3.1 and 3.2 require much more than one SN (Section 3.6). About 60% (twenty-four) of the whole are in the outer Galaxy, and 33% (eight) of the outer Galactic shells are at quite far Galactocentric distances ($R_{\rm Gal} \gtrsim 14$ kpc). When seeing only our results H I shells/supershells seem to be not rare in the outer Galaxy. However, the distribution of Galactic H II regions in Figure 5 of Anderson et al. (2015) shows that they are mostly concentrated on about 4–8 kpc, that is in the inner Galaxy, although a non-negligible number of the objects were detected beyond the solar circle. Comparison with the distribution of H II regions may be rather to indicate the absence of many H I shells/supershells in the inner Galaxy. It is unlikely that current H II regions are directly related to the formation of H I shells because most of them are surrounded by much smaller gas bubbles. Stochastically, however, the comparison result is still meaningful because the distribution of previous generations is likely too.

Massive star clusters, which contain many massive stars and can be evolved to H I supershells, are also expected to be mostly located in the inner Galaxy. However,

two-thirds of our H I supershells, requiring $E_{\rm E} \geq 3{\times}10^{52}$ erg, are in the outer Galaxy. It may be caused by missing many inner Galactic H I supershells. We checked the fact using giant molecular clouds (GMCs) since stars are born in there, and significant massive stars are evolved in place. Recently, Miville-Deschênes et al. (2017) presented a molecular cloud catalog over the entire Galactic plane using ^{12}CO data of Dame et al. (2001), which cover 98% of Galatic ^{12}CO emission. Instead of using surface intensity, we counted the number of massive molecular clouds which have enough mass to make massive star clusters and then finally supershells. To drive the lowest cloud mass, we assumed that 1% of parent molecular cloud mass contributes to forming star clusters (e.g., Lada 2016). Also, we adopt initial mass function (IMF) of Kroupa (2001), which is a form of multiple-part power-law, to populate star clusters. The power-law index is -2.3 for star mass $\geq 0.5\,M_{\odot}$, and, according to the IMF, such stars occupy 68% in cluster mass. We considered that a star cluster could be evolved to a supershell if it has initially at least 40 stars having mass $\geq 8\,M_{\odot}$, as following a discussion in Heiles (1987). So, the minimum cloud mass is $3.9 \times 10^5\,M_{\odot}$. Finally, the number of the molecular clouds selected in $l = 32^{\circ}$ to 77° is 109.

Figure 3.12 shows the number of such GMCs which are limited in the I-GALFA longitude range ($l = 32^{\circ}$ to 77°) within Galactocentric rings of increasing $R_{\rm Gal}$. First, see the top panel of Figure 3.12. I-GALFA H I supershells and *WISE* H II regions are also overlapped to make comparisons. Note that the *WISE* H II regions considered here are those with measured velocities, from single velocity component of ionized gas, however the original *WISE* catalog contains many H II regions with no available velocity information or multiple velocity components. The total number of H II regions used here is 591. Emptied bins at $R_{\rm Gal} \lesssim 4.5$ kpc in the diagram is caused by a limit of the I-GALFA longitude range. Most of the selected GMCs are located within $R_{\rm Gal} \leq 9$ kpc and concentrated near $R_{\rm Gal} \sim 6$ and 8.5 kpc where are very likely to be spiral arms. A small fraction, but the non-negligible number

of GMCs are in the outer Galaxy. There is no GMC at $R_{\rm Gal} \geq 15$ kpc. It is not surprising that the distributions of GMCs and H II regions are analogous to each other since massive stars are born predominantly in GMCs (Lada & Lada 2003). H II regions present higher levels since we could not give a constraint in brightness, but the trend will not be changed much. On the other hand, in the inner Galaxy, the number of H I supershells we found seem to be tiny comparing with that of GMCs. It may be explained as that inner Galactic supershells are easy to be open at the top because of low scale height of the Galactic gaseous disk, and look like "worms" (Heiles 1984; Koo et al. 1992). In the bottom panel of Figure 3.12, Galactic worms listed by Koo et al. (1992) are added, and the diagram indeed shows that the found worms significantly contribute the inner Galaxy.

Meanwhile, at very far distances ($R_{\rm Gal} \gtrsim 15$ kpc) are two H I supershells which need gigantic explosion energy, more than 10^{53} erg, i.e., more than hundred simultaneous SN explosions. It is hard to imagine very massive star-forming regions at such vast distances. Therefore, alternative mechanisms are still required, and actually, we had reported that GS040.2+00.6−70, one of our H I supershells, was produced by HVC interaction with disk materials (Park et al. 2016). Furthermore, the two H I supershells, GS064.3−00.9−80 (GS064−01−97) and GS067.5+00.1−93, may be produced by HVC collisions, and also there might be more examples. To find additional examples of CHVC-supershell systems similar to GS040.2+00.6−70, we checked whether known CHVCs of de Heij et al. (2002) are related with our shells, but also whether there is undiscovered HVC emission in the sight-lines of our shells. In the directions of three H I shells, GS035.1+05.9+57 (GS036+06+55), GS053.6+00.4+29, and GS057.7+02.6−14 (GS057+03−11), some known CHVCs exist on the edge of each shell, but there does not seem to correlate morphologically, i.e., it is a coincidence. Moreover, we could not find new H I features possibly related with our shells. It might be because it is rare to observe a CHVC-supershell system

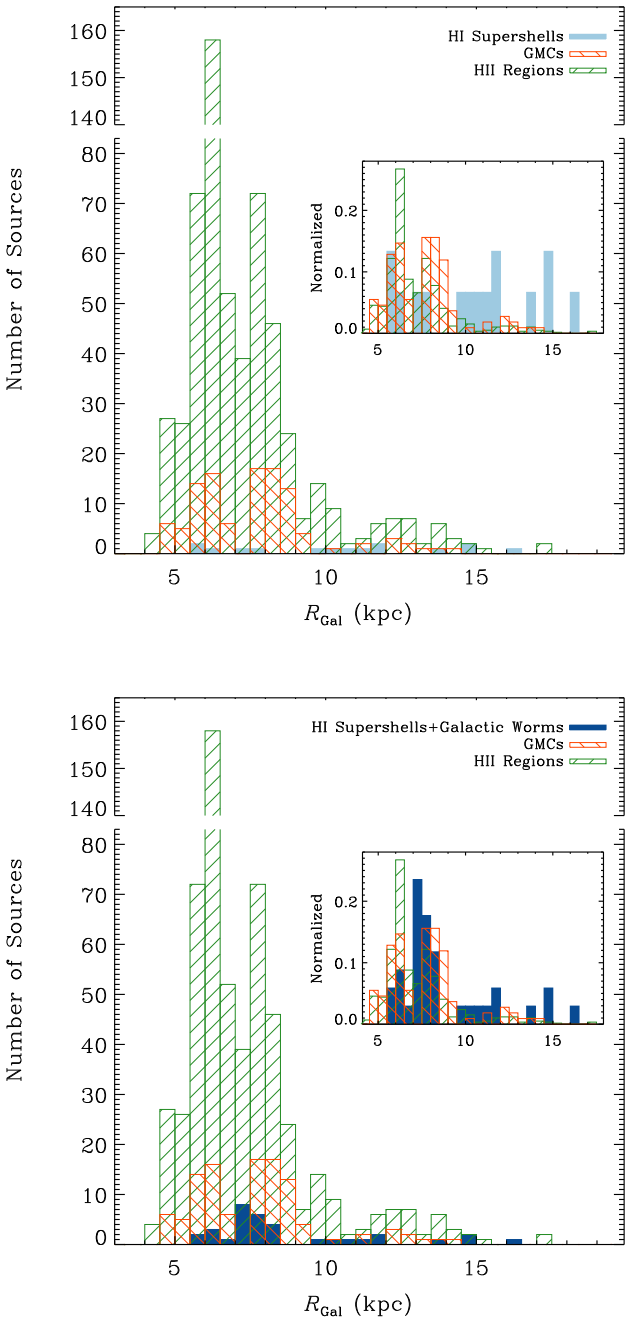

Figure 3.12. The number of objects vs. Galactocentric radius, including Galactic worms (bottom) or not (top). (Continued on the following page.)

in the same line of sight. Also, it could be hard to connect the two objects if the collision time elapses enough that a colliding HVC gets out of the solid angle of an H I shell.

Figure 3.12. (Previous page.) Cyan filled histogram for I-GALFA H I supershells, red backward-diagonally hatched for GMCs having mass $\geq 3.9 \times 10^5\,M_\odot$ (Miville-Deschênes et al. 2017), and green forward-diagonally hatched for *WISE* H II regions (Anderson et al. 2014). In the bottom panel, blue filled histogram indicates the sum of the I-GALFA H I supershells and Galactic worms cataloged by Koo et al. (1992). Each object is counted within an arc-like area with a width of 0.5 kpc and $l = (32°, 77°)$. Inset is same, but normalized. See Section 3.8.1 for details.

3.8.2 H I Shells/Supershells and Formation of Molecular Clouds

The effect of H I shells on the ISM is also important, and one of the major issues is the formation of molecular clouds in H I shell walls. It has been believed that molecular gas can be formed in compressed atomic shells where gas piled up (e.g., Dawson 2013, references therein). As an individual example, molecular clouds were observed in CO line in walls of GSH 287+04−17 and GSH 277+00+36 (Dawson et al. 2011). CO clouds embedded within H I shell walls, elongated along their inner edges were suggested as newly-born clouds in situ while those located at the tips of H I features were thought to be remnants of pre-existing molecular clouds. We will give an additional potential example of such a case among our shell list.

Comparison with CO Data

We examined CO emission in/near the shells since CO is a general tracer of molecular gas. We mainly used the composite ^{12}CO $J = 1 - 0$ line survey done by the 1.2-m

telescope at the CfA (angular resolution = 8′.4; 1 pixel = 7′.5; velocity resolution = 0.65 km s^{-1}; T_{rms} = 0.18 K; Dame et al. 2001). In the first Galactic quadrant, it covers almost part of the Galactic disk within $b = \pm 5^{\circ}$ with the velocity range of (−90, +180) km s^{-1}, and several areas at higher latitudes over more limited velocity ranges. For comparison, we looked into a velocity-integrated map over the velocity range where a shell is visible in H I emission to check whether there is a CO emission feature brighter than $\sim$ 1.5 K km s^{-1} near shell walls. And then we examined velocity-channel maps or CO line profiles of the found CO features. Description and results of comparison with the CO data are given in Appendix C. In summary, about a half of the H I shells in Tables 3.1 and 3.2 are likely to have CO emission which is probably associated with each shell. Most of CO emission features appear near shell walls. However, many of them occupy one or a few pixels, which may mean that they are not sufficiently resolved in the CfA survey data. Higher resolution observations are necessary to measure the exact locations of CO and to confirm association with H I shells. Nonetheless, in the next section, we will look over one of the most interesting regions that contain two shells, GS060.2+01.1−74 and GS063.6+01.0−71, in the outer Galaxy.

The Region of GS060.2+01.1−74 and GS063.6+01.0−71

Two shells, GS060.2+01.1−74 and GS063.6+01.0−71, are right next to each other, and the eastern wall of the former and the western wall of the latter seem to be overlapped. CO emission can be found at several walls of GS063.6−01.0−71, some of which are the overlapping parts. Hereafter, we will call this region where CO emission is detected as the GS064 region. The top image of Figure 3.13 shows a velocity-integrated H I image over the velocity range of (−80, −65) km s^{-1} with contours of ^{12}CO $J = 1 - 0$ and $2 - 1$ transitions (Hereafter, respective of CO 1–0 and CO 2–1) in the GS064 region. We used the CfA CO 1–0 survey data and CO 2–1 data. The

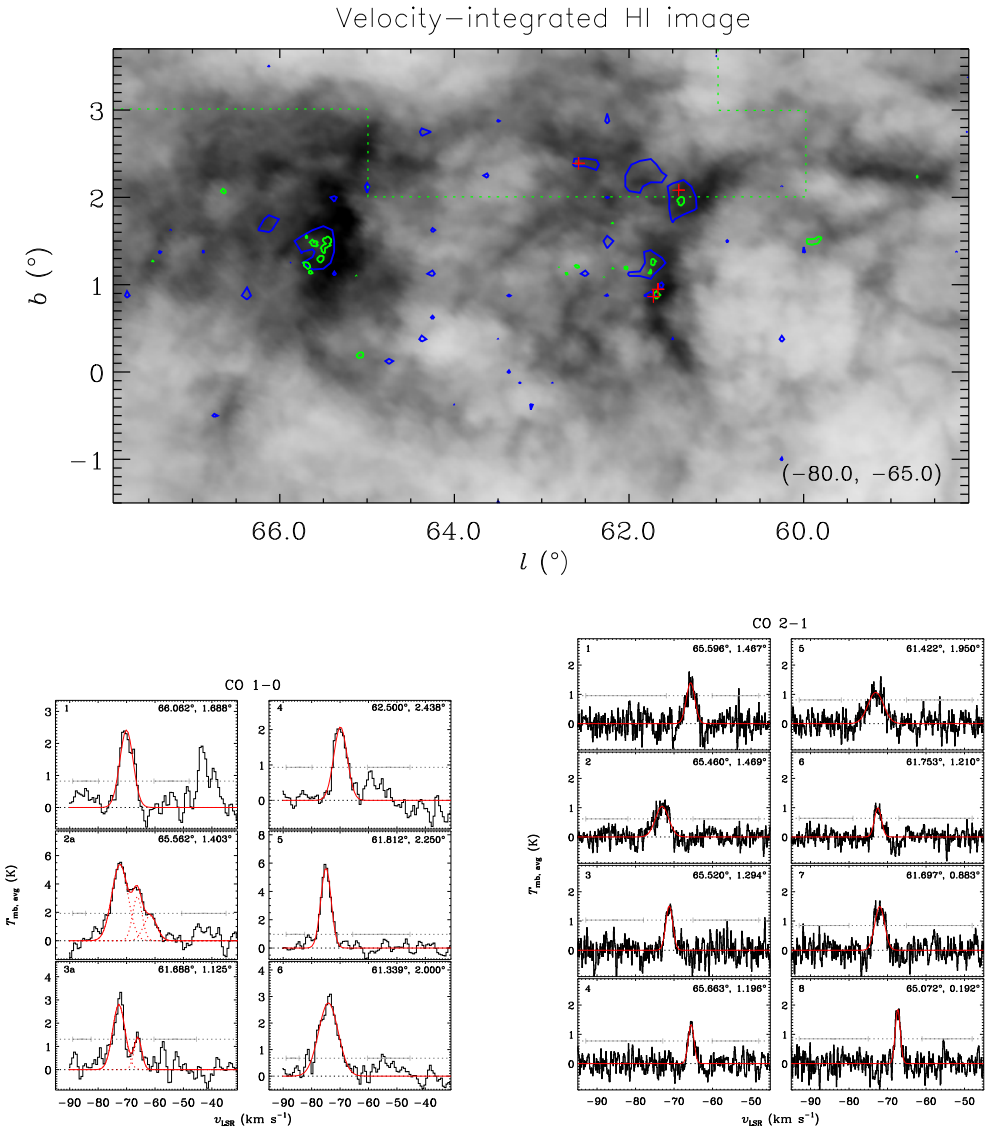

Figure 3.13. For the GS064 region, velocity-integrated H I image overlaid with CO contours (top) and average line profiles of several local areas in ^{12}CO $J = 1 - 0$ (bottom left) and ^{12}CO $J = 2 - 1$ (bottom right). (Continued on the following page.)

latter obtained using a 1.85-m telescope at the Nobeyama Radio Observatory by the radio astronomy group at Osaka Prefecture University in Japan (angular resolution $\sim 3'$; velocity resolution ~ 0.08 km s^{-1}; typical $T_{rms} \sim 0.8$ K at $\Delta v \sim 0.1$ km s^{-1}). The CO 2–1 data partially cover the GS064 region. As shown in Figure 3.13, CO emission features appear beside where H I emission is bright. Most CO clouds are marginally resolved in both CO transitions. They are likely to be associated with H I shell walls there, which is supported by agreement in location. However, it is not simple to conclude whether the molecular clouds are newly formed by shell walls or pre-existing clouds remain.

Figure 3.13. (Previous page.) Top: The velocity range to integrate is $(-80, -65)$ km s^{-1}. The inverted gray scale ranges from 0 K km s^{-1} (white) to 1100 K km s^{-1} (black). Blue and green contours are ^{12}CO $J = 1 - 0$ observed by the CfA survey and ^{12}CO $J = 2 - 1$ detected with the 1.85-m telescope at the Nobeyama Radio Observatory. A contour level for both is 2 K km s^{-1}, respectively. Green dotted line indicates area boundary observed in ^{12}CO $J = 2 - 1$. Red crosses show locations of *WISE* H II regions within the same velocity range. Bottom left: The site and number of each line profile described in Table 3.4 are written in the upper right and left corners, respectively. The geometric mean radius of the local area is listed in Table 3.4. A red solid curve is a fitted line using a Gaussian function with a single component except for the left second and third panels, of which the profile decomposes to multiple components (red dotted lines). A horizontal, gray dotted line is a 3σ level calculated from the velocity range marked with solid gray lines. Bottom right: Same as those left but for CO 2–1 line profiles. Each line profile is Hanning-smoothed.

We give properties of CO clouds detected in the GS064 regions in Table 3.4.

First, we picked up CO features which have at least comparable to a beam size and obtained average line profiles there shown in Figures 3.13, and then apply Gaussian fit to them. Table 3.4 lists locations of the CO clouds, Gaussian parameters (peak main beam temperature ($T_{\rm mb,pk}$), central velocity (v_0), velocity dispersion (σ_v), and velocity-integrated main beam temperature ($W_{\rm CO}$)) of the average line profiles, *angular radii* (r_θ) of the cloud areas, heliocentric distances (d), CO luminosity-based H_2 masses ($M_{\rm H_2}$), *corrected linear radii* (r'), virial masses ($M_{\rm vir}$), and some notes of association between CO 1–0 and CO 2–1 clouds. For the parameters above related with radius, r is of an imaginary circular extent equal to the projected area of each feature in arcminutes while r' is a corresponding value at a given distance which is deconvolved with a beam size ($\theta_{\rm beam}$) to correct the beam-spreading effect ($r' = \sqrt{(r_\theta/\pi)^2 - (\theta_{\rm beam}/\pi)^2}\, d$). A kinematic distance (d) is derived from Gaussian central velocity assuming the Galactic rotation model of Brand & Blitz (1993). $M_{\rm H_2}$ is generally determined by the empirical relationship between CO 1–0 integrated intensity ($W_{\rm CO\,1-0}$) and molecular hydrogen column density ($N_{\rm H_2}$): $M_{\rm H_2}/M_\odot = N_{\rm H_2} \times area = X \mu\, m_{\rm H} W_{\rm CO\,1-0} \times area = 13.59\, X\, W_{\rm CO\,1-0} r_\theta d$, where μ is the molecular weight (= 2.9), and X is the conversion factor. We adopted $X = 2 \times 10^{20}\ ({\rm K\,km\,s^{-1}})^{-1}\,{\rm cm^{-2}}$ with an uncertainty of 30% (Bolatto et al. 2013). For the CO 2–1 transition, the above equation should be divided by the line ratio, $R_{21} = W_{\rm CO\,2-1}/W_{\rm CO\,1-0}$. We adopted $R_{21} = 0.64 \pm 0.05$ which is the median value throughout the Milky Way (Heyer & Dame 2015).[5] Virial masses are estimated using the equation of $M_{\rm vir}/M_\odot = 1047\, r' {\sigma_v}^2$, assuming a spherically symmetric cloud which is gravitationally bound with a 1/r density distribution (e.g., Solomon et al. 1987; Rosolowsky & Leroy 2006).

Two profiles in CO 1–0 are decomposed into multiple components while the

[5]The line ratio in a large Galactocentric radius might be lower than the median value (Sakamoto et al. 1997). So, the cloud mass from CO 2–1 emission might be underestimated, but it is not clear whether the fact can explain a big difference between cloud masses from CO 1–0 and CO 2–1.

Table 3.4

Properties of Molecular Clouds detected in ^{12}CO $J = 1 - 0$ and $J = 2 - 1$ in the GS064 Region

No.	Position		Observed Properties					Derived Properties				Ass?*
	ℓ	b	$T_{\rm mb,pk}$	v_0	σ_v	$W_{\rm CO}$	r_θ	d	$M_{\rm H_2}$	r'	$M_{\rm vir}$	
	(°)	(°)	(K)	(km s^{-1})	(km s^{-1})	(K km s^{-1})	($'$)	(kpc)	($M_\odot$)	(pc)	($M_\odot$)	
					^{12}CO $J = 1 - 0$							
1	66.062	+1.688	2.42±0.13	−70.04±0.15	2.34±0.15	14.17	12.0	14.5	5.01×10^5	35	2.00×10^5	···
2a	65.562	+1.403	5.38±0.26	−72.35±0.21	2.83±0.06	38.25	18.0	14.6	3.16×10^6	68	5.72×10^5	*a*
2b			3.13±0.49	−66.22±0.36	1.66±0.16	13.01		14.1	9.69×10^5	65	1.87×10^5	*b*
2c			1.77±0.34	−61.68±0.86	2.28±0.23	10.12		13.5	6.93×10^5	62	3.36×10^5	···
3a	61.688	+1.125	2.81±0.20	−72.71±0.21	2.18±0.08	15.35	13.4	16.0	8.02×10^5	48	2.39×10^5	*c*
3b			1.38±0.30	−66.03±0.33	1.33±0.09	4.62		15.0	2.11×10^5	45	8.37×10^4	···
4	62.500	+2.438	2.08±0.15	−69.86±0.20	2.35±0.20	12.23	10.4	15.4	3.67×10^5	26	1.50×10^5	···
5	61.812	+2.250	5.67±0.18	−74.96±0.07	1.81±0.07	25.68	12.0	16.3	1.13×10^6	40	1.37×10^5	···
6	61.339	+2.000	2.76±0.09	−74.11±0.13	3.45±0.13	23.88	11.2	16.3	9.12×10^5	35	4.37×10^5	*d*
					^{12}CO $J = 2 - 1$							
1	65.596	+1.467	1.39±0.08	−65.70±0.07	1.12±0.07	3.90	3.2	14.0	1.40×10^4	5	6.54×10^3	*b*
2	65.460	+1.469	1.04±0.04	−73.10±0.08	1.73±0.08	4.50	5.2	15.0	5.06×10^4	18	5.61×10^4	*a*
3	65.520	+1.294	1.51±0.09	−71.24±0.07	0.91±0.07	3.44	3.3	14.8	1.43×10^4	6	5.21×10^3	*a*
4	65.663	+1.196	1.33±0.08	−65.56±0.05	0.75±0.05	2.51	4.5	14.0	1.73×10^4	13	7.75×10^3	*b*
5	61.422	+1.950	1.07±0.05	−73.05±0.11	2.02±0.11	5.38	3.7	16.1	3.30×10^4	10	4.25×10^4	*d* †
6	61.753	+1.210	0.99±0.06	−72.49±0.06	0.91±0.06	2.26	4.5	15.9	2.12×10^4	15	1.31×10^4	*c*
7	61.697	+0.883	1.49±0.07	−72.03±0.06	1.28±0.06	4.79	3.2	15.9	2.29×10^4	6	1.03×10^4	*c*
8	65.072	+0.192	1.84±0.09	−67.34±0.04	0.66±0.04	3.07	3.1	14.4	1.10×10^4	3	1.39×10^3	···

Note. Column 1: cloud numbers (Those by adding an alphabet signify multiple velocity components.) ; Columns 2–3: Galactic locations of clouds; Columns 4–7: Parameters obtained by Gaussian fit, Peak main beam temperature ($T_{\rm mb,pk}$), central velocity (v_0), velocity dispersion (σ_v), and velocity-integrated main beam temperature ($W_{\rm CO}$); Column 8: *circular radii* (r_θ) which have the same areas with the cloud areas in arcminutes; Columns 9–10: heliocentric distances (d) and CO luminosity-based H_2 masses ($M_{\rm H_2}$); Columns 11–12: *corrected radii* (r') in parsecs and virial masses ($M_{\rm vir}$). See Section 3.8.2 for details about r and r'.

*Between two transitions, those labeled with the same alphabet (*a*–*d*) are possible to be related.

†It is located at the boundary of the observed area, so may be part of its original feature.

others in CO 1–0 and all in CO 2–1 have a single component. Finally, eight CO 1–0, except 2*c*, and eight CO 2–1 clouds are obtained, and which are possible to associate with H I gas of the supershells in the GS064 region. The average line profiles of the two transitions have average σ_v of 2.24 km s^{-1} and 1.17 km s^{-1} with standard deviations of 0.68 km s^{-1} and 0.48 km s^{-1}, respectively. Such σ_v values are not very different from typical of the clouds having similar sizes (See the σ_v-size relationship in Figure 9a of Heyer & Dame 2015). They seem to be placed slightly below the scatter of the σ_v-size distribution, and the trend is consistent with that of the outer Galactic clouds plotted in the Figure 9a of Heyer & Dame (2015). It may mean that there is no σ_v increase which may indicate shocked or highly disrupted molecular gas. Most $M_{\rm H_2}$ values are somewhat larger than corresponding $M_{\rm vir}$ values, it implies that such clouds seem to be gravitationally bounded.

Figure 3.14 shows a plot of $M_{\rm H_2}$ versus $M_{\rm vir}$ of eight CO 1–0 clouds with CO 1–0 clouds observed in the Carinal Flare supershell (GSH $287+04-07$) by Dawson et al. (2008a) for comparison. Since Dawson et al. (2008a) used a slightly lower value of X, we adjusted by multiplying 1.28 to their $M_{\rm H_2}$. We obtained that $M_{\rm H_2}$–$M_{\rm vir}$ distributions can be presented as $log(M_{\rm H_2}) = 0.83\,log(M_{\rm vir}) + 1.27$ for Dawson's and $log(M_{\rm H_2}) = 0.77\,log(M_{\rm vir}) + 0.82$ for ours by Robust bisector fits. The slope of our CO 1–0 clouds in the GS064 region has a slightly shallower slope than that of Dawson's, and the fitting line of ours is shifted down about a half unit comparing that of Dawson's. Such differences may be caused by CO clouds in the GS064 region are more evolved. Two supershells in the GS064 region have about 3–4 times larger sizes. Their ages are roughly 4.5×10^7 and 5.3×10^7 yr respectively assuming a stationary shell has an age comparable to its sound crossing time with a typical sound speed of ~ 10 km s^{-1} in the warm neutral medium, while GSH $287+04-07$ has an age of $\sim 10^7$ yr (Dawson et al. 2008b). Since CO clouds are associated with each shell, the fact that the supershells in the GS064 region are older than

GSH 287 + 04 − 07 is likely to support the conditions. On the other hand, most of CO 2–1 clouds are likely to belong to poorly resolved CO 1–0 clouds based on their locations and central velocities. This fact may imply that CO 1–0 clouds can be divided into several fragmented smaller clouds in higher resolution observations.

Interestingly, there are four *WISE* H II regions having $v_{\rm LSR} < -65$ km s^{-1} in the GS064 region shown in the top image of Figure 3.13: G62.578 + 2.389 at -73.6 km s^{-1}, G61.432 + 2.082 at -71.7 km s^{-1}, G61.668 + 0.947 at -78.8 km s^{-1}, and G61.721 + 0.863 at -75.2 km s^{-1}. It would not be a coincidence that such a small number of H II regions are seen in shell walls in a large space of the GS064 region. Also, they appear near or within some of the CO clouds above, but their velocities are slightly shifted from those of the clouds. The H II regions seem not to be embedded within the CO clouds, but their association may not rule out.

Figure 3.15 shows 2D-distribution of properties of CO 2–1 clouds in two subregions. From top to bottom panels are $W_{\rm CO\,2-1}$, v_0, and σ_v for pixels having integrated intensities over $(-77, -62)$ km s^{-1} larger than 1.7 K km s^{-1}. When seeing CO 2–1 clouds in the left panels (2–3 listed in Table 3.4), there are gradients in v_0 and σ_v from the west to the east, i.e., v_0 are shifted toward lower negative velocities, and σ_v becomes smaller overall. In the west, there is GS063.6+01.0−71, and expansion of the supershell may cause such phenomena. In right panels, CO 2–1 clouds 6–7 and another cloud not listed in Table 3.4 are presented. The two CO 2–1 clouds have no gradient in v_0 and σ_v while most σ_v values are similar to most western part of CO 2–1 cloud 2. Two *WISE* H II regions are located just outside of CO 2–1 cloud 7 at somewhat higher negative velocities shown in the middle right panel.

H I gas features along supershell walls are very complicated, so it is hard to extract and examine an isolated H I cloud. However, we analyze one H I cloud probably associated with CO 1–0 cloud 3a and CO 2–1 clouds 6–7 in a box region at $(l,\ b) = (61.^\circ65,\ +1.^\circ15)$ with $(\Delta l,\ \Delta b) = (0.^\circ26,\ 0.^\circ45)$. H I emission

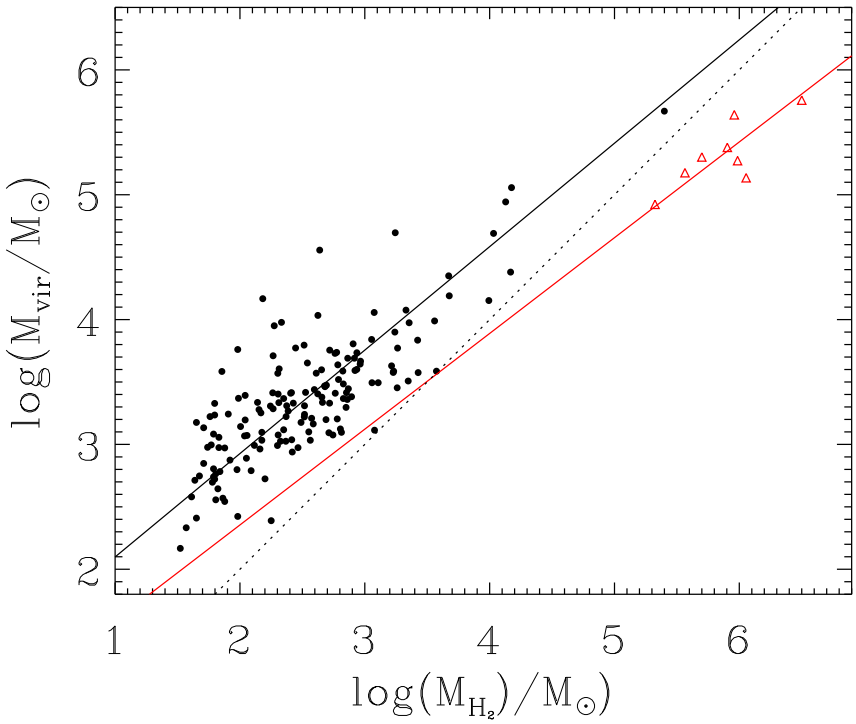

Figure 3.14. Plots of $M_{\rm H_2}$ versus $M_{\rm vir}$ for CO 1–0 clouds in the GS064 region (red triangles) and those in the Carina Flare supershell observed by Dawson et al. (2008a) (black dots). Red and black solid lines are robust bisector fits for each set of data points. Black dotted line indicates where $M_{\rm H_2}$ is equal to $M_{\rm vir}$.

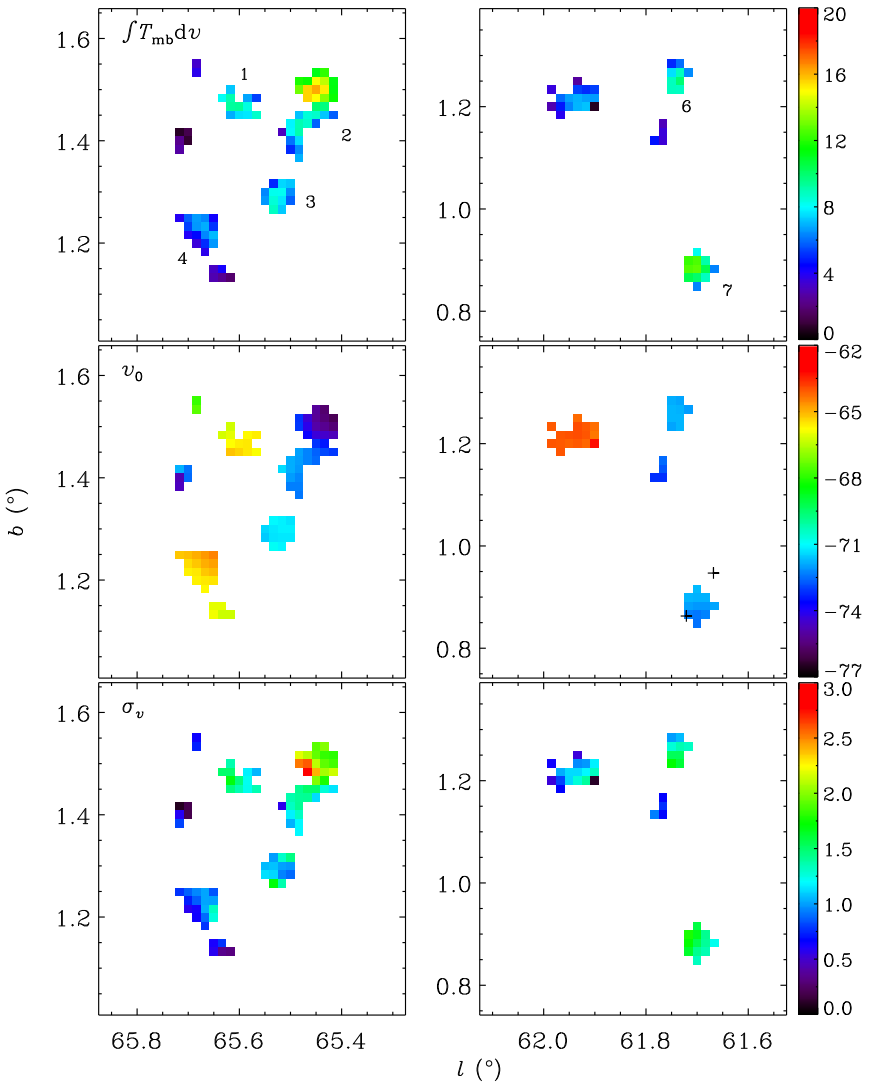

Figure 3.15. Properties of ^{12}CO $J = 2 - 1$ line profiles in two GS064 sub-regions. Integrated intensity ($\int T_{\rm mb} dv$ in K km s^{-1}; top), central velocity (v_0 in km s^{-1}; middle), and velocity dispersion (σ_v in km s^{-1}; bottom) are derived by fitting a single Gaussian curve to each line profile. The fit is limited to positions where integrated intensity over (-77, -62) km s^{-1} is larger or equal than 1.7 K km s^{-1}. The cloud numbers are marked in the upper panels. Black crosses in the middle right panel mark locations of *WISE* H II regions having higher negative velocities than a neighboring CO cloud.

in the selected region at the velocity range where the two supershells and CO clouds are visible is almost filled with H I gas in the walls since it is where the supershells seem to be interfaced. Figure 3.16 shows a slightly larger view of the selected region with CO emission contours and two *WISE* H II regions. CO emission features are not on where H I emission is brightest, but against a bright subfilamentary H I structure. We obtained an average H I line profile from the subregion mentioned above, and then applied the Gaussian fit to it. The CO 1–0 and CO 2–1 clouds are at about $-72 - -73$ km s^{-1}. A decomposed Gaussian H I component having a similar central velocity of the CO clouds gives Gaussian parameters of $T_{\rm b,pk} = 48.00$ K, $v_0 = -73.42$ km s^{-1}, and $\sigma_v = 3.40$ km s^{-1}. Figure 3.17 shows the average H I line profile and decomposed Gaussian components with a thicker line for what is associated with H I shell walls. The heliocentric distance corresponding to the v_0 value is 16.1 kpc. H I column density can be derived using the equation, $N({\rm H\,I}) = -1.82 \times 10^{18}\, T_{\rm s} \int_{-\infty}^{\infty} \ln[1 - T_{\rm b}(v)/T_{\rm s}]\, {\rm d}v$, where $T_{\rm s}$ is spin temperature assuming as 125 K (Wilson et al. 2013), and we obtained that $N({\rm H\,I}) = 8.74 \times 10^{20}$ cm^{-2}. H I mass is inferred as $2.57 \times 10^5\ M_\odot$. According to previous studies, the formation of H_2 starts at where total gas column density is larger than $3 - 5 \times 10^{20}\,{\rm cm}^{-2}$ (e.g., Savage et al. 1977; Gillmon et al. 2006), and H_2 gas exists at where $N({\rm H\,I}) \gtrsim 5 - 10 \times 10^{20}\,{\rm cm}^{-2}$ (e.g., Reach et al. 1994; Barriault et al. 2010; Liszt 2014). It is likely that this H I cloud coincides to such expectation.

The GS064 region is an intriguing place located in the outer Galaxy ($R_{\rm Gal} \sim$ 14 kpc). It contains H I supershells, molecular clouds, and H II regions, and spatial coincidence implies that they are likely to be associated with each other. So, this place is worth studying in more detail to understand the supershell-driven molecular formation and triggered star formation.

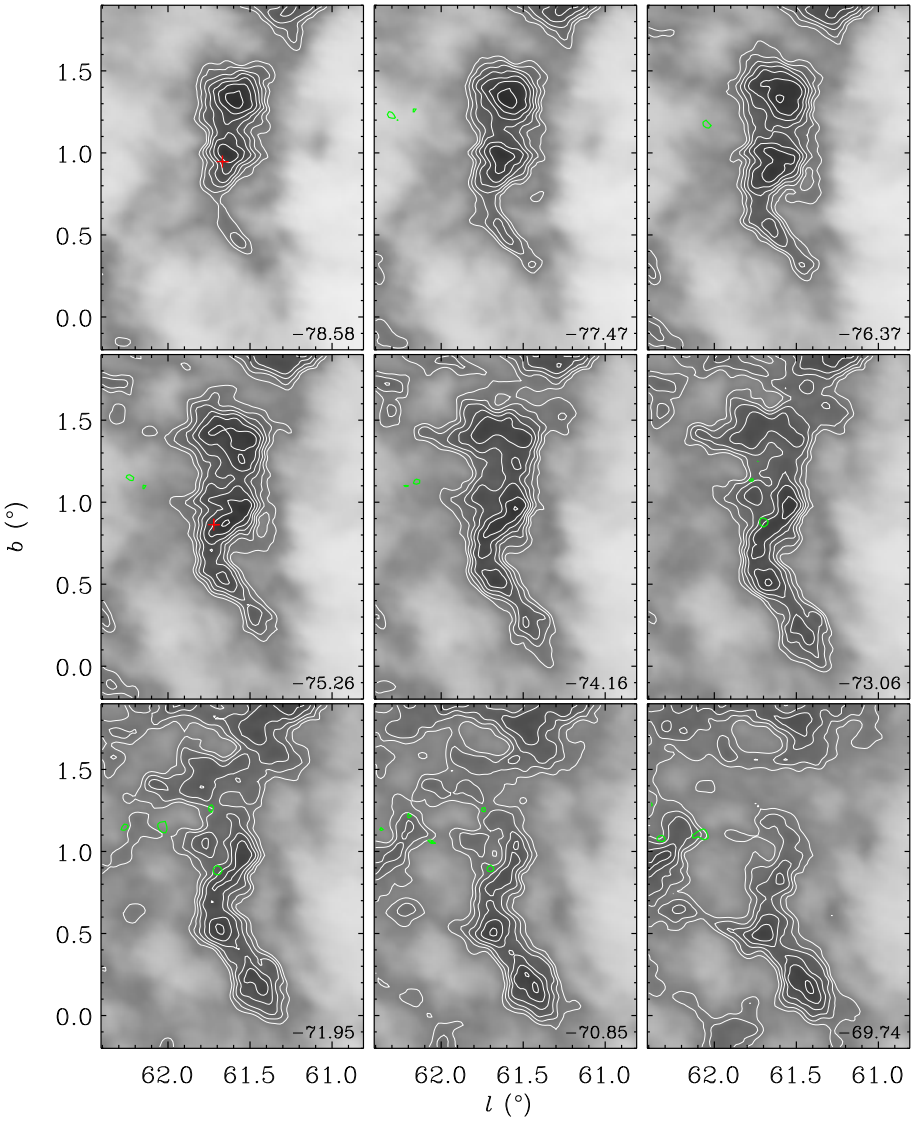

Figure 3.16. H I channel maps with CO contours for the western part of the GS064 region. The central velocity of each map is written in the lower right corner, and the channel width is 1.1 km s^{-1}. The inverted gray scale ranges from 0 K (white) to 100 K (black). White contours are same as gray images, and levels are 50, 55, 60, 65, 70, 75, 80 K. Green contour is ^{12}CO $J = 2 - 1$ emission with a level of 2 K. Red crosses shows locations of *WISE* H II regions.

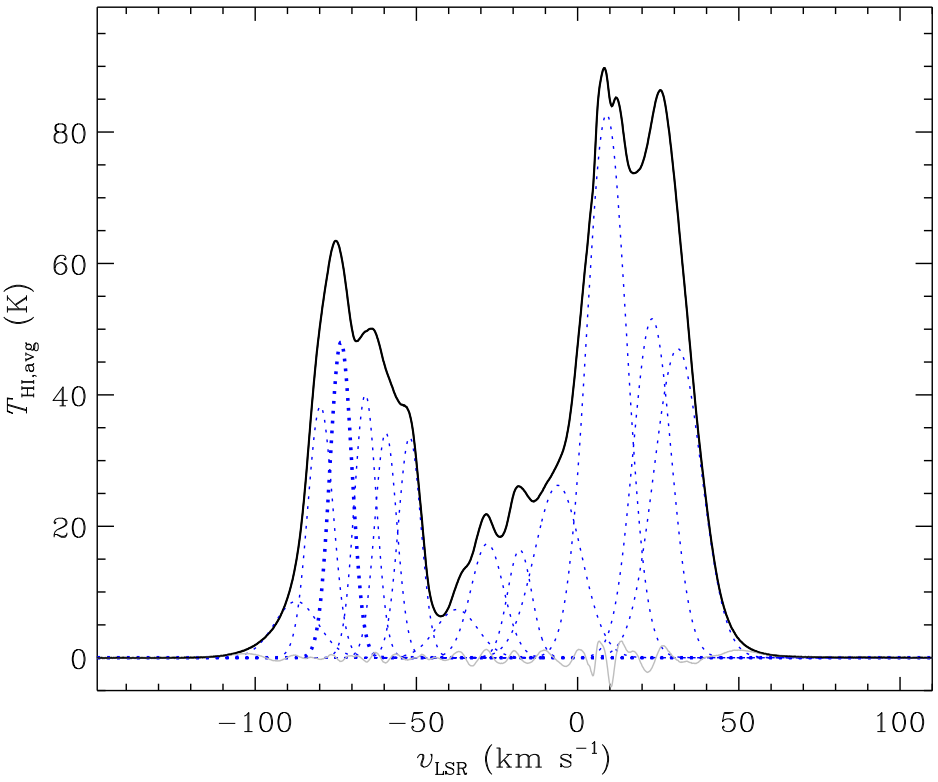

Figure 3.17. H I average line profile obtained from the western part of the GS064 region showing CO emission. Blue dotted curves show decomposed components by fitting multiple Gaussian curves, and a solid gray line is residual. The blue thick dotted curve indicates which has a similar velocity of CO line. A detailed description is in Section 3.8.2.

3.9 Summary

H I shells/supershells have been studied by many previous researchers mostly using low or moderate-resolution H I survey data, but there was somewhat limited to study on their detailed structures. The I-GALFA H I survey was done in $\ell \approx 32^\circ$ to 77° and $b \approx -10^\circ$ to $+10^\circ$ and achieved the high resolution ($4'$) and high sensitivity (0.2 K) of the H I data. This survey data provide an opportunity to investigate H I shells/supershells from small to large scales. In the survey area, we verified known objects cataloged by Heiles (1979) with low-resolution ($36'$) data and searched new shell candidates. And then, we examined their properties to understand the true nature of the objects found. The main results are summarized as follows.

1. We listed the total of 38 H I shells/supershells in the survey area. We confirmed that 13 of 20 shells identified by Heiles (1979) are reliable. Six of the remainder are ambiguous shell-like structures, which seem to be transient filaments, and one is invisible in the I-GALFA survey data. On the other hand, we found new 25 shell candidates in the survey area. For all shells/supershells listed in this paper, the geometric mean diameter and velocity extent, where a shell is visible, range about 1°–13° and 7–65 km s^{-1} with an average of $4.^\circ6$ and 18 km s^{-1}, respectively. Some of them, mostly in the inner Galaxy, are complicated with other chimney or more than one shell, and some might be located near active star-forming region(s).

2. We estimated distance, linear diameter, and initial explosion energy ($E_{\rm E}$) (Table 3.3). Fourteen and twenty-four shells are located in the inner and outer Galaxies, respectively, and at the given distances, they have the geometric mean diameters between 50 pc and 4 kpc. Fifteen of them need an enormous initial energy of $E_{\rm E} \geq 3 \times 10^{52}$ erg.

3. We compared Galactocentric radius distribution of H I shells/supershells to those of H II regions and GMCs since they are likely to have possible energy sources to produce a shell/supershell (Figure 3.12). All H II regions, obtained from the *WISE*

catalog (Anderson et al. 2014), in the I-GALFA area are mainly distributed in the inner Galaxy and concentrated on about 4–8 kpc. However, a non-negligible number of H II regions are distributed in the outer Galaxy. The distribution of GMCs show a similar trend with one of *WISE* H II regions. Meanwhile, I-GALFA H I supershells are mostly located in the outer Galaxy, and a few are in the inner Galaxy. The comparison results imply that many inner Galactic H I supershells are missing in our survey because they are shaped like "worms." Indeed, the diagram including the Galactic worm catalog of Koo et al. (1992) presents that such structures could replace missing inner Galactic supershells. On the other hand, stellar activities such as stellar winds and multiple SN explosions are very likely to form shells, but some shells, especially located at very far distances ($R_{\rm Gal} \geq 15$ kpc), seem unlikely. Also, there is no selected GMC at such far distances. We speculate that they could be formed by HVC collisions. Most of them show no association of HVC emission features, but the possibility could not be ruled out.

4. We examined CfA CO 1–0 data (FWHM = $8\farcm4$) to check whether our shells are associated with molecular clouds, and gave a brief description of the results (Table C.1). Also, we investigated in detail molecular clouds in walls of two supershells (GS060.2+01.1−74 and GS063.6+01.0−71) in the outer Galaxy by using CO 2–1 data (FWHM $\sim 3'$) additionally. Several molecular clouds are observed near the shell walls and marginally resolved in both CO transitions. The found molecular clouds have velocity dispersions close to typical values of clouds with similar sizes and masses of $\sim 10^5$–$10^6\,M_\odot$. Moreover, in one part of shell walls where molecular clouds are observed, an H I component related with was decomposed to calculate H I column density, and the value is large enough to retain molecular gas. However, our analysis is limited, since the spatial resolution of the CO 1–0 data is poor or the spatial coverage of the CO 2–1 data is not enough. So, we expect that further study can give a better understanding of molecular clouds found in the shells.

Chapter 4

Discovery of an H I Supershell Formed by HVC Impact[1]

4.1 Abstract

H I gas in interstellar space is largely organized into filaments, loops, and shells, the most prominent of which are "supershells". These gigantic structures requiring $\gtrsim 3\times 10^{52}$ erg to form are generally thought to be produced by either the explosion of multiple SNe in OB associations or alternatively by the impact of HVCs falling to the Galactic disk. Here we report the detection of a kpc-size supershell in the outskirts of the Milky Way with the compact HVC 040+01−282 (hereafter CHVC040) at its geometrical center using the I-GALFA H I 21-cm survey data. The morphological and physical properties of both objects suggest that CHVC040, which is either a fragment of a nearby disrupted galaxy or a cloud originated from an intergalactic

[1] Most of the contents in this chapter were written as a separate paper: Geumsook Park, Bon-Chul Koo, Ji-hyun Kang, Steven J. Gibson, J. E. G. Peek, Kevin A. Douglas, Eric J. Korpela, and Carl E. Heiles, "A High-Velocity Cloud Impact Forming a Supershell in the Milky Way," 2016, ApJ, 827, L27

accreting flow, collided with the disk ~ 4.3 Myrs ago to form the supershell. Our result shows that some compact HVCs can survive their trip through the Galactic halo and inject energy and momentum into the Milky Way disk.

4.2 Introduction

Supershells are large gaseous shells of radius greater than a few hundred parsecs. They are distinct from other shell-like structures in their extraordinarily large energy requirement, i.e., $\gtrsim 3 \times 10^{52}$ erg, which corresponds to $\gtrsim 30$ SN explosions (Heiles 1979, 1984; McClure-Griffiths et al. 2002). About twenty supershells have been found in the Milky Way, and numerous H I holes corresponding to supershells have been discovered in nearby dwarfs and spiral galaxies (Kamphuis et al. 1991; Bagetakos et al. 2011). These gigantic structures are generally thought to arise from multiple SN explosions in stellar OB associations. But most supershells are missing a stellar association in their interior, and the number of supershells and their energies are usually incompatible with the level of star formation in those galaxies (Heiles 1984; Rhode et al. 1999). Therefore, several alternative scenarios have been proposed, the most popular of which is the collision of HVCs with the disk (Tenorio-Tagle 1980; Tenorio-Tagle et al. 1987; Mirabel & Morras 1990).

HVCs are H I clouds with radial velocities very different from the disk material in the Milky Way, e.g., with a deviation more than 50 km s^{-1} from the range of permitted velocities in a simple model of the distribution and rotation of the H I gas in the Galaxy (Wakker 1991). Some large HVC complexes are known to be gas streams tidally stripped from satellite galaxies of the Milky Way, but the origin of isolated CHVCs remain controversial: they could be clouds formed from galactic fountain or intergalactic accreting flows, part of the large HVC complexes, or condensations in the multi-phase circumgalactic medium (Putman et al. 2011; Wakker 2004; Putman et al. 2012). The HVC origin has been proposed for a few supershells

(Heiles 1984; Mirabel & Morras 1990; Tamanaha 1997), but there has been no clear example showing a direct link between the two, particularly for CHVCs.

Here we report the detection of a Galactic supershell with an associated HVC, GS040.2+00.6−70 (hereafter GS040). GS040 was first identified as a faint, forbidden-velocity wing feature (FVW 40.0+0.5) in the low-resolution, large-scale longitude-velocity study of Kang & Koo (2007). We have found that GS040 appears to be a complete circular ring with complicated structures inside in our high-resolution I-GALFA H I 21-cm line survey data. The I-GALFA survey is a survey of the first Galactic quadrant visible to Arecibo ($\ell = 32^\circ$ to 77° and $|b| \lesssim 15^\circ$) done by using the 7-beam ALFA receiver on the Arecibo 305 m telescope, and it provides sensitive ($\Delta T_b = 0.2$ K) and fully-sampled H I maps at spatial and spectral resolutions of $4'$ and 0.184 km s^{-1}, respectively (Koo et al. 2010; Gibson et al. 2012). The I-GALFA survey data further reveal that there is a CHVC at the very center of GS040. This CHVC, named HVC040+01−282 (hereafter CHVC040), was first identified in the Leiden/Dwingeloo survey (Wakker & van Woerden 1991) and was later classified as an isolated CHVC by Braun & Burton (1999) and de Heij et al. (2002). Westmeier et al. (2005) presented a higher-resolution ($9'$) H I image obtained from the Effelsberg telescope, which showed that CHVC040 has a pronounced head-tail structure. Our Arecibo H I images reveal detailed spatial and velocity structure of CHVC040 strongly suggesting its association with the supershell GS040. We describe two structures in Section 4.3, and discuss their physical characteristics and their association together with some implications on the disruption of HVCs in Section 4.4. Section 4.5 summarizes this work.

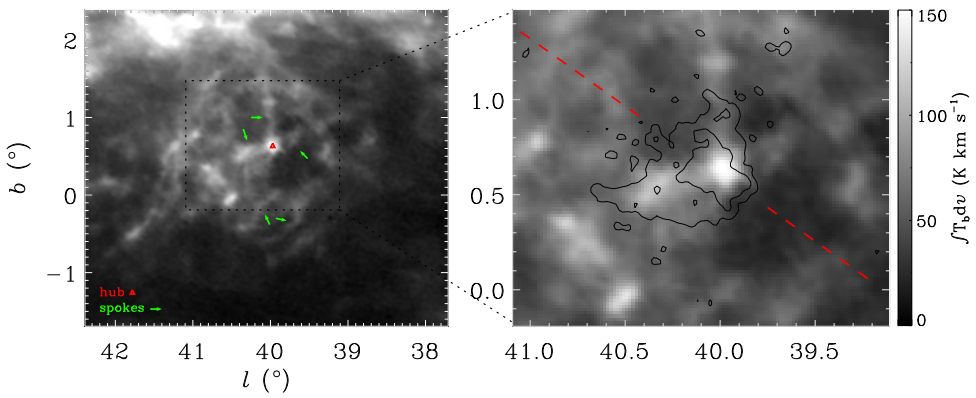

Figure 4.1. H I integrated-intensity maps of the overall picture of the supershell GS040 (left) and a close-up view inside its ring structure (right). The maps are obtained by integrating the emission between $v_{\rm LSR} = -141$ and -66 km s^{-1}. The features described in Sec. 4.3 are labeled in the left image. The overlaid contours in the right image show the overall appearance of the high-velocity cloud CHVC040 in integrated H I emission (see Figure 4.4). The position-velocity diagram in Figure 4.3 was obtained along the dashed red line.

4.3 Supershell GS040.2+00.6−70 and High-Velocity Cloud HVC040+01−282

The supershell GS040 is centered at $(\ell, b) = (40\overset{\circ}{.}2, +0\overset{\circ}{.}6)$ and clearly visible from $v_{\rm LSR} \sim -120$ to -70 km s^{-1}. In an integrated intensity map (Figure 4.1), GS040 appears as a complete circular ring of radius $\sim 1\overset{\circ}{.}3$ with complicated structures inside. More detailed structures can be seen in Figure 4.2, which presents velocity channel maps. At the most negative velocities (~ -120 km s^{-1}), we see diffuse emission with embedded knotty filaments near the center and an extended filament in the south. The features are observable at even more negative velocities (-150 km s$^{-1} < v_{\rm LSR} < -120$ km s^{-1}) but they are extremely weak and hard to detect in velocity-channel maps. As the velocity increases ($v_{\rm LSR} \gtrsim -90$ km s^{-1}), the nebulosity fades out, and a larger ($\sim 2\overset{\circ}{.}6$) ring structure appears, which resembles a cartwheel with a bright central "hub" and several "spokes" (see also Figure 4.1). The size of the ring increases slightly with velocity indicating that the ring structure is an approaching portion of an expanding shell. At velocities greater than about -70 km s^{-1}, the Galactic background H I emission becomes dominant, and the emission associated with GS040 is less clear.

At the very center of GS040 is the HVC CHVC040. The positional coincidence of CHVC040 with the GS040's central hub is striking as can be seen in Figure 4.3, which is the position-velocity map crossing the center of GS040. The morphological agreement between the two is also noticeable. Our high-resolution Arecibo H I image reveals that CHVC040 has a blunt cone shape with a steep southwestern boundary and a faint envelope flaring out northeast (Figure 4.4). This morphology of CHVC040 matches well with that of the central hub of GS040, e.g., see Figure 4.1 and also the channel map at -88 km s^{-1} in Figure 4.2.

Figure 4.4 shows the detailed spatial and velocity structures of CHVC040. The

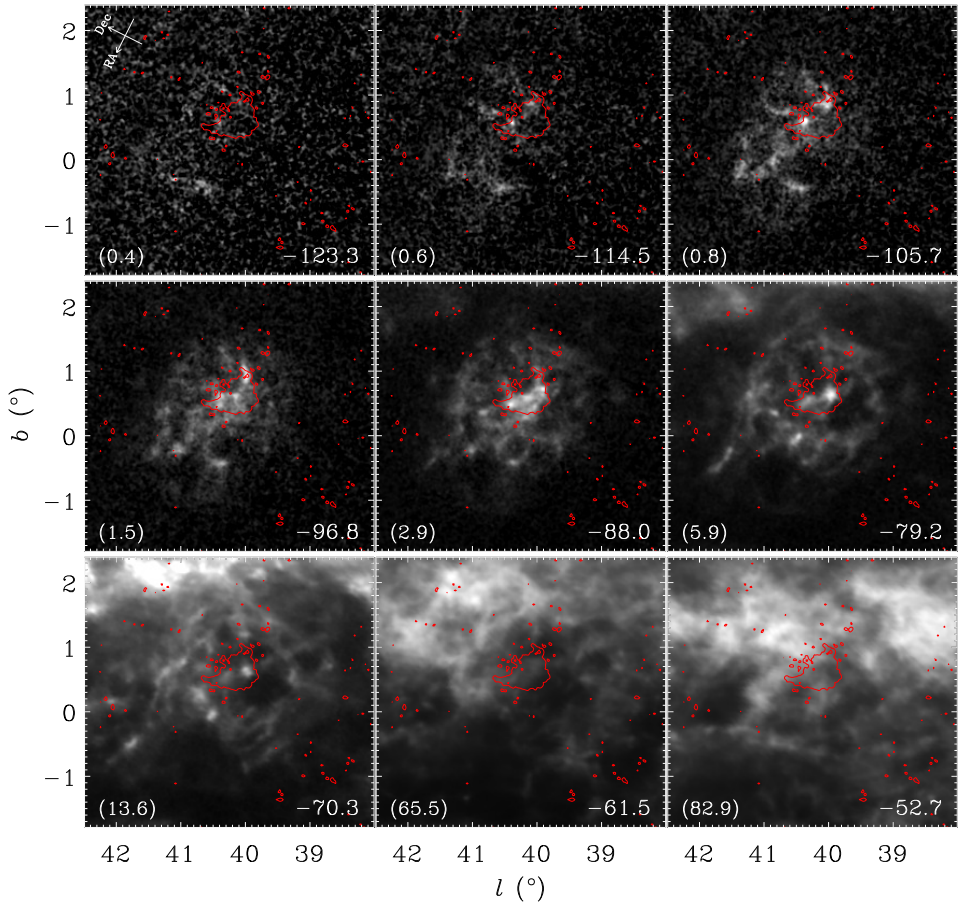

Figure 4.2. Velocity-channel maps of GS040 in the H I data. The central LSR velocity of each channel is written at the bottom right corner in km s^{-1}. The channel width and interval are 3.68 and 5.15 km s^{-1}, respectively. The H I brightness temperature in gray scale ranges from 0 K (black) to the value (white) in parentheses at the bottom left corner of each panel in Kelvins. Contours show the overall appearance of CHVC040 in integrated H I emission (see Figure 4.4). To aid comparison to literature studies in Equatorial coordinates, arrows are shown in the first panel indicating Right Ascension and Declination (J2000) coordinate directions.

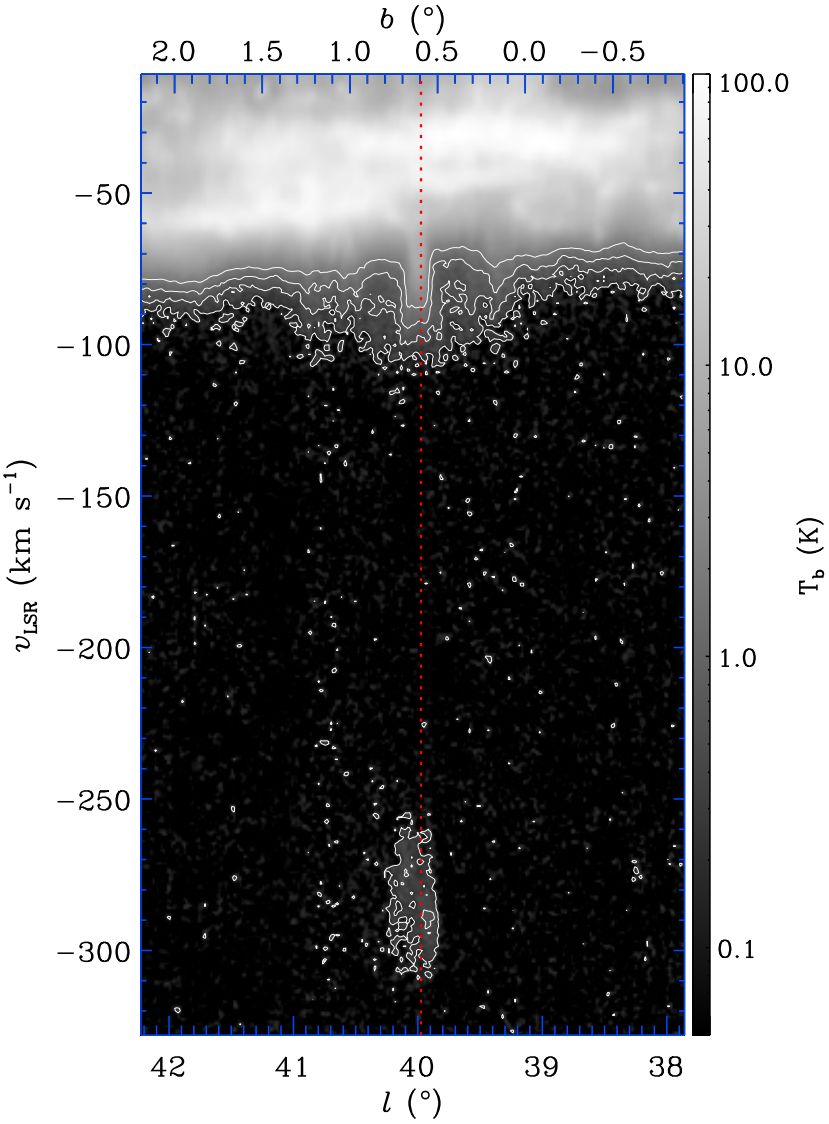

Figure 4.3. Position-velocity map of H I emission of GS040 and CHVC040. This diagram is drawn along a line crossing the center of GS040 at position angle of about 35° (Figure 4.1). The lower and upper x-axis indicate ℓ and b coordinates of the position, respectively. The y-axis indicates the LSR velocity. The contour levels are 0.2, 0.5, 1, and 2 K in brightness temperature. The dotted vertical line is toward the center of GS040.

integrated intensity map in the left frame shows that CHVC040 has a bright, $\sim 12' \times 15'$- sized "core" elongated along the northeast-southwest direction. The core appears to be composed of several clumps with a sharp boundary at southwest, whereas the diffuse envelope appears to be slightly more extended toward southeast. The mean H I column density, assuming that the emission is optically thin, is $1.5\times\ 10^{19}\,\mathrm{cm}^{-2}$ while the peak H I column density is about two times higher. The velocity centroid map in the middle frame shows that systemic velocity attains its most negative ($\lesssim -290$ km s^{-1}) at the southwestern boundary and most positive (~ -260 km s^{-1}) along the southeastern boundary and also in the middle of the northwestern boundary. The mean systemic velocity is -282 km s^{-1}. If the most positive feature in the northwestern boundary were not present, the velocity structure could have been suggestive of a rotation with respect to the northeast-southwest symmetry axis at speed of $\lesssim 20$ km s^{-1}. The velocity width (FWHM) ranges 25–45 km s^{-1} over most parts of the cloud with a median of 36 km s^{-1}. The southwesternmost thin layer has relatively narrow width ($\sim$19–28 km s^{-1}) while parts of the northern area has width $\gtrsim 50$ km s^{-1}. The region with the narrowest line width is very thin ($\sim 3'$), and therefore Westmeier et al. (2005) could not spatially resolve it.

Some representative line profiles are shown in Figure 4.5 together with the average line profile of the cloud. Most profiles are well described with a single Gaussian component, while some profiles, e.g., c and e-g, show clear double peaks or a narrow component superposed on a broad component. The velocity width of the mean profile is 45 km s^{-1}, which is considerably larger than the median value (36 km s^{-1}) of individual profiles, presumably due to the dispersion of central velocities. The median width corresponds to a kinetic temperature of 2.8×10^4 K. At several positions, narrow velocity components are detected, but still their widths are ≥ 10 km s^{-1}, which implies a kinetic temperature $\geq$ 2,000 K. This indicates that CHVC040 is mostly composed of warm neutral gas, which is not unusual for CHVCs (Winkel et

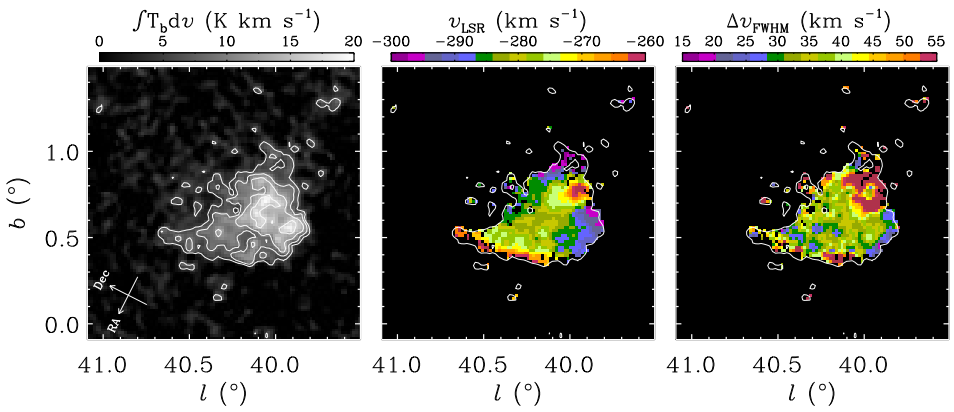

Figure 4.4. Spatial and velocity structures of the high-velocity cloud CHVC040. Left: H I intensity map integrated over LSR velocities from −330 to −230 km s^{-1}. Contours are drawn at 5, 8, 12, and 16 K km s^{-1}. If the emission is optically thin, 1 K km s^{-1} corresponds to hydrogen columns of 1.82×10^{18} cm^{-2}. Middle and Right: Central velocity and velocity width maps derived by fitting single Gaussian curve to each line profile. The fit is limited to positions with integrated intensity greater than 5 K km s^{-1}, i.e., within the white contour. The pixels where the emission is weak and a reasonable fit cannot be obtained are also blanked out. To aid comparison to literature studies in Equatorial coordinates, arrows are shown in the left panel indicating Right Ascension and Declination (J2000) coordinate directions.

al. 2011; Faridani et al. 2014). But it is different from those head-tail HVCs with a narrow-line head of undisturbed cold H I gas and a wide-line tail of disturbed warm H I gas (e.g., HVC125+41−207; Brüns et al. 2001).

4.4 Discussion

4.4.1 Formation of GS040 by the Collision of CHVC040

The location of CHVC040 at the geometrical center of GS040 suggests that their physical association is very likely. The centroids of the CHVC emission and that of the GS040's hub emission overlap within ~ 0.2 degrees. The probability of this being a random alignment is $\sim 3 \times 10^{-6}$, and multiplying this by ~ 300 CHVCs yields an overall probability of 9×10^{-4} for any CHVC aligning this well with the GS040's hub. No intermediate-velocity H I connecting the two is apparent (Figure 4.3), but this could be because the gas is ionized. We searched for a warm ionized gas associated with GS040 using the Wisconsin Hα Mapper Northern Sky Survey (WHAM-NSS) data (Haffner et al. 2003). The survey has an angular resolution of 1°, and, around the GS040 area, it provides Hα spectra covering $v_{\rm LSR}$ from -85 to $+100$ km s^{-1} at spectral resolutions of 12 km s^{-1}. We have examined the Hα intensity map integrated over the velocity range of GS040 (-85 to -66 km s^{-1}), but could not detect an associated emission ($\lesssim$ 0.05 R where $1R = 10^6/4\pi$ photons cm^{-2} sr^{-1} s^{-1}). Note that this area is bright in the total Hα intensity map with a mean intensity of about 3 R, so that we do not expect to see the faint emission associated with either GS040 or CHVC040 in the all-sky Hα maps (Finkbeiner 2003; Dennison et al. 1998). We also searched for an associated hot ionized gas using the 0.1-2.4 keV image of the ROSAT All-Sky X-ray Survey (1 pixel scale = 44″; Voges et al. 1999), but couldn't detect any emission.

CHVC040 belongs to the "Galactic Center Negative" (GCN) HVC complex,

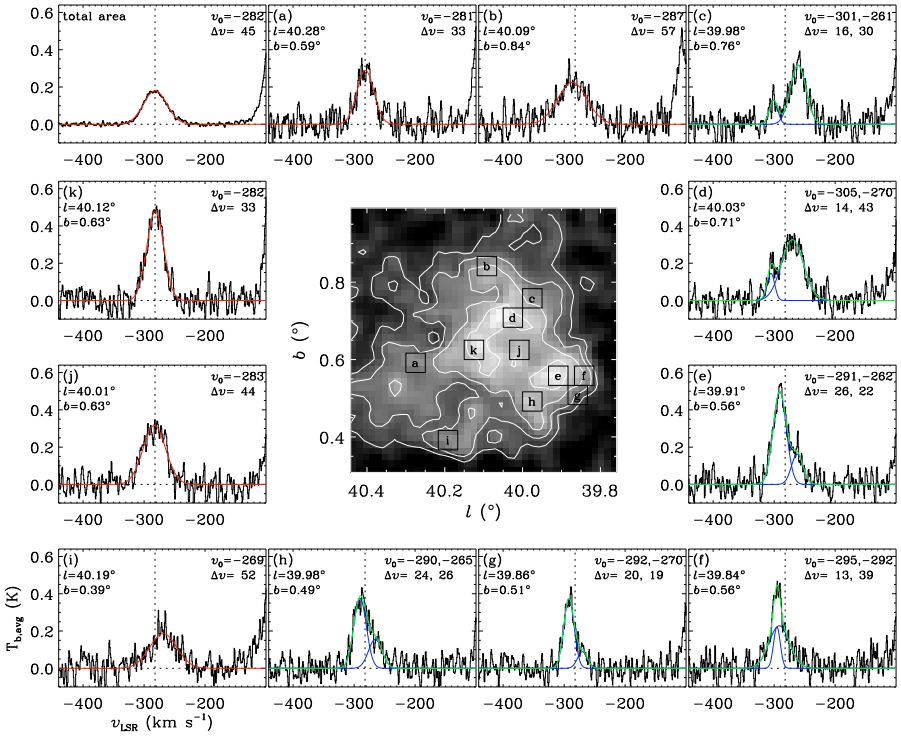

Figure 4.5. Examples of CHVC040 H I line profiles. The profile in the top left frame is an average profile of the whole cloud. The rest of line profiles are extracted from the areas marked by boxes in the central image, which is the integrated intensity map in Figure 4.4. The profiles have been Hanning smoothed to have a velocity resolution of 2.96 km s^{-1}. A Gaussian fit with the suitable number (n) of components is applied and displayed with a red (n=1) or green curve (n=2; each in a blue line). Resultant parameters, including central LSR velocity (v_0) and velocity width (Δv) in km s^{-1}, are written on the top right corner of each panel. A vertical line at the central velocity of the average line profile (-282 km s^{-1}) is drawn to aid the intercomparison of different plots.

which is a collection of small discrete HVCs sparsely distributed over a $70^\circ \times 70^\circ$ area within $\ell = 0^\circ$ to 70° and $b = -60^\circ$ to 10° (Wakker & van Woerden 1991; Winkel et al. 2011). A kinematic model has been proposed where GCN is a smooth gas flow starting at $b = -60^\circ$ at a heliocentric distance of 35 kpc and crossing the Galactic plane obliquely at 15 kpc (Jin 2010). For comparison, GS040 is probably located near the Sct-Cen arm at a distance of ~ 20 kpc (Dame & Thaddeus 2011) because the disrupted ISM is seen only at velocities below that of the Sct-Cen arm (~ -60 km s^{-1}), not at higher velocities (see Figures 4.2 and 4.3). We examined lists of known stellar objects, H II regions, OB stars, and SNRs, but no known sources are likely to be associated with GS040. There is one H II region (G039.864 + 00.645) in the *WISE* catalog of Galactic H II regions (Anderson et al. 2014) that is located at $\sim 6'$ west of the hub. But this H II region has a systemic velocity of -40.9 km s^{-1} (Anderson et al. 2011) and is enclosed by a small ($68''$) dust shell, so it cannot be responsible for the HI shell. Instead the distance of ~ 20 kpc is not unreasonable for CHVC040, because GCN does not have a smooth extended envelope like other HVC complexes, and it appears to be composed of several subpopulations that do not share a common origin (Winkel et al. 2011). Note that the geometrical center of GS040 is well below the Galactic plane ($\sim 420\, d_{20}$ pc where $d_{20} \equiv d/20$ kpc), i.e., at $b = +0.^\circ 6$ while the midplane there is at $b \sim +1.^\circ 8$ because the Galactic plane is warped in the outer Galaxy (Levine et al. 2006). It is difficult to imagine the SN origin for a supershell at such height, and CHVC040 is most likely the energy/momentum source for GS040.

The total energy deposited in the Galactic disk by CHVC040 can be inferred from the parameters of the GS040 supershell. The radius of GS040 is $450\, d_{20}$ pc, while its mass at $v_{\rm LSR} \leq -75$ km s^{-1} is $1.6 \times 10^5\, d_{20}^2 M_\odot$ including the cosmic abundance of helium. If we account for the mass unobservable due to Galactic background H I emission, the total mass of GS040 would be considerably greater.

Adopting $v_{\rm exp} \sim 30$ km s^{-1} as the expansion speed of the shell, its kinetic energy is $E_{\rm K} \gtrsim 1.4 \times 10^{51}\, d_{20}^2$ erg. The collision should have occurred $\sim 0.29 R_{\rm sh}/v_{\rm exp} \sim 4.3 \times 10^6\, d_{20}$ yrs ago, where the numerical factor 0.29 accounts for the deceleration of the shell (Cioffi et al. 1988). Note that $E_{\rm K}$ is a small fraction of the total energy deposited ($E_{\rm E}$), most of which should have been radiated away. If GS040 was produced by multiple SNe, then, assuming instantaneous energy injection (Heiles 1979), $E_{\rm E} \sim 5.3 \times 10^{43}\, n_0^{1.12}\, R_{\rm sh}^{3.12}\, v_{\rm exp}^{1.4} \sim 1.2 \times 10^{53}\, (n_0/0.1\ {\rm cm}^{-3})$ erg, where n_0 is ambient hydrogen density. At the position of GS040, the mean H I density in the midplane is $\sim 0.1\, {\rm cm}^{-3}$, and the H I scale height is about 720 pc (Levine et al. 2006). So $n_0 \sim 0.06$ cm^{-3}, and we have $E_{\rm E} \sim 7 \times 10^{52}$ erg. For comparison, the total extent of CHVC040 is $210\, d_{20} \times 320\, d_{20}$ pc^2 while its H I mass is $M_{\rm CHVC} = 5{,}800\, d_{20}^2 M_\odot$. The area used to derive this mass has a geometrical mean radius of 150 pc, so that the mean hydrogen density of CHVC040 is 0.017 cm^{-3}. If CHVC040 collided with the rotating disk with the mean 'deviation' speed (absolute difference in velocity from the disk gas there) of HVCs, i.e., ~ 240 km s^{-1} (Wakker 2004), the kinetic energy and momentum would be $4.7 \times 10^{51}\, d_{20}^2$ ergs and $2.0 \times 10^6\, d_{20}^2 M_\odot$km s^{-1} including the He abundance, respectively. This implies that the mass of CHVC040 when it collided with the disk should have been an order of magnitude greater and that the HVC that we see (CHVC040) might be the remains of the original HVC.

The spatial morphology and velocity structure of CHVC040 suggest that it is moving southwest in the plane of the sky and is approaching us. The steep southwestern boundary of the cloud might represent the region compressed by the interaction with the ambient medium, whereas the diffuse envelope might be the material stripped off from the cloud due to the interaction or by the ram pressure of the surrounding medium (Santillán et al. 1999; Kwak et al. 2009). The small velocity width along the southwestern boundary and large velocity width beyond appear to be consistent with such speculation. Recently, Heitsch et al. (2016) suggested that,

for a CHVC with head-tail structure, the inclination angle, i.e., the angle between the CHVC's trajectory and the line-of-sight, can be derived from the asymmetry in position-velocity diagram along the head-tail line crossing the center of mass. The morphology of CHVC040 is different from typical head-tail CHVCs, i.e., CHVC040 has a wide flaring 'tail' not a narrow elongated tail (see also Section 4.3), and its core is fragmented, so that it is not obvious if their model can be applied. Nevertheless if we assume that the center of mass is near the southwestern boundary and apply their model (their equations 1–4) to the position-velocity diagram along the red-dashed line in Figure 1, we obtain an inclination angle of $\sim 30^{\circ}$ which is consistent with our expectation.

The shape of CHVC040 appears to be pointed away from the Galactic midplane as if it already went through the midplane. But the geometrical center of the supershell coincides with the current location of CHVC040, not being located in the midplane. Perhaps CHVC040 is approaching at an angle to the warped Galactic disk and has not yet fully penetrated the disk to the midplane. It is worth to note that, according to the Jin (2010)'s model, the GCN HVC stream is colliding to the Galactic plane almost perpendicularly *from below*, while the head-tail directions of individual HVCs seem to indicate that there is no preferential direction in their motions (Winkel et al. 2011). Therefore, the orbit of CHVC040 is uncertain. The colliding geometry and the origin of the complex structures such as the hub and spokes in GS040 need to be explored.

4.4.2 CHVC040 and Disruption of HVCs

There are about three hundred known CHVCs in the Milky Way (de Heij et al. 2002; Putman et al. 2002). A considerable fraction of CHVCs has a head-tail structure indicating a ram pressure interaction with the diffuse galactic halo gas (Putman et al. 2011). An important question is whether they are totally dissipated in the

Galactic halo to feed the multi-phase circumgalactic medium or they can survive their trip through the halo (e.g., Putman et al. 2011). Since CHVC040 is located in the far outer Galaxy, it may be of extragalactic origin rather than originating from a Galactic fountain, although it is not clear whether CHVC040 was originally a fragment of a nearby tidally disrupted galaxy or a cold cloud formed in a larger accreting flow of ionized, low-metallicity intergalactic gas. Our result then directly shows that at least some CHVCs of extragalactic origin do survive and collide with the Galactic disk. According to numerical studies, CHVCs with H I masses $\lesssim 3 \times 10^4 M_\odot$ would be totally disrupted in the Galactic halo unless they are embedded in dark matter (Heitsch & Putman 2009; Plöckinger & Hensler 2012). But dynamical shielding by an extended diffuse gaseous component can significantly extend their lifetime (Putman et al. 2012). We have checked whether there are additional sources like the CHVC040-GS040 system in the I-GALFA H I data using the HVC catalog of de Heij et al. (2002). There are twelve CHVCs in their Table 2 including CHVC040 in the I-GALFA survey area, most of which are at relatively high latitudes. They are isolated HVCs and have $v_{\rm LSR} < -150$ km s^{-1}, so they belong to the GCN HVC complex. We see low-velocity H I features around some CHVCs, but none of them appear associated. A systemic study against all CHVCs may reveal other CHVC-supershell systems.

4.5 Summary

We report the detection of a kpc-size supershell (GS040) in the outskirts of the Milky Way with the compact HVC (CHVC040) at its geometrical center using the I-GALFA H I data. They were presented in previous studies (Kang & Koo 2007; Westmeier et al. 2005) with lower resolution H I data ($30'$ and $9'$, respectively), but our high-resolution Arecibo H I images reveal their detailed spatial and velocity structures. GS040 looks like a cartwheel composed of a ring structure of radius

$\sim 1.^{\circ}3$ with a bright central "hub" and several "spokes" inside, while CHVC040 show a bright elongated core (size $\sim 12' \times 15'$) surrounded by diffuse gas with a sharp boundary at the far side of the Galactic disk (Figure 4.1). The most region of CHVC040 has velocity line width of 25–45 km s^{-1}. However, the region with the narrowest line width ($\sim$ 19–18 km s^{-1}) is seen at the sharp boundary and very thin ($\sim 3'$), so Westmeier et al. (2005) could not spatially resolve it (Figure 4.4). The kinematic distance of GS040 is estimated at $\sim$ 20 kpc from the Sun and located below the Galactic plane ($\sim$ 420 pc). It is hard to imagine the SN origin for a supershell at such height, and CHVC040 is most likely the energy/momentum source for GS040. The analysis of the morphological and physical properties of the both objects suggests that CHVC040 might be the remains of the original HVC which collided with the Galactic disk $\sim$ 4.3 Myrs ago. Also, CHVC040 might be of extragalactic origin rather than originating from a Galactic fountain since it is located at the far outer Galaxy. That is, CHVC040 might be either a fragment of a nearby disrupted galaxy or a cloud originated from an intergalactic accreting flow. Our results imply that some compact HVCs can survive their journey through the Galactic halo and provide energy and momentum into the Milky Way disk.

Chapter 5

Summary

H I shells/supershells are one of the outgrowths of the most energetic physical processes in the diffuse ISM. They have been studied by many previous researchers mostly using low or moderate-resolution H I survey data, but there was somewhat limited to study on H I shells/supershells in details. The I-GALFA survey provides fully-sampled H I data covering the Galactic plane in the first Galactic quadrant between longitudes 32 to 77 degrees and latitudes -10 to $+10$ degrees. The considerable latitude range up to off-site Galactic plane is enough to examine large structures such as supershells. Furthermore, the high resolution ($4'$) and high sensitivity (0.2 K) of the data provide an opportunity to investigate small-scale, faint H I emission in the diffuse ISM. Using the I-GALFA survey data, we could have studied Galactic H I shells/supershells from small to large scales. The main results of three sub-projects presented in this thesis are summarized as follows.

First, we have investigated the I-GALFA data toward the all known 39 SNRs in the survey area to search for associated fast-expanding H I shells (Chapter 2). H I emission from the fast-expanding H I shells can be seen at high velocities without the confusion of background emission. We found that four of the 39 SNRs, G34.7$-$0.4

(W44), G49.2−0.7 (W51C), G54.4−0.3 (HC40), and G69.0+2.7 (CTB 80), show associated HV H I emission. The fact of the four SNRs is presented in the previous low-resolution (30′) H I study of KH91, but the high-resolution and high-quality I-GALFA data show that W44 has associated H I emission at both very high positive and negative velocities. This is the first detection of both sides of an expanding shell associated with an SNR in the inner Galaxy in H I line emission. Also, the high-resolution images of the SNR G54.4−0.3 present that very circularly symmetric H I emission matches very well with its radio continuum morphology, and a ring structure is seen just outside the SNR boundary which could be a pre-existing structure formed by the progenitor. We discuss the properties of the expanding H I shells in these two SNRs and derive their physical parameters. The other two SNRs have been studied previously in detail, and the I-GALFA results are consistent with those previous studies. We conclude that the four SNRs with H I shells (H I SNRs) are middle-aged SNRs which are probably the remnants of CCSNe interacting with a relatively dense medium.

On the other hand, we note that there is no detection of associated HV H I emission in any of ten SNRs newly discovered since the work of KH91. Also, one expects to detect large H I SNRs in the diffuse ISM, but they have not found. We examined the visibility or detectability of H I SNRs which depends on their location in the Galaxy. Three of the four detected H I SNRs (excluding W44) are situated at favorable locations, while many other SNRs are *not* detected in the H I 21-cm line in spite of favorable positions. Therefore, we conclude that the SNRs without H I shells could be either too young or too old to have an associated fast-expanding H I shell.

Second, we have verified known objects cataloged by Heiles (1979) with low-resolution (36′) data and searched new shell candidates (Chapter 3). Among the

twenty Heiles' shells in the survey area, thirteen are confirmed to be a shell and others are ambiguous or even not seen in the I-GALFA data. We found twenty five new shell candidates. Consequently, we listed the total of thirty-eight H I shells/supershells in the survey area. Their geometric mean diameters and velocity extents range about 1°–13° and 7–65 km s^{-1} with an average of 4.°6 and 18 km s^{-1}, respectively. Fourteen shells are located in the inner Galaxy, and twenty-four in the outer Galaxy. Our Arecibo images show that some of them, mostly in the inner Galaxy, are complicated with other chimney or more than one shell. Comparing with known massive stars or H II regions, some might be located near active star-forming region(s). We also inferred distance, linear diameter, and initial explosion energy. At the given distances, our findings have geometric mean diameters between 50 pc and 4 kpc, and fifteen of them require an enormous initial energy of $E_{\rm E} \geq 3 \times 10^{52}$ erg.

We compared the Galactocentric distribution of I-GALFA H I shells/supershells with those of H II regions and GMCs which are closely related with star forming regions. The H II regions and GMCs show a similar trend each other that most objects are distributed in the inner Galaxy and concentrated on about 4–8 kpc, although a non-negligible number of objects appear in the outer Galaxy. However, I-GALFA H I supershells does not show such a trend, that is, a few are in the inner Galaxy. These facts may imply that many inner Galactic H I supershells are missing in our shell list. One possibility to explain is that they had broken through the disk and evolved into "chimneys" or "worms." Additionally, considering Galactic worms found by Koo et al. (1992) in the inner Galaxy, the distributions are comparable. It may support the common belief that stellar activities are most likely to form H I shells/supershells. On the other hand, stellar activities such as stellar winds and multiple SN explosions are very likely to form shells, but some shells, especially located at very far distances ($R_{\rm Gal} \geq 15$ kpc), seem unlikely. Also, there is no selected GMC at such far distances. We speculate that they could be formed by

HVC collisions. Most of them show no association of HVC emission features, but the possibility could not be ruled out.

We also examined molecular clouds associated with H I shells and gave brief description of the results (Table C.1). As one of most interesting regions, we investigated molecular clouds in walls of two supershells (GS060.2+01.1−74 and GS063.6+01.0−71) in the outer Galaxy. The molecular clouds that we found have velocity dispersions close to typical values of clouds with similar sizes (Heyer & Dame 2015). Due to the sensitivity and spatial resolution of CO data, massive molecular clouds with masses of $\sim 10^5$–$10^6\,M_\odot$ are found. Moreover, in one part of shell walls where molecular clouds are observed, an H I component related with was decomposed to calculate H I column density, and the value is large enough to retain molecular gas. However, our analysis is limited, since the spatial resolution of the CO 1–0 data is poor or the spatial coverage of the CO 2–1 data is not enough. So, we expect that further study can give a better understanding of molecular clouds found in our shells.

Third, we report that one of H I supershells listed in Chapter 3 is associated with a compact HVC in the line-of-sight (Chapter 4). We found that GS040.2+00.6−70 (hereafter GS040) is a kpc-size supershell in the outskirts of the Milky Way, and at its geometrical center, the compact HVC 040+01−282 (hereafter CHVC040) is located. They were presented in previous studies (Kang & Koo 2007; Westmeier et al. 2005) with lower resolution H I data ($30'$ and $9'$, respectively), but the high-resolution I-GALFA H I images reveal their detailed spatial and velocity structures. GS040 resembles a cartwheel-like structure which is composed of a ring of radius $\sim 1\overset{\circ}{.}3$, several "spokes" inside, and a bright central "hub." CHVC040 show a bright elongated core, of which size is $\sim 12' \times 15'$, surrounded by diffuse gas with a sharp boundary at the far side of the Galactic disk. Most area of CHVC040 has broad

velocity line profiles of 25–45 km s^{-1} FWHM, but the southwesternmost thin region ($\sim 3'$) with a sharp boundary shows narrower line widths of $\sim$ 19–18 km s^{-1}. GS040 is inferred to be located at $\sim$ 20 kpc from the Sun and below the Galactic plane ($\sim$ 420 pc). Since it is hard to imagine the SN origin for a supershell at such height, CHVC040 is most likely the energy/momentum source for GS040. The analysis of the morphological and physical properties of the both objects suggests that CHVC040 might be the remains of the original HVC which collided with the Galactic disk $\sim$ 4.3 Myrs ago. Also, CHVC040 might be of extragalactic origin rather than originating from a Galactic fountain since it is located at the far outer Galaxy. That is, CHVC040 might be either a fragment of a nearby disrupted galaxy or a cloud originated from an intergalactic accreting flow. Our results imply that some compact HVCs can survive their journey through the Galactic halo and provide energy and momentum into the Milky Way disk.

We present that H I shells can be relevant to SNRs in the first sub-project, but many missing SNRs are expected when considering SN rate and SNR timescale visible in radio continuum emission. That is, there could be many old SNRs or supershells not visible in radio continuum but visible in the H I 21-cm line. It means that search for such H I features is worthwhile, so we did the second sub-project. In the second sub-project, comparison of Galactocentric distribution with molecular clouds and H II regions may imply that many H I shells/supershells, when considering inner Galactic worms, may be formed by stellar feedback. However, some supershells in the outskirts of the Milky Way are in doubt, and an alternative formation mechanism may be needed. In the third project, we show that one of H I supershells in the outskirts is, indeed, probably originated by the HVC impact to the Galactic disk. The results of this thesis provide a better understanding of the nature and origin of H I shells/supershells, and it could be helpful to understand diffuse ISM.

Bibliography

Abdo, A. A., Ackermann, M., Ajello, M., et al. 2009, ApJ, 706, L1

Abdo, A. A., Ackermann, M., Ajello, M., et al. 2010, Science, 327, 1103

Anderson, L. D., Bania, T. M., Balser, D. S., & Rood, R. T. 2011, ApJS, 194, 32

Anderson, L. D., Bania, T. M., Balser, D. S., & Rood, R. T. 2012, ApJ, 754, 62

Anderson, L. D., Bania, T. M., Balser, D. S., et al. 2014, ApJS, 212, 1

Anderson, L. D., Armentrout, W. P., Johnstone, B. M., et al. 2015, ApJS, 221, 26

Arbutina, B., Urošević, D., Stanković, M., & Tešić, Lj. 2004, MNRAS, 350, 346

Bagetakos, I., Brinks, E., Walter, F., et al. 2011, AJ, 141, 23

Barriault, L., Joncas, G., Lockman, F. J., & Martin, P. G. 2010, MNRAS, 407, 2645

Billot, N., Noriega-Crespo, A., Carey, S., Guieu, S., Shenoy, S., Paladini, R., & Latter, W. 2010, ApJ, 712, 797

Bolatto, A. D., Wolfire, M., & Leroy, A. K. 2013, ARA&A, 51, 207

Boomsma, R., Oosterloo, T. A., Fraternali, F., van der Hulst, J. M., & Sancisi, R. 2008, A&A, 490, 555

Boumis, P, Meaburn, J., López, J. A., Mavromatakis, F., Redman, M. P., Harman, D. J., & Goudis, C. D. 2004, A&A, 424, 583

Boumis, P., Mavromatakis, F., Xilouris, E. M., Alikakos, J., Redman, M. P., & Goudis, C. D. 2005, A&A, 443, 175

Boumis, P., Xilouris, E. M., Alikakos, J., Christopoulou, P. E., Mavromatakis, F., Katsiyannis, A. C., & Goudis, C. D. 2009, A&A, 499, 789

Brand, J. & Blitz, L. 1993, A&A, 275, 67

Braun, R., & Strom, R. G. 1986, A&AS, 63, 345

Braun, R., & Burton, W. B. 1999, A&A, 341, 437

Brogan, C. L., Gelfand, J. D., Gaensler, B. M., Kassim, N. E., & Lazio, T. J. W. 2006, ApJ, 639, L25

Brüns, C., Kerp, J., & Pagels, A. 2001, A&A, 370, L26

Burton, W. B. 1988, in: Galactic and Extragalactic Radio Astronomy, 2nd ed., Eds. G. L. Verschuur, K. I. Kellermann (Springer, Berlin) 154

Camilo, F., Lorimer, D. R., Bhat, N. D. R., et al. 2002, ApJ, 574, L71

Case, G. L., & Bhattacharya, D. 1998, ApJ, 504, 761

Castelletti, G., Dubner, G., Brogan, C., & Kassim, N. E. 2007, A&A, 471, 537

Caswell, J. L., Murray, J. D., Roger, R. S., Cole, D. J., & Cooke, D. J. 1975, A&A, 45, 239

Cazzolato, F., & Pineault, S. 2005, AJ, 129, 2731

Chevalier, R. A. 1999, ApJ, 511, 798

Churchwell, E., Povich, M. S., Allen, D., Taylor, M. G., Meade, M. R., Babler, B. L., Indebetouw, R., Watson, C., Whitney, B. A., Wolfire, M. G., Bania, T. M., Benjamin, R. A., Clemens, D. P., Cohen, M., Cyganowski, C. J., Jackson, J. M., Kobulnicky, H. A., Mathis, J. S., Mercer, E. P., Stolovy, S. R., Uzpen, B., Watson, D. F.; Wolff, M. J. 2006, ApJ, 649, 759

Cioffi, D. F., McKee, C. F., & Bertschinger, E. 1988, ApJ, 334, 252

Daigle, A., Joncas, G., & Parizeau, M. 2007, ApJ, 661, 285

Dame, T. M., Hartmann, D., & Thaddeus, P. 2001, ApJ, 547, 792

Dame, T. M., & Thaddeus, P. 2011, ApJ, 734, L24

Dawson, J. R., Kawamura, A., Mizuno, N., Onishi, T., & Fukui, Y. 2008a, PASJ, 60, 1297

Dawson, J. R., Mizuno, N., Onishi, T., McClure-Griffiths, N. M., & Fukui, Y. 2008b, MNRAS, 387, 31

Dawson, J. R., McClure-Griffiths, N. M., Kawamura, A., et al. 2011, ApJ, 728, 127

Dawson, J. R. 2013, PASA, 30, e025

Dawson, J. R., Ntormousi, E., Fukui, Y., Hayakawa, T., & Fierlinger, K. 2015, ApJ, 799, 64

de Heij, V., Braun, R., & Burton, W. B. 2002, A&A, 391, 159

Dennison, B., Simonetti, J. H., & Topasna, G. A. 1998, PASA, 15, 147

Deul, E. R., & den Hartog, R. H. 1990, A&A, 229, 362

Dickey, J. M., & Lockman, F. J. 1990, ARA&A, 28, 215

Dunham, M. K., Rosolowsky, E., Evans, N. J., II, Cyganowski, C., & Urquhart, J. S. 2011, ApJ, 741, 110

Ehlerová, S., & Palouš, J. 2005, A&A, 437, 101

Ehlerová, S., & Palouš, J. 2013, A&A, 550, A23

Ehlerová, S., & Palouš, J. 2016, A&A, 587, A5

Faridani, S., Flöer, L., Kerp, J., & Westmeier, T. 2014, A&A, 563, A99

Fesen, R. A., Saken, J. M., & Shull, J. M. 1988, Nature, 334, 229

Finkbeiner, D. P. 2003, ApJS, 146, 407

Folgheraiter, E. L., Warwick, R. S., Watson, M. G., & Koyama, K. 1997, MNRAS, 292, 365

Frail, D. A., & Clifton, T. R. 1989, ApJ, 336, 854

Froebrich, D., Davis, C. J., Ioannidis, G., et al. 2011, MNRAS, 413, 480

Giacani, E. B., Dubner, G., Cappa, C., & Testori, J. 1998, A&AS, 133, 61

Gibson, S. J., Koo, B., Douglas, K. A., et al. 2012, American Astronomical Society Meeting Abstracts, 219, #349.29

Gillmon, K., Shull, J. M., Tumlinson, J., & Danforth, C. 2006, ApJ, 636, 891

Giovanelli, R., & Haynes, M. P. 1979, ApJ, 230, 404

Giuliani, A., Cardillo, M., Tavani, M., et al. 2011, ApJ, 742, L30

Green, D. A. 2004, Bulletin of the Astronomical Society of India, 32, 335

Green, D. A. 2009a, Bulletin of the Astronomical Society of India, 37, 45

Green, D. A. 2009b, MNRAS, 399, 177

Green, D. A. 2014, Bulletin of the Astronomical Society of India, 42, 47

Guseinov, O. H., Ankay, A.,Sezer, A., & Tagieva, S. O. 2003, A&AT, 22, 273

Hadfield, L. J., van Dyk, S. D., Morris, P. W., Smith, J. D., Marston, A. P., & Peterson, D. E. 2007, MNRAS, 376, 248

Haffner, L. M., Reynolds, R. J., Tufte, S. L., et al. 2003, ApJS, 149, 405

Harrus, I. M., Hughes, J. P., Singh, K. P., Koyama, K., & Asaoka, I. 1997, ApJ, 488, 781

Hartmann, D., & Burton, W. B. 1997, Atlas of Galactic Neutral Hydrogen, by Dap Hartmann and W. Butler Burton, pp. 243. ISBN 0521471117. Cambridge, UK: Cambridge University Press, February 1997

Hartmann, L., Ballesteros-Paredes, J., & Bergin, E. A. 2001, ApJ, 562, 852

Heiles, C., & Habing, H. J. 1974, A&AS, 14, 1

Heiles, C. 1976, ApJ, 208, L137

Heiles, C. 1979, ApJ, 229, 533

Heiles, C. 1984, ApJS, 55, 585

Heiles, C. 1987, ApJ, 315, 555

Heiles, C., & Troland, T. H. 2003, ApJ, 586, 1067

Heitsch, F., & Putman, M. E. 2009, ApJ, 698, 1485

Heitsch, F., Bartell, B., Clark, S. E., et al. 2016, arXiv:1606.06689

Heyer, M., & Dame, T. M. 2015, ARA&A, 53, 583

Higdon, J. C., & Lingenfelter, R. E. 2005, ApJ, 628, 738

HI4PI Collaboration, Ben Bekhti, N., Flöer, L., et al. 2016, A&A, 594, A116

van der Hucht, K. A. 2001,New Astron. Rev., 45, 135

Hunter, D. A., & Massey, P. 1990, AJ, 99, 846

Inutsuka, S.-i., Inoue, T., Iwasaki, K., & Hosokawa, T. 2015, A&A, 580, A49

Jackson, J. M., et al. 2006, ApJS, 163, 145

Jiang, B., Chen, Y., Wang, J., Su, Y., Zhou, X., Safi-Harb, S., & DeLaney, T. 2010, ApJ, 712, 1147

Jin, S. 2010, MNRAS, 408, L85

Junkes, N., Fuerst, E., & Reich, W. 1992a, A&AS, 96, 1

Junkes, N., Fuerst, E., & Reich, W. 1992b, A&A, 261, 289

Junkes, N. 1996, Unsolved Problems of the Milky Way, 169, 627

Kang, J.-h., & Koo, B.-C. 2007, ApJS, 173, 85

Kamphuis, J., Sancisi, R., & van der Hulst, T. 1991, A&A, 244, L29

Kalberla, P. M. W., Burton, W. B., Hartmann, D., et al. 2005, A&A, 440, 775

Kalberla, P. M. W., & Dedes, L. 2008, A&A, 487, 951

Kalberla, P. M. W., & Kerp, J. 2009, ARA&A, 47, 27

Kang, J.-H., & Koo, B.-C. 2007, ApJS, 173, 85

Kawamura, A., Kun, M., Onishi, T., et al. 2001, PASJ, 53, 1097

Kerr, F. J. 1969, ARA&A, 7, 39

Kim, H.-J., Koo, B.-C., & Moon, D.-S. 2013, ApJ, 774, 5

Koo, B.-C., Reach, W. T., Heiles, C., Fesen, R. A., & Shull, J. M. 1990, ApJ, 364, 178

Koo, B.-C., & Heiles, C. 1991, ApJ, 382, 204 (KH91)

Koo, B.-C., Heiles, C., & Reach, W. T. 1992, ApJ, 390, 108

Koo, B.-C., Yun, M.-S., Ho, P. T. P., & Lee, Y. 1993, ApJ, 417, 196

Koo, B.-C., & Heiles, C. 1995, ApJ, 442, 679

Koo, B.-C., Kim, K.-T., Seward, F. D. 1995, ApJ, 447, 211

Koo, B.-C., & Moon, D.-S. 1997a, ApJ, 475, 194

Koo, B.-C., & Moon, D.-S. 1997b, ApJ, 485, 263

Koo, B.-C., & Kang, J.-h. 2004, MNRAS, 349, 983

Koo, B.-C., Kang, J.-h., & McClure-Griffiths, N. M. 2004, Journal of Korean Astronomical Society, 37, 61

Koo, B.-C., McKee, C. F., Lee, J.-J., et al. 2008, ApJ, 673, L147

Koo, B.-C., Heiles, C., Stanimirović, S., & Troland, T. 2010, AJ, 140, 262

Koo, B.-C., et al. 2017, arXiv:1706.10084, PASP in press

Koralesky, B., Frail, D. A., Goss, W. M., Claussen, M. J., & Green, A. J. 1998, ApJ, 116, 1323

Kothes, R., Reich, W., Foster, T., & Byun, D.-Y. 2003, ApJ, 588, 852

Kothes, R., Landecker, T. L., & Wolleben, M. 2004, ApJ, 607, 855

Kothes, R., Uyanıker, B., & Reid, R. I. 2005, A&A, 444, 871

Kroupa, P. 2001, MNRAS, 322, 231

Kulkarni, S. R., Clifton, T. C., Backer, D. C., Foster, R. S., & Fruchter, A. S. 1988, Nature, 331, 50

Kwak, K., Shelton, R. L., & Raley, E. A. 2009, ApJ, 699, 1775

Lada, C. J., & Lada, E. A. 2003, ARA&A, 41, 57

Lada, C. J. 2016, Young Stars & Planets Near the Sun, 314, 8

Lang, C. C., Wang, Q. D., Lu, F., & Clubb, K. I. 2010, ApJ, 709, 1125

Lee, J.-J., Koo, B.-C., Yun, M. S., Stanimirović, S., Heiles, C., & Heyer, M. 2008, AJ, 135, 796

Lee, H.-G., Moon, D.-S., Koo, B.-C., Lee, J.-J., & Matthews, K. 2009, ApJ, 691, 1042

Levine, E. S., Blitz, L., & Heiles, C. 2006, ApJ, 643, 881

Levine, E. S., Heiles, C., & Blitz, L. 2008, ApJ, 679, 1288

Li, W., Chornock, R., Leaman, J., Filippenko, A. V., Poznanski, D., Wang, X., Ganeshalingam, M., & Mannucci, F. 2011, MNRAS, 412, 1473

Liszt, H. 2014, ApJ, 783, 17

Lockman, F. J. 1989, ApJS, 71,469

Lockman, F. J., Blundell, K. M., & Goss, W. M. 2007, MNRAS, 381, 881

Loeb, A., & Perna, R. 1998, ApJ, 503, L35

Lozinskaya, T. A., Sitnik, T. G., & Pravdikova, V. V. 1993, ARep, 37, 240

Maciejewski, W., Murphy, E. M., Lockman, F. J., & Savage, B. D. 1996, ApJ, 469, 238

Marsden, D., Lingenfelter, R. E., Rothschild, R. E., & Higdon, J. C. 2001, ApJ, 550, 397

Markwardt, C. B. 2009, Astronomical Society of the Pacific Conference Series, 411, 251 (http://purl.com/net/mpfit)

Matthews, B. C., Wallace, B. J., & Taylor, A. R. 1998, ApJ, 493, 312

Mavromatakis, F., Papamastorakis, J., Ventura, J., Becker, W., Paleologou, E. V, & Schaudel, D. 2001, A&A, 370, 265

McClure-Griffiths N. 2001, PhD thsis, Univ. Minnesota

McClure-Griffiths, N. M., Dickey, J. M., Gaensler, B. M., & Green, A. J. 2002, ApJ, 578, 176

McClure-Griffiths, N. M., Dickey, J. M., Gaensler, B. M., & Green, A. J. 2003, ApJ, 594, 833

McClure-Griffiths, N. M., Dickey, J. M., Gaensler, B. M., et al. 2005, ApJS, 158, 178

McClure-Griffiths, N. M. 2012, AN, 333, 497

McCray, R., & Kafatos, M. 1987, ApJ, 317, 190

Mirabel, I. F., & Morras, R. 1990, ApJ, 356, 130

Miville-Deschênes, M.-A., Murray, N., & Lee, E. J. 2017, ApJ, 834, 57

Maoz, D., & Mannucci, F. 2012, PASA, 29, 447

Norman, C. A., & Ikeuchi, S. 1989, ApJ, 345, 372

Ntormousi, E., Burkert, A., Fierlinger, K., & Heitsch, F. 2011, ApJ, 731, 13

Paladini, R., Burigana, C., Davies, R. D., et al. 2003, A&A, 397, 213

Park, G., Koo, B.-C., Gibson, S. J., Kang, J.-h., Lane, D. C., Douglas, K. A., Peek, J. E. G., Korpela, E. J., Heiles, C., Newton, J. H. 2013, ApJ, 777, 14

Park, G., Koo, B.-C. et al. accpeted in ApJL

Peek, J. E. G., Begum, A., Douglas, K. A., et al. 2010, Astronomical Society of the Pacific Conference Series, 438, 393

Peek, J. E. G., Heiles, C., Douglas, K. A., et al. 2011, ApJS, 194, 20

Petre, R., Kuntz, K. D., & Shelton, R. L. 2002, ApJ, 579, 404

Piddington, J. H., & Minnett, H. C. 1952, Australian Journal of Scientific Research A Physical Sciences, 5, 17

Pidopryhora, Y., Lockman, F. J., & Shields, J. C. 2007, ApJ, 656, 928

Planck Collaboration, Ade, P. A. R., Aghanim, N., et al. 2014, A&A, 571, A13

Plöckinger, S., & Hensler, G. 2012, A&A, 547, AA43

Putman, M. E., de Heij, V., Staveley-Smith, L., et al. 2002, AJ, 123, 873

Putman, M. E., Saul, D. R., & Mets, E. 2011, MNRAS, 418, 1575

Putman, M. E., Peek, J. E. G., & Joung, M. R. 2012, ARA&A, 50, 491

Reach, W. T., Koo, B.-C., & Heiles, C. 1994, ApJ, 429, 672

Reach, W. T., Rho, J., & Jarrett, T. H. 2005, ApJ, 618, 297

Reed, B. C. 2005, AJ, 130, 1652

Reed, B. C. 2003, AJ, 125, 2531

Reich, W., Furest, E., Reich, P., & Reif, K. 1990, A&AS, 85, 633

Rho, J., & Petre, R. 1998, ApJ, 503, L167

Rhode, K. L., Salzer, J. J., Westpfahl, D. J., & Radice, L. A. 1999, AJ, 118, 323

Roberts, W. W. 1969, ApJ, 158, 123

Robin, A. C., Creze, M., & Mohan, V. 1992, ApJ, 400, L25

Ruphy, S., Robin, A. C., Epchtein, N., et al. 1996, A&A, 313, L21

Rosolowsky, E., & Leroy, A. 2006, PASP, 118, 590

Russeil, D. 2003, A&A, 397, 133

Sakamoto, S., Hasegawa, T., Handa, T., Hayashi, M., & Oka, T. 1997, ApJ, 486, 276

Sallmen, S. M., Korpela, E. J., Bellehumeur, B., et al. 2015, AJ, 149, 189

Santillán, A., Franco, J., Martos, M., & Kim, J. 1999, ApJ, 515, 657

Savage, B. D., Bohlin, R. C., Drake, J. F., & Budich, W. 1977, ApJ, 216, 291

Seta, M., Hasegawa, T., Dame, T. M., Sakamoto, S., Oka, T., Handa, T., Hayashi, M., Morino, J.-I., Sorai, K., & Usuda, K. S. 1998, ApJ, 505, 286

Smartt, S. J. 2009, ARA&A, 47, 63

Solomon, P. M., Rivolo, A. R., Barrett, J., & Yahil, A. 1987, ApJ, 319, 730

Stil, J. M., Taylor, A. R., Dickey, J. M., Kavars, D. W., Martin, P. G., Rothwell, T. A., Boothroyd, A. I., Lockman, F. J., & McClure-Griffiths, N. M. 2006, AJ, 132, 1158

Suad, L. A., Caiafa, C. F., Arnal, E. M., & Cichowolski, S. 2014, A&A, 564, A116

Tamanaha, C. M. 1997, ApJS, 109, 139

Taylor, J. H., & Cordes, J. M. 1993, ApJ, 411, 674

Taylor, A. R., Gibson, S. J., Peracaula, M., et al. 2003, AJ, 125, 3145

Tenorio-Tagle, G. 1980, A&A, 88, 61

Tenorio-Tagle, G., Franco, J., Bodenheimer, P., & Rozyczka, M. 1987, A&A, 179, 219

Voges, W., Aschenbach, B., Boller, T., et al. 1999, A&A, 349, 389

Wada, K., Spaans, M., & Kim, S. 2000, ApJ, 540, 797

Wakker, B. P. 1991, A&A, 250, 499

Wakker, B. P., & van Woerden, H. 1991, A&A, 250, 509

Wakker, B. P. 2004, Ap&SS, 289, 381

Wang, B., & Han, Z. 2012, NewAR, 56, 122

Weaver, H. 1970, The Spiral Structure of our Galaxy, 38, 126

Weaver, H., & Williams, D. R. W. 1973, A&AS, 8, 1

Weaver, H. 1974, Galactic Radio Astronomy, 60, 573

Westmeier, T., Brüns, C., & Kerp, J. 2005, A&A, 432, 937

Wilson, T. L., Rohlfs, K., & Hüttemeister, S. 2013 *Tools of Radio Astronomy* (6th ed.; Berlin: Springer)

Winkel, B., Ben Bekhti, N., Darmstädter, V., et al. 2011, A&A, 533, A105

Wolszczan, A., Cordes, J. M., & Dewey, R. J. 1991, ApJ, 372, L99

Wolszczan, A., Cordes, J. M., & Dewey, R. J. 1991, ApJ, 372, L99

Wootten, H. A. 1977, ApJ, 216, 440

Xu, W. F., Gao, X. Y., Han, J. L., & Liu, F. S. 2013, A&A, 559, A81

Xu, J.-L., & Ju, B.-G. 2014, A&A, 569, A36

Yamaguchi, H., Ueno, M., Koyama, K., Bamba, A., & Yamauchi, S. 2004, PASJ, 56, 1059

Yang, J., Zhang, J.-L., Cai, Z.-Y., Lu, D.-R., & Tan, Y.-H. 2006, Chinese J. Astron. Astrophys., 6, 210

Yoshita, K., Miyata, E., & Tsunemi, H. 2000, PASJ, 52, 867

Yu, N.-P., & Wang, J.-J. 2012, Research in Astronomy and Astrophysics, 12, 651

Appendix A

Brief Description of All H I Shells listed in Chapter 3

Heiles' shells in Table 3.1 are discussed as follow:

GS033+06−49.— It is thought that transient H I gas makes a shell-like feature. Its eastern part is visible as thin and bright arc within the velocity range.

GS034.7−05.5+61 (GS034−06+65).— This shell looks like a water drop and is located below the Galactic disk. It is seen at similar velocities with GS035.1+05.9+57 (GS036+06+55). See Section 3.3.2 for details.

GS034+02+73.— H I hole surrounded by irregular filamentary clumps are seen, but it does not seem to be a shell.

GS035.1+05.9+57 (GS036+06+55).— An arc-like H I structure is seen at slightly high latitudes. See Section 3.3.2 for details.

GS042.0+00.4+29 (GS041+01+27).— This is one of the prominent supershells in the I-GALFA survey area. It looks like a complete ellipse which is apparently filled with H I gas features. See Section 3.3.2 for details.

GS046.6−00.4−17 (GS046−01−15).— This is a stationary, incomplete shell of which the southern part is missing. Unlike the previous description of this shell, we found

a differently shaped shell which is longish along Galactic longitudes in given coordinates and velocities.

GS045.4−01.1+93 (GS046−01+83).— This is distinct from a simply expected shell-shape which has H I enhancement along shell walls with a hole in an interior area. We redefined that this shell has an angular size of $6.2^\circ \times 5.8^\circ$ at the center of (ℓ, b) = (45.4°, -1.1°) and extends more up to $\sim +110$ km s^{-1}. Lots of clumps and small filaments seem to be more concentrated within the area of the shell than its outside. This shell is a bit vague but appears to have a weak outer boundary. Meanwhile, the shell appears at higher velocities than the maximum value ($\sim$ 62 km s^{-1}) allowed by Galactic rotation in its sight line.

GS048−04+49.— Several filamentary structures are visible, and some of them seem to make a wall around a relatively faint center. However, it does not look like a shell.

GS053.0−05.0+26 (GS052−05+25).— This is one of the prominent shells in the I-GALFA data. Its center is considerably far away from the midplane, and the whole structure is below it. Its northern part is apparently connected with gas in the plane, so the outer boundary of the region is ambiguous. The eastern wall seems relatively thicker than the other part. Also, many filamentary structures stretch from inside to outside the shell.

GS052+07+39, GS063+04+13, & GS063−01−3.— It is probably not a shell, instead, many clumps and filaments appear around relatively a faint center.

GS057.5+02.6−14 (GS057+03−11) & GS056.8+00.1−21 (GS057+01−33).— GS057.5+02.6−14 (GS057+03−11) has a thick wall of which the edge is partially bright. In a certain range of velocities, it is connecting with another Heiles' shell, GS056.8+00.1−21 (GS057+01−33). It is difficult to discern an expansion of GS056.8+00.1−21 (GS057+01−33) since H I gas seems to flow from lower to higher longitudes as velocity decreases.

GS061.6−00.4+54 (GS061+00+51).— This shell has complicated walls. The eastern

and western walls appear to be connected with different H I features, but it is not certain whether they are related to each other or not.

GS064.3−00.9−80 (GS064−01−97).— This is a shell with an inclined elliptical shape and seems to be stationary, not expanding. A tail-like feature is apparent outward the southeastern wall. At velocities higher than ∼85 km s^{-1}, H I emission toward the western wall is still bright, but it is not sure whether it belongs to this shell or not. On the other hand, another shell having a much larger size appears (See Section 3.3.2).

GS064.0−01.1+45 (GS066−01+35).— The eastern wall of the shell is seen but faint, and the western one is unclear because of contamination from other features. Also, the western wall is apparently overlapped with a larger, straight filamentary feature.

GS066.8−02.1−39 (GS067−02−37).— This is a faint shell, and it is ambiguous whether its southeastern wall is closed or open.

GS074.8−00.9+29 (GS075−01+39).— Since the I-GALFA survey partially covers this shell, we additionally used the LAB data to examine this shell. On the whole, this is an expanding shell with complicated walls. In the view of high resolution, lots of gas makes filamentary structures from center to the outside. See Section 3.3.2 for details.

New Shell Candidates in Table 3.2 are discussed as follow:

GS031.4+01.1+65.— This seems to be elongated and tilted with respect to the Galactic plane in (ℓ, b) maps, also shows relatively shell-like feature in PV maps. A filamentary structure is apparently overlapped on the southwestern wall and spreads inside and outside.

GS034.2+02.4−77.— This looks like a relatively well-defined circular shell in an (ℓ, b) map. When seeing in PV maps, it appears at the very edge of galactic gas in high negative velocities. It is uncertain that the shell is open toward higher negative

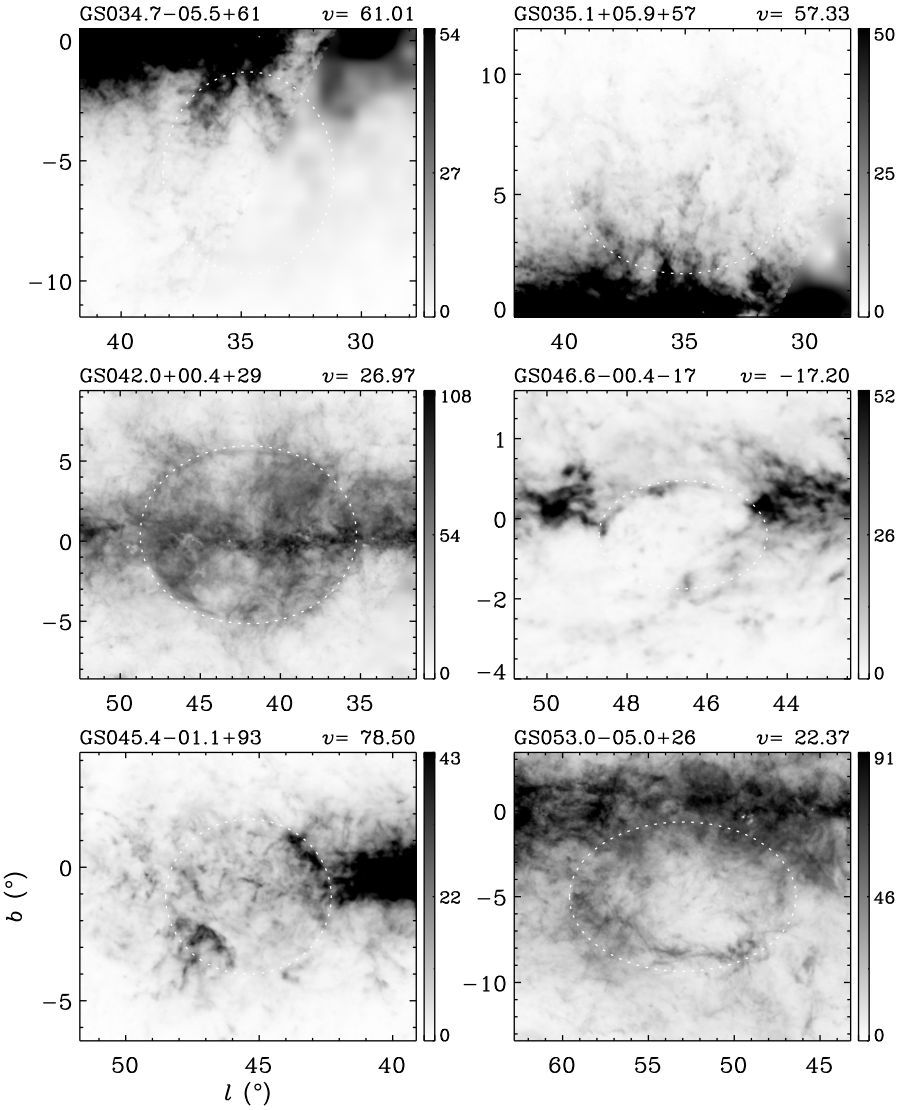

Figure A.1. A representative H I channel map showing Heiles' shells in Table 3.1. A name of a shell is written in the top left of each panel, and a channel velocity at the top right in km s^{-1}. A channel width is 0.92 km s^{-1}. A white dotted ellipse is drawn to help locating a shell.

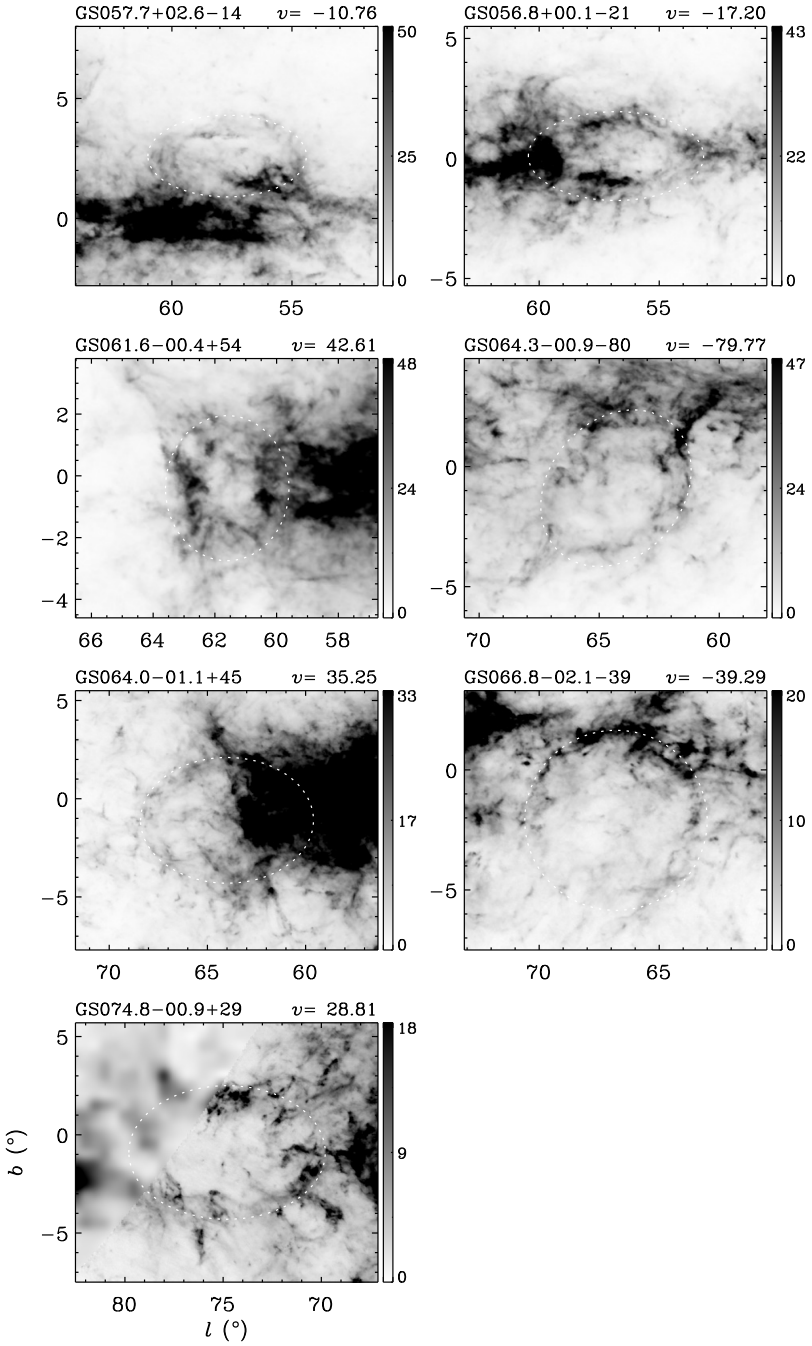

Figure A.1. *Continued*

velocities or not.

GS034.5−01.1+72.— This is a thin arc-like structure just below the midplane. A relatively thicker, different arc-like feature appears in the northeastern part of the shell, also many clumps within the shell.

GS036.4+00.8−37, GS036.8−01.0−35 and GS037.5+00.5−39.— Apparently, these are adjacent to each other in a certain range of velocities. GS036.4+00.8−37 shows an uneven wall on the western side, but the eastern part is not clear. GS037.5+00.5−39 appears in the east of GS036.4+00.8−37, and its western wall seems to be missing. For the two shells, the ambiguous parts are where they overlap assuming a complete elliptical shape. It is uncertain that they are physically associated or not. GS36.8−01.0−35 is bordering on the southern wall of GS37.5+00.5−39 and has a very faint thin wall in the south.

GS037.9+00.5−25, GS061.3+02.6−69, and GS072.3+03.1−56.— These show half shells of which walls in the north are visible but weak. Their inner boundaries are somewhat sharp. The southern part of each shell is ambiguous since other structures of ambient gas are contaminated.

GS040.2+00.6`70.— It shows a cartwheel-like shape which is different from those of other shells. It is seen at relatively higher negative velocities than H I disk gas in the same line of sight. See Section 3.4.2 for details.

GS044.3−00.1−39.— It is very elongated toward longitudes, and a longitudinal extent is about twice latitudinal one. The southern part seems to be open.

GS044.9−12.8+20.— This seems like a half shell of which the eastern part is bright.

GS045.0−08.1+32.— This is an almost complete shell. Several filamentary features, in the shape of a rake, appear inside.

GS047.0+01.2−35 and GS048.4+00.6−40.— These are located side-by-side along longitudes in a certain range of velocities. The surroundings of two shells are quite complicated with filamentary and arc-like features. While GS047.0+01.2−35 is a

complete shell, GS048.4+00.6−40 is a partial shell. GS048.4+00.6−40 are seen from −40 km s^{-1} to −29 km s^{-1}, and the shell walls are distinct. Its shape is changed somewhat around −40 km s^{-1}: only a half shell in the north is visible at $v_{\rm LSR}$ > −40 km s^{-1} while faint partial shell walls in south appear at $v_{\rm LSR}$ > −40 km s^{-1}. When seeing velocity line profiles, some positions along shell walls show two peaks. It would be more likely to consider them as sub-structures in a single system, not two different shells. That is because their sizes are very similar and velocities where such structures are continuative. In the same point, it does not imply expansion.

GS047.6−00.1−98.— This seems like an incomplete circular shell and appears at very negative velocities in the line of sight. Cross sections shown in PV maps represent a protruding feature from Galactic disk gas like GS040.2+00.6−70.

GS048.3−00.8−25.— This shell has a sparse wall, and its boundary seems to be ambiguous.

GS053.6−00.2+5.— It shows a ring-shape of which the southeastern part is broken in an (ℓ, b) map. In PV maps, it looks like an expanding shell bordering gas neighboring the Sun at around 10 km s^{-1}, which may not be physically associated.

GS053.6+00.4+29.— This seems to be an almost complete circular shell with a quite clear inner boundary. Part of the shell shows relatively thin walls. See Section 3.4.2 for details.

GS056.1−02.1−21.— This is likely to be an expanding, hemispherical shell. It shows a partial wall that two parts in the south are unfilled. There is a tail-like feature in the southwest, which seems like a passage through one of the open parts, out of a marked ellipse. It is not sure if they are just a coincidence or not.

GS060.2+01.1−74.— It is an almost complete shell, but partially opened.

GS063.3−00.4−3.— It seems to be an expanding, uneven circular shell. When seeing (v, b) maps, it shows a hole and dramatic change of shape beyond the negative velocity boundary of this shell. It is unclear whether they organize a single system

or not.

GS063.6+01.0−71.— This is a circular shell of which the center is crossed by filamentary features in the shape of a trident.

GS067.5+00.1−93.— This is the largest supershell in the I-GALFA area and is seen at quite high negative velocities. See Section 3.4.2 for details.

GS072.3+01.3−46.— It is a partial shell of a large arc in the west which extends from positive to negative latitudes.

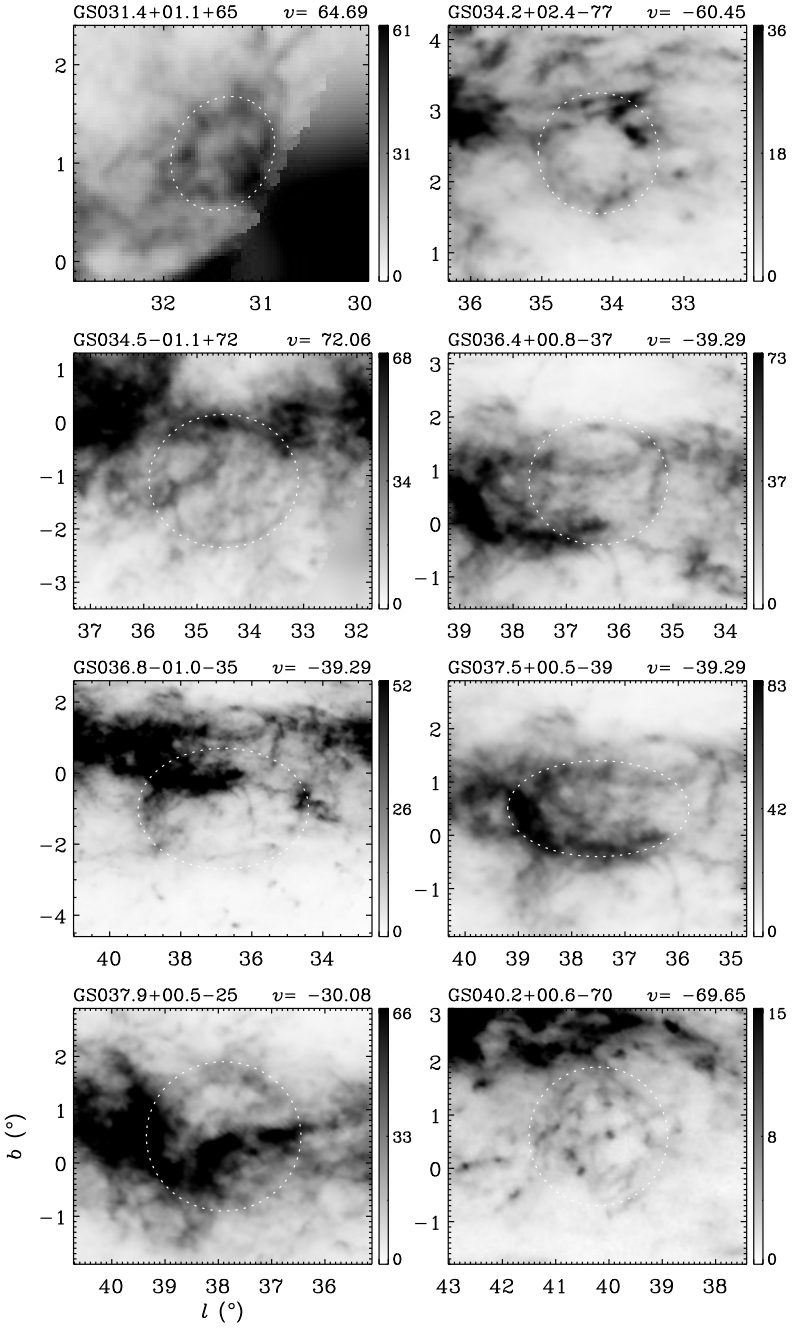

Figure A.2. Same as Figure A.1, but for new shell candidates in Table 3.2.

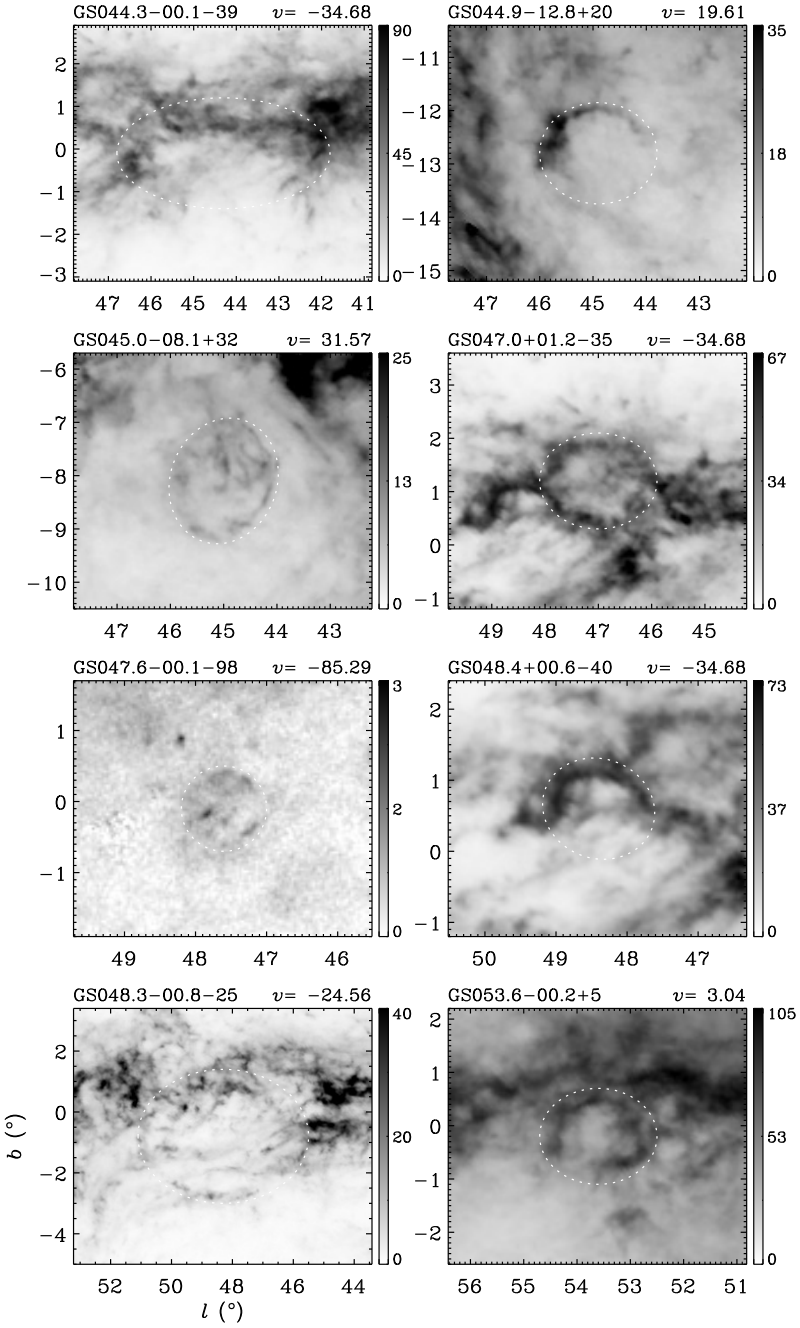

Figure A.2. Continued

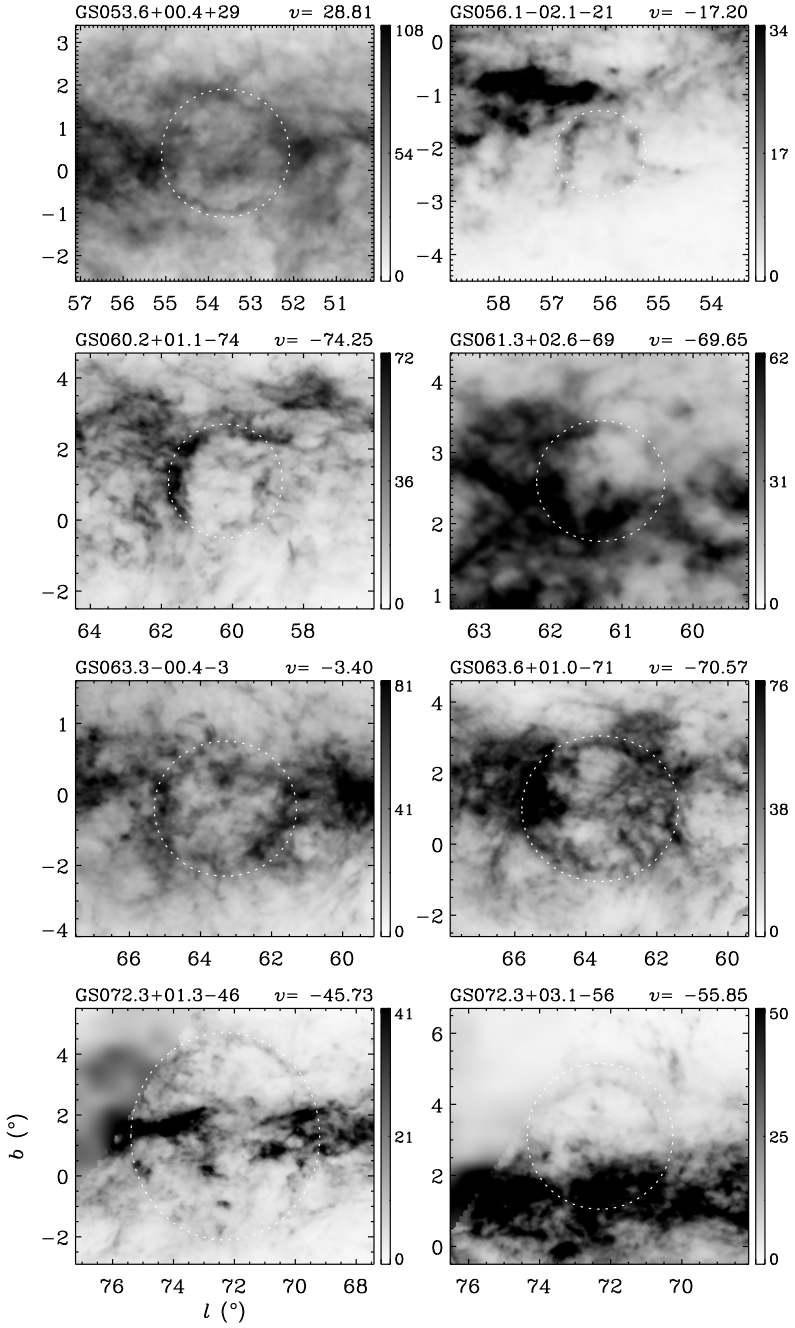

Figure A.2. Continued

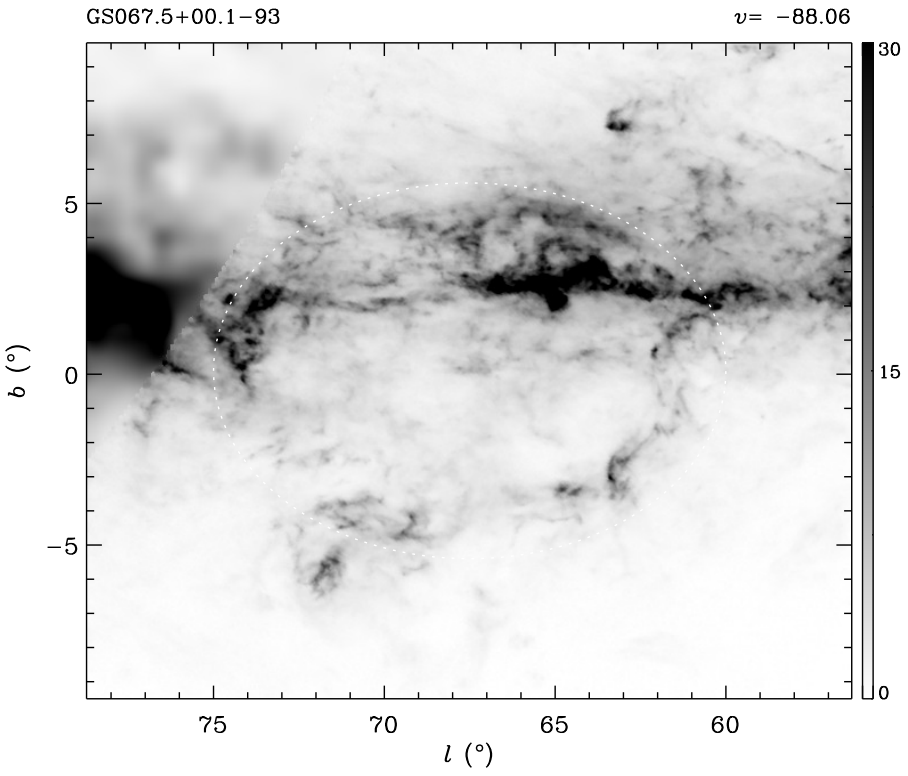

Figure A.2. Continued

Appendix B

Comparison of H I Shells in Chapter 3 with Other H I Shell Catalogs

In this section, we describe comparison results of individual shells listed in Tables 3.1 and 3.2 from those in Ehlerová & Palouš (2013) or Sallmen et al. (2015) (See Section 3.7 for details of the two catalogs). Table B.1 lists comparable shells, although they are not completely the same in a spatial definition and velocity range where shells are seen.

Table B.1

Comparison with Other Shell Catalogs

Shell Name				Note
This Paper	Heiles (1979)	Ehlerová & Palouš (2013)	Sallmen et al. (2015)	
Those in Table 3.1				
GS034.7−05.5+61	GS034−06+65	GS35.0−6.5+52.6	···	···
GS042.0+00.4+29	GS041+01+27	GS43.5+4.5+25.8	···	*
GS053.0−05.0+26	GS052−05+25	GS50.0−5.0+19.6	GSH052−05+023 and GSH056−06+033	†
GS056.8+00.1−21	GS057+01−33	GS56.5+0.0−22.7	···	···
GS061.6−00.4+54	GS061+00+51	GS61.5−0.5+46.4	···	···
GS064.0−01.1+45	GS066−01+35	···	GSH062+00+045	···
GS074.8−00.9+29	GS075−01+39	GS75.5−1.0+25.8	···	···
Those in Table 3.2				
GS053.6−00.2+5	···	···	GSH054−00+003	···
GS053.6+00.4+29	···	···	GSH054+01+031	‡
GS063.3−00.4−3	···	GS63.5−0.5−01.0	···	···
GS063.6+01.0−71	···	···	GSH060+01−076	···

*Ehlerová & Palouš was found a shell toward GS041+01+27, but the Ehlerová & Palouš's shell does not cover the whole structure of GS041+01+27 which is remarkably extended in an (ℓ, b) map. The region inside/around GS041+01+27 is very complicated with other H I gas, so Ehlerová & Palouš could catch a part of the shell where is less crowded.

†Sallmen et al. identified two separate shells, but we consider that the two features can be associated and give a similar definition with what Heiles gave.

‡Sallmen et al. identified a smaller shell with the center shifted toward the northwest, which is a lower intensity-part than the surrounding. They mentioned that the southern wall of their shell might be a cloud inside it, and this is what we described in Section 3.4.2.

Appendix C

Examination of CO Emission in H I Shells of Chapter 3

We usually used the CO CfA survey data described in Section 3.8.2. Among thirty-eight shells, thirty-two are almost entirely covered by the CO CfA data, and two are not. For four, less than half the area are covered by the CO CfA data. We made a velocity-integrated map over the velocity range where a shell is visible in H I and examined emission feature brighter than $\sim 1.5\ \mathrm{K\,km\,s^{-1}}$. In some cases, we looked into the ^{13}CO GRS Survey (Jackson et al. 2006), the Planck ^{12}CO integral map (Planck Collaboration et al. 2014), also referred literary reports. Comparison results of all shells are recorded in Table C.1. We note that the results are limited to the data used.

Table C.1

CO Emission in H I Shells/Supershells

Shell Name	Characteristics of CO Emission	Ref.
GS031.4+01.1+65	An elongated clump having two peaks in the eastern wall in vr = (+59.5, +65) km s^{-1} and another clump (having multi-velocity components) in the western wall.	1
	Fragmented filamentary features inside ^{12}CO clumps.	2[a]
GS034.2+02.4−77	No CO emission associated with shell walls.	1
GS034.5−01.1+72	CO emission is seen at some same velocities, but it seems to be not associated.	1
GS034.7−05.5+61	No CO emission associated with shell walls.	1[b]
GS035.1+05.9+57	No CO emission associated with shell walls.	1[b]
GS036.4+00.8−37	No CO emission associated with shell walls.	1
GS036.8−01.1−35	CO emission is seen at some same velocities, but it seems to be not associated.	1
GS037.5+00.5−39	An elongated source in the southeastern wall ($\ell \sim 38\overset{\circ}{.}8$, $b \sim +0\overset{\circ}{.}1$) in vr = (−41, −32) km s^{-1}.	1
GS037.9+00.5−25	A compact source in the eastern wall ($\ell \sim 39\overset{\circ}{.}3$, $b \sim +0\overset{\circ}{.}4$) in vr = (−32, −26) km s^{-1}.	1
GS040.2+00.6−70	No CO emission associated with shell walls.	1
GS042.0+00.4+29	Complicated area, but some plausible features (e.g., a clump in the northern wall ($\ell \sim 44\overset{\circ}{.}4$, $b \sim 5\overset{\circ}{.}3$) in the velocity range (vr) of (+24, +31) km s^{-1}).	1[b]
GS044.3−00.1−39	A compact source in the western wall ($\ell \sim 42\overset{\circ}{.}8$, $b \sim -0\overset{\circ}{.}1$) in vr = (−47, −40) km s^{-1}.	1
GS044.9−12.8+20	No CO emission toward the line of sight.	3
GS045.0−08.1+32	No CO emission at velocities where the shell is seen.	1[c], 3
GS045.4−01.1+93	Weak CO emission features in the southeastern part of the shell and near its center.	1
GS046.6−00.4−17	No CO emission associated with shell walls.	1
GS047.0+01.2−35	A compact source in the southeastern wall ($\sim 42\overset{\circ}{.}8$, $b \sim +0\overset{\circ}{.}6$) which borders with GS048.3 + 00.6 − 35 in vr = (−37, −31) km s^{-1}.	1
GS047.6−00.1−98	No CO emission associated with shell walls.	1
GS048.3−00.8−25	CO emission is seen at some same velocities, but it seems to be not associated.	1
GS048.4+00.6−40	Elongated sources just inside the northeastern wall and a compact one in the western wall which can even be a part of GS047.0 + 01.2 − 35.	1
GS053.0−05.0+26	An elongated source just inside the southwestern wall ($\ell \sim 49\overset{\circ}{.}5$, $b \sim -7\overset{\circ}{.}5$) in vr = (20, 25) km s^{-1}.	1[d], 4
GS053.6−00.2+5	A filamentary feature along the northwestern wall in vr = (−2, +10) km s^{-1}, and a compact source in the northern wall in vr = (0, 5) km s^{-1}.	1

Continued on Next Page...

Table C.1 – Continued

Shell Name	Characteristics of CO Emission	Ref.
	Fragmented, several clumps and smaller filaments in the larger ^{12}CO filament and compact source.	2[e]
GS053.6+00.4+29	Complicated area, but some features possible to be associated. (e.g. a compact source in the southwestern wall in vr = (29, 34) km s^{-1}; sizable cloud(s) inside the shell)	1
GS056.1−02.1−21	No CO emission associated with shell walls.	1
GS056.8+00.1−21	Some clumps along the southern wall (e.g., $\ell \sim 55^\circ, 57\overset{\circ}{.}4, 58^\circ$) in vr = (−18, −12) km s^{-1}.	1
GS057.7+02.6−14	A compact source in the southwestern wall ($\ell \sim 56\overset{\circ}{.}4$, $b \sim +1\overset{\circ}{.}8$) in vr = (−15, −11) km s^{-1}.	1
GS060.2+01.1−74	Two CO emission features in the eastern wall, where can even be a part of GS63.6 + 01.0 − 71, in vr = (−76, −69) km s^{-1}.	1
GS061.3+02.6−69	No CO emission associated with shell walls.	1
GS061.6−00.5+54	Several clumps in many parts of a wall (including some portion of the eastern wall which seems to belong to GS064.0−01.1+45 either) in vr = (+36, +50) km s^{-1}.	1
GS063.3−00.4−3	Filamentary features along the northern wall which shows a dramatic morphological change in velocities from −18 to −5 km s^{-1} and a clump in the eastern wall ($\ell \sim 64\overset{\circ}{.}9$, $b \sim +0\overset{\circ}{.}3$) in higher velocities (between −5 and 2 km s^{-1}).	1
GS063.6+01.0−71	CO emission features in some shell walls: one in the eastern wall, which borders with GS064.3 − 00.9 − 80, in vr = (−75, −70) km s^{-1} and two in the western wall in vr = (−78, −71) km s^{-1} (some of which can even be a part of GS60.2+ 01.1 − 74).	1
GS064.0−01.1+45	Some clumps in the western wall which is likely to be also part of GS061.6−00.4+54 in vr = (+34, +44.5) km s^{-1}.	1
GS064.3−00.9−80	A CO emission feature appears in its northern wall, where is overlapped with GS063.6+01.0−71. It may not be related to this shell since the CO emission line shows a peak at lower negative velocities than where this shell is seen, but the possibility may not be entirely ruled out.	1
GS066.8−02.1−39	No CO emission associated with shell walls.	1
GS067.5+00.1−93	...	...
GS072.3+01.3−46	CO emission is seen at some same velocities, but it seems to be not associated.	1
GS072.3+03.1−56	CO emission is seen at some same velocities, but it seems to be not associated.	1
GS074.8−00.9+29	Some clumps in the western wall (especially, one at the tip of H I filamentary gas ($\ell \sim 72\overset{\circ}{.}4$, $b \sim 1\overset{\circ}{.}9$) in vr = (+23, +30) km s^{-1}).	1

Note. The last column gives reference(s) of CO information as follow: (1) Dame et al. (2001, CfA ^{12}CO $J = 1-0$ Survey; $8\farcm7$), (2) Jackson et al. (2006, GRS ^{13}CO $J = 1-0$ Survey; $46''$), (3) Planck Collaboration et al. (2014, Planck ^{12}CO $J = 1-0$ integral map (TYPE 2); $15'$), (4) Kawamura et al. (2001, See their Figures 5, 7, and 8).

[a]Partially covered. No data at $b > 1\fdg15$.
[b]Partially covered. No data at $b < -4^\circ$ and part of the northeastern wall.
[c]Partially covered. No data at $l < 45^\circ$.
[d]Partially covered. No data at $b \lesssim -3^\circ$ except for a western part of this shell.
[e]Partially covered. No data at $v_{\rm LSR} < -5$ km s^{-1}.

Appendix D

List of Abbreviations

The following table describes the meaning of various abbreviations and acronyms used in the thesis. The page number given in the last column is where each one is defined or first used. Nonstandard acronyms that are used in some places to abbreviate the phrases which frequently appear are not in this list.

Table D.1

List of Abbreviations

Abbreviation	Meaning	Page
ALFA	Arecibo L-band Feed Array	7
CCSNe	core-collapse supernovae	3
CGPS	Canadian Galactic Plane Survey	6
CHVC	compact high-velocity cloud	74
FWHM	full width at half-maximum	1
GCN	Galactic center negative	118
HVC	high-velocity cloud	2
I-GALFA	Inner-Galaxy Arecibo L-band Feed Array	7
ISM	interstellar medium	1
LAB	Leiden/Argentine/Bonn	6
RMS	root-mean-square	16
Sct-Cen	Scutum-Centaurus	81
SGPS	Southern Galactic Plane Survey	5

Continued on Next Page...

Table D.1 – Continued

Abbreviation	Meaning	Page
SN	supernova	2
SNe	supernovae	2
SNR	supernova remnant	5
VGPS	VLA Galactic Plane Survey	9
WISE	Wide-field Infrared Survey Explorer	78

요 약

성간공간 내 중성수소가스는 대개 필라멘트, 고리, 구각구조의 형태를 이룬다. 중성수소가스 구각구조는 항성풍, 초신성 폭발과 같은 에너지원으로부터 발생한 초음속 충격파에 휩쓸린 성간물질이다. 중성수소가스 구각구조 중 "거대 구각구조"라 불리는 매우 큰 구조는 형성에 필요한 에너지가 3×10^{52} erg 이상에 이른다. 이들의 형성기원은 OB성협 내 다수의 초신성 폭발이나 고속구름과 우리은하 원반의 충돌로 여겨지고 있다.

본 학위 논문에서는 "Inner-Galaxy Arecibo L-band Feed Array (I-GALFA)" 중성수소 21-cm 탐사 자료를 이용하여 우리은하 1사분면의 ($\ell \approx 32°$–$77°$, $|b| \approx 10°$) 중성수소가스 구각구조에 대한 체계적인 연구를 수행하였다. 이 탐사 자료의 고분해능 ($4'$)과 고감도 (0.2 K)는 이전의 저분해능 연구에서 찾은 대상들의 본질을 더 잘 이해하는데 도움이 된다. 또한, 탐사 자료로부터 이전에 발견하지 못 했던 세기가 약하거나 먼 거리에 있는 중성수소가스 구각구조를 발견할 수 있다. 이 논문에서 수행한 일은 크게 세가지로 나뉜다. 첫번째는 알려진 초신성잔해와 관련된 빠르게 팽창하는 중성수소가스 구각구조에 대한 연구이고, 두번째는 Heiles (1979)의 저분해능 ($36'$) 자료를 이용해서 찾은 중성수소가스 구각구조를 재확인하고 새로운 구각구조를 탐색하는 것이다. 세번째는 거대 구각구조 GS040.2+00.6−70 (GS040)와 조밀 고속구름 HVC 040+01−282 (CHVC040)의 공간 및 속도 구조에 대한 상세한 연구이다.

첫번째 연구에서 I-GALFA 탐사 역역 내 39개의 초신성잔해 중 4개의 초신성잔해가 연관된 중성수소가스 구각구조를 가짐을 확인하였다. 그 4개의 초신성잔해는 W44, G54.4−0.3, W51C, CTB 80 이다. 4개 모두 이전 저분해능 자료 연구에서 이러한 정황이 알려져 있었고, G54.4−0.3를 제외한 나머지는 아레시보 망원경 자료를 이용한 연구도 수행되었었다. 하지만, 본 연구에서 알게된 새로운 사실은 초신성잔해 W44에서 초고속 중성수소 방출선이 음과 양의 속도대에서 모두 발견된 것이다. 각각의 방출선은 팽창하는 중성수소가스 구각구조의 다가오고 면과 멀어지는 면에 해당한다. 이 발견은 '우리은하 안쪽 (inner Galaxy)'에 위치한 초신성 잔해로부터 팽창하는 중성

수소가스 구각구조의 양면을 모두 관측한 첫번째 사례이다. 또한, 고분해능 I-GALFA 자료에서 초신성잔해 G54.4−0.3와 관련된 중성수소가스 구각구조가 매우 대칭이며 둥근 형태로 두드러져 보인다. 4개 초신성잔해의 물리량을 조사하였고, 탐사 영역 내 다른 초신성잔해들과의 차이를 토의하였다. 그리고, 이 4개의 초신성잔해가 핵심 붕괴 초신성의 잔해로써 상대적으로 밀한 주변 물질과 상화작용하고 있다고 결론지었다. 또한, 중성수소선에서 초신성잔해의 가시성을 논의하였다.

두번째 연구에서 I-GALFA 자료에서 총 38개의 중성수소가스 구각구조를 목록화하였다. 이 중 13개는 이전에 알려진 Heiles 구각구조이고 나머지 25개는 새로 발견된 것이다. 그들의 기하 평균 지름과 속도범위는 각각 1°–13°, 7–65 km s^{-1}에 이른다. 고분해능 I-GALFA 자료에서 몇몇의 중성수소가스 구각구조는 (대개 우리은하 안쪽에 있는 대상들) 여러 구각구조나 또다른 굴뚝구조와 복합되어 있음을 보여준다. 또한, 몇몇은 별탄생이 활발한 영역 근처에 위치하고 있을 것이라 짐작케 한다. 본 연구에서 찾은 구각구조의 거리와 실제 반경, 형성에 필요한 에너지, 그리고 은하원반중심으로부터의 높이를 추정하였다. 그들 중 15개는 거대 구각구조로 여겨진다. 또한, 은하 중심 거리에 따른 구각구조의 분포와 전리수소영역 혹은 분자운의 분포를 비교분석하였다. 비교 결과는 많은 우리은하 안쪽 거대 구각구조가 본 연구 목록에서 결여되었음을 시사한다. 이것은 많은 거대 구각구조가 은하원반을 뚫고 나가 그 형태가 깨어졌고 굴뚝구조나 지렁이구조로 진화하였기 때문이라고 볼 수 있다. 마지막으로, 중성수소가스 구각구조와 분자운의 연관성을 조사한 결과를 제시하였다.

세번째 연구에서 우리은하 외곽부에 위치한 킬로파섹 크기의 거대구각구조 GS040의 기하학적 중심부에 CHVC040이 위치함을 발견하였다. 아레시보 자료는 GS040이 거의 완전한 원형의 고리 형태를 하고 안쪽에는 복잡한 구조를 가짐을 보인다. CHVC040은 희박한 가스에 둘러싸인 밝고 길쭉한 중심부를 가지고 있고, 은한 원반과 먼 쪽의 경계가 뚜렷함을 보인다. 두 천체의 형태와 물리적 특성을 분석한 결과는 이 거대 구각구조가 대략 4.3만년전 CHVC040과 은한원반 가스와의 충돌로 만들어 졌음을 시사한다. 또한, CHVC040은 근처 분열된 은하의 파편이거나 은하간 부착흐름 (accreting flow)에서 기인한 구름으로 생각된다. 이 연구 결과는 밀한 고속구름 중 몇몇은 우리은하

팽대부를 지나 원반까지 도달할 수 있으며 우리은하 원반에 에너지와 운동량을 공급할 수 있음을 보여주는 관측 증거라 할 수 있다.

주요어: 우리은하: 은하원반 – 성간물질: 거품구조 – 성간물질: 초신성잔해 – 성간물질: 분자운 – 전파선: 성간물질

학 번: 2008-30826